Investigation of Ultrafast Electronic and Nuclear Dynamics in Molecular Nitrogen using an XUV Time Delay Compensating Monochromator

Im Fachbereich der Physik
der Freien Universität Berlin
eingereichte Dissertation

von

Martin Eckstein

Berlin 2015

This work was performed between October 2010 and July 2015 at the department for Attosecond Physics at the Max-Born-Institute of the Leibniz Society under the supervision of Prof. Marc Vrakking and Dr. Oleg Kornliov.

Berlin, in July 2015

1. Gutachter: Prof. Dr. M.J.J. Vrakking
2. Gutachter: Prof. Dr. G. Sansone

Tag der Disputation: 12.10.2015

Erklärung der Selbstständigkeit

Hiermit versichere ich, die vorliegende Arbeit selbstständig verfasst und keine anderen als die angegebenen Quellen und Hilfsmittel benutzt sowie die Zitate deutlich kenntlich gemacht zu haben. Die Arbeit ist weder in einem früheren Promotionsverfahren angenommen noch als ungenügend beurteilt worden.

Berlin, 29.7.2015   Martin Eckstein

Contents

Contents

1 Introduction

Time-resolved XUV spectroscopy allows investigation of dynamical processes directly in the time domain with both excellent time and spatial resolution due to the shorter wavelengths of the XUV light as compared to spectroscopy in the visible range. In recent years XUV pulses with attosecond pulse durations coming from laser-driven high-harmonic-generation (HHG) sources have been successfully applied to investigate, for the first time, purely (multi)-electron dynamics, which are taking place on few femtosecond or even sub-femto second timescales, in atoms [1], molecules [2] and solids [3].

One of the most natural fields for the application of time-resolved optical spectroscopy is photochemistry. In the photochemistry of molecules, light-induced dynamics in the electronic cloud lead to structural rearrangements of the molecule that determine the chemical reaction pathway. The novel XUV-based experimental techniques make it possible to study both the motion of electrons and ion cores completely in the time domain, in order to gain further insight into the complex relations between different degrees of freedom of the involved particles.

While the application of HHG-XUV sources for time-resolved studies has been a success in the recent decade, they still develop towards more elaborate experiments that can be tailored to study specific dynamical processes. At the same time extensive theoretical efforts are being carried out to model the dynamics. A close and direct exchange between theory and experiment is absolutely crucial for future developments in the research field.

In this thesis we concentrate on XUV-induced ultrafast dynamics in molecular nitrogen (N_2), which is a diatomic molecule with one of the strongest chemical bonds that exist. Despite its simple molecular structure it exhibits many dynamical effects that are common to all molecules. Its relatively simple molecular structure allows for sophisticated theoretical modelling and the interplay between theory and experiment helps to develop theoretical tools to describe the multi-electron dynamics and their possible consequences for the structural dynamics on ultrafast time-scales. The main XUV-induced process investigated in this thesis is the inner-valence ionization of N_2 that leads to ultrafast dissociation of the molecule. Inner-valence ionization of N_2 has been in the focus of spectroscopic research for decades [4–6], but the complex nature of the involved electronic states has prevented complete assignment of different dissociation channels. We provide the complementary time-domain investigation of the inner-valence ionization and are able to offer new insights into this long-standing puzzle.

While HHG sources provide excellent temporal characteristics, the XUV pulses coming from HHG are commonly spectrally much broader than the bandwidth required to support the pulse duration. This is especially detrimental for the powerful method of photoelectron

spectroscopy, since the spectral width of the XUV pulse directly translates itself into the energy resolution of the measurement.

Therefore a significant portion of this thesis is devoted to the development of a general method to overcome this problem. We spectrally filter the XUV radiation generated by the HHG-source with a special XUV-monochromator that is designed to preserve the temporal duration of the XUV pulse, essentially creating a source that delivers ultrashort bandwidth limited pulses with tunable center wavelength. Such a monochromator is called a time-delay compensating monochromator (TDCM) and was demonstrated to work in the group of Mauro Nisoli in 2009 [7]. We designed and implemented an HHG-beamline for time-resolved XUV/IR photoelectron and photoion spectroscopy, that is hosting such a TDCM. Special emphasis lies on the usability and reliability of the system to make it a versatile tool to study complex dynamics with excellent time and energy resolution and allowing long data acquisition times. The XUV center energy can be tuned in a range between 3 eV and 50 eV, with an energy resolution below 0.4 eV and the time-resolution is below 30 fs. It is designed to achieve time-resolutions below 5 fs in the future, when the HHG driving laser source will be improved. The energy range can easily be extended to higher energies without great efforts. The optical layout was designed in collaboration with the group of Luca Poletto at CNR-IFN in Padova which is specialized in construction of XUV spectrometers and monochromators.

We employ the newly built experimental setup, to perform time-resolved photoelecton and photoion spectroscopy (using a velocity imaging spectrometer, VMIS) of N_2, where our focus is on the photoionization-induced dissociation dynamics after the creation of an inner-valence hole by XUV energies above 37 eV. In this energetic region the ionized molecule is left in a highly excited state that leads to ultrafast dissociation of the molecule on a few femtosecond timescale. The highly correlated interactions between the electrons during the bond-breaking of the triple bond are a challenge for theoretical modelling. Experimental time-resolved studies can gain further insight into the underlying dynamics.

By varying the XUV center energy in the range of 32 eV to 48 eV around the threshold energy at 37 eV, we are able to clearly identify different dissociation channels, both resonant to the XUV energy and induced by direct ionization. The time-resolved study stimulated improved theoretical modelling of the involved electronic states. The calculations were carried out by Oleg Kornilov and Hans-Hermann Ritze, within our group. The newly modelled states are in better agreement with the observed experimental data, compared to the states available in the literature, and might have consequences for XUV-driven atmospheric chemistry and resulted in a publication [8].

Additionally, we exploit the full capabilities of the XUV monochromator and study the multi-electron dynamics of a Fano resonance at 17.5 eV, which is 2 eV above the ionization potential of N_2. The spectrally narrow XUV pulses can be tuned in energy to excite a specific resonance and at the same time are short enough to observe the lifetime of the resonance directly in the time domain by probing the dynamics with a short IR pulse. We study the dynamics by angular-resolved photoelectron spectroscopy and can clearly identify the different electronic states that are involved in the autoionization.

The thesis is organized as follows: In the second chapter an overview of the available theoretical modelling of the electronic structure of N_2 is given within the Born-Oppenheimer approximation. Additionally the result of new *ab initio* modelling performed by our group is presented. This chapter will provide the theoretical background for the time-resolved studies of N_2 presented in this thesis. The chapters 3 to 5 deal with the design, implementation and characterization of the TDCM. Chapter 3 describes the optical layout of the monochromator and estimates the theoretical performance limits of the system. The chapter ends with a technical description of the complete beamline. Chapter 4 presents a description of various alignment strategies that we developed during the installation of the beamline. In chapter 5 an overview of the practically achieved performance specifications and the corresponding measurement techniques is given. Chapters 6 and 7 present time-resolved photoelectron and photoion studies on the XUV-induced dissociation dynamics after ionization of an inner-valence orbital of N_2 with a binding energy of about 37 eV. The XUV central energy was set at six energies in a range of 32 eV to 48 eV corresponding to harmonics 21 to 31 of the HHG spectrum, in order to identify different possible dissociation channels, both resonant to the XUV energy and induced by direct ionization. Chapter 6 presents the static time-independent XUV spectra and their comparison with the literature. Chapter 7 presents the time-resolved experiments. In both chapters the agreement with the newly calculated electronic states is discussed. In chapter 8 time-resolved photoelectron spectroscopy on the multi-electron dynamics at a Fano resonance around 17.5 eV is presented. Chapter 9 gives a summary and outlook.

2 Electronic Structure of N_2

This chapter presents the electronic structure of N_2. A short introduction into *ab initio* modelling of the molecule, within the Born-Oppenheimer approximation, is given and the theoretical background of XUV photoionization is presented. This chapter is complemented with the presentation of new *ab initio* modelling results for inner valence states. The modelling is triggered by disagreements between our experimental results and results published in the literature. It is carried out within our group, by Oleg Kornilov and Hans-Hermann Ritze. These results prepare the basis for the interpretation of experimental results on time-resolved photoelectron and photoion spectroscopy in N_2, presented in the later chapters.

N_2 is one of the lightest diatomic molecules. It consists of 14 electrons and two N nuclei, each built from 7 protons and 7 neutrons. The abundance of the N^{14} isotope is larger than 99 %. The two ion cores are bound together by a triple bond, that has a binding energy of 9.79 eV [9], and is one of the strongest chemical bonds that exist in nature. Under normal laboratory conditions (1 bar, 25°) N_2 molecules is a gas.

After the ionization by an XUV photon with an energy above 28.5 eV, the molecule can directly dissociate on an ultrafast time scale below 100 fs [10]. The complex dynamics in the electronic cloud during the bond breaking and their relation with to the movement of the nuclei requires time-resolved spectroscopy to gain further insight.

For photon energies above 28.5 eV an increasing number of dissociation channels can be excited by photoionization. In this thesis we concentrate on a particular dissociation channel, that can be excited by an XUV photon energy above 36.5 eV. In this channel the dissociation is induced by the creation of an inner-valence hole at the moment of ionization. The XUV/IR beamline allows to vary the center XUV energy of the pulses around the threshold energy of the creation of the hole. The induced dynamics are probed by a second short IR pulse and time-resolved photoion and photoelectron spectra are recorded with a VMIS. By comparing the data obtained for different XUV pulse energies, we can identify the single hole dissociation pathway in the dataset and can gain insight into the dynamic evolution of the hole during the bond breaking. The different ionic states that are excited and partly lead to dissociation, are now described in more detail.

2.1 Electronic Structure

The complete wave-function describing N_2 depends on the position of the 14 electrons, the positions of the two nuclei and the spin of the electrons and nuclei. The center of mass for a diatomic molecule always is in the middle of the axis connecting the two nuclei and will be

the center of the coordinate system describing the spatial component of the wave-function.

An approximation to the complete wave-function can be made by separating the dynamics of the ionic cores from the electronic dynamics. This approximation drastically eases the computation of the wave-function and is called the Born-Oppenheimer approximation.

2.1.1 Born Oppenheimer Approximation

Electrons are much lighter than nuclei and therefore are expected to move much faster. This suggests a logical way of separating the spin-independent part of the Hamiltonian into a fast part describing electrons and a slow part responsible for the motion of the nuclei. This can be done in the following way:

$$\hat{H}_{mol} = \underbrace{\hat{T}_e + \hat{V}_{ee} + \hat{V}_{eN} + \hat{V}_{NN}}_{\hat{H}_{el}} + \hat{T}_N \tag{2.1}$$

where $\hat{T}$ stands for the kinetic energy operator, $\hat{V}$ is describing the static Coulomb interaction between the particles and the subscripts N stands for nuclei and e for the electrons. The Born Oppenheimer approximation neglects the influence of the dynamics of the nuclei on the electronic wave-function by neglecting the nuclear kinetic energy operator T_N when describing the electronic part of the wave-function. Due to the huge difference in mass between atoms and nuclei it is assumed that light electrons instantaneously (or adiabatically) adjust to the position of the nuclei. One can separate the solution of the complete wave-function into a part describing the electron wave-function and a part dealing with the positions and dynamics of the nuclei.

$$\Psi_{mol}(\vec{r}, \vec{R}) = \phi(\vec{r}, \vec{R})\psi(\vec{R}) \tag{2.2}$$

where $\vec{r}$ describes the spatial positions of the electrons, $\vec{R}$ the spatial positions of the nuclei, Ψ is the total wave-function, ϕ is the electronic wave-function and ψ the wave-function of the nuclei.

We neglect the influence of $\hat{T}_N$ on the electronic part, according to the Born-Oppenheimer approximation, and get

$$\hat{H}_{el}\phi(\vec{r}, \vec{R}) = W(\vec{R})\phi(\vec{r}, \vec{R}) \tag{2.3}$$

with $W(\vec{R})$ being the *potential energy curve* (PEC) for a 1D system yielding the potential for the nucleus motion. For the motion of the nuclear in the potential we solve

$$\left(\hat{T}_N + W(\vec{R})\phi\right)\psi(\vec{R}) = E_{tot}\psi(\vec{R}) \tag{2.4}$$

giving the complete energy E_{tot} including the kinetic energy of the nuclei. $W(\vec{R})$ usually can only be determined approximately by numerical methods, which shall be introduced in the following.

2.1.2 Ab initio Methods in Quantum Chemistry

Analytic solutions of equation 2.3 can not be found, even for the simplest molecules. Usually one has to apply numerical methods to find a wave-function which gives the lowest binding energy in equation 2.3. This function is considered to be the closest approximation to the true ground state wave-function [11]. The subtleties of the numerical methods can be very complex and are a complete research field on its own [12]. However a few aspects shall be presented here, in order to set the ground stage for the interpretation of the experiments in the thesis.

The first step in approximating the complete wave-function is usually the Hartree-Fock method (HF), see for example reference [11]. As the starting point for this numerical method one usually takes wave-functions for single electrons. These functions are typically constructed from functions describing atomic orbitals. They are parameterized and the parameters can be varied to change the shape of the wave-functions, which are commonly called molecular orbitals (MO). The method is a self-consistent method, where the multi electron wave-function is constructed from the MOs, by filling up the individual orbitals with electrons, according to the Pauli principle, taking into account the spin of the electrons, i.e. two electrons per orbital. The solution to equation 2.3 is then found by optimizing the individual orbitals in sequence. The interaction between the electrons is hereby taken into account by averaging the $\hat{V}_{ee}$ term (the mean-field approach). Since this approach takes as a starting point single electron functions the final solution cannot completely account for the interactions between the electrons ($\hat{V}_{ee}$).

To take into account these electron-electron correlations more correctly, a variety of approaches have been developed collectively that are called post-HF methods. They are essentially differently well-suited depending on the the size and structure of the molecule. One of the common methods is the configuration interaction (CI) method. In this method the MOs generated in the HF step are used to build electron configurations (or molecular states, MS) with one or more electrons excited from the ground state to higher-lying orbitals. The CI wave function is then built from these MS:

$$\phi(\vec{r}, \vec{R}) = \sum_l^M a_l \phi_{MS}^l(\vec{r}, \vec{R}) \tag{2.5}$$

where l indicates different MS with increasing excitation energy. The number M is essentially limited by the numerical power. This parameterization of the complete wave-function is then variationally optimized which yields the coefficients a_l. We define the *dominant configuration* of the CI state as the contribution with the largest coefficient a_l.

We can go even further and define the contribution of a MO to the multi electron state. In comparison to a MS, where a single MO can only be occupied by one or two electrons, the occupation of the single MO in the multi electron state can take any value between zero and two. We can express this in the following equation:

$$\phi = \sum_m^X |\phi_{MO}^m\rangle \langle\phi_{MO}^m|\phi\rangle = \sum_m^X b_m |\phi_{MO}^m\rangle \qquad (2.6)$$

The molecular orbital with the largest factor b_m is defining the *character* of the wavefunction. We now continue by describing different symmetries of all the involved orbitals and states.

2.1.3 Molecular Orbitals and Symmetries

The molecular orbitals are linear combinations of atomic orbitals centered at the position of the nuclei. At large internuclear distances the electrons are completely localized on the individual atoms and the atom is in one of the atomic (or ionic) states of N^+. The lowest-lying states in energy that will be relevant later in the thesis are given in the following table:

N		N^+	
Configuration	Energy [eV]	Configuration	Energy [eV]
$2s^2 2p^3 \ ^4S^o$	0	$2s^2 2p^2 \ ^3P$	0
$2s^2 2p^3 \ ^2D^o$	2.38	$2s^2 2p^2 \ ^1D$	1.90
$2s^2 2p^3 \ ^2P^o$	3.58	$2s^2 2p^2 \ ^1S$	4.05
$2s^2 2p^2(^3P)3s \ ^4P$	10.33	$2s2p^3 \ ^5S^o$	5.80
$2s2p^4 \ ^4P$	10.92	$2s2p^3 \ ^3D^o$	11.44
$2s^2 2p^2(^1D)3p \ ^2D^o$	13.70		
$2s^2 2p^2(^1S)3s \ ^2S$	14.42		
Lim N^+	14.53	Lim N^{++}	29.60

Table 2.1: Atomic energy states of N and N^+ and the corresponding ionization thresholds. For the energetic region above 10.92 eV in the case of N only states with a principle quantum number not larger than 3 are presented.

The first part of the configuration column denotes the occupation of orbitals. The two electrons in the $1s$ shell are omitted. The second part gives the coupling of the total angular momentum and the spin as is encoded in the following term symbol:

$$\text{Term symbol for atoms:} \quad ^{2S+1}\Lambda \qquad (2.7)$$

with Λ taking the values 0, 1, 2, ... also labeled $S, P, D, ...$. Due to the electron interactions states with higher angular momentum can have lower binding energy, see also Hund's rules [13]. S can take the values 1/2, 3/2, ... for 7 electrons and 0, 1 ,2, ... for 6 electrons.

When the internuclear distance becomes smaller, the molecular orbitals are formed as a linear combination of the atomic orbitals. The center of the coordinate system is chosen

to be exactly in the middle between the atoms on the internuclear axis. In comparison to atoms the wave functions are not rotationally symmetric around the center point. However they are cylindrical symmetric around the internuclear axis, in a diatomic molecule. The projection of the total angular momentum onto the axis is therefore a conserved quantity and the main quantum number to characterize the solutions, again with a term symbol.

$$\text{Term symbol for MO :} \quad n\lambda_{g/u} \tag{2.8}$$

λ is the angular momentum projected on the molecular axis, and again can take the values 0, 1, 2, ... also written as $\sigma, \pi, \delta, ...$ (Now with small greek letters). n is the main quantum number. The solutions can be grouped further by symmetries, beyond the one that is associated with projection of the angular momentum. g/u correspond to inversion symmetry through the origin of the coordinate system. If there is an inversion center, as it is the case for a diatomic molecule, this can only result in

$$gerade : \quad \Psi(\vec{r}) = \Psi(-\vec{r}) \tag{2.9}$$
$$ungerade : \quad \Psi(\vec{r}) = -\Psi(-\vec{r}) \tag{2.10}$$
$$\tag{2.11}$$

denoted as g/u. From equation 2.5 and 2.6 we see that the multi-electron wave-function can be described as a combination of the molecular orbitals. The symmetry of the multi-electron wave-function is deduced from the symmetries of the MO.

$$\text{Term symbol for the multi-electron wave-function :} \quad {}^{2S+1}\Lambda_{g/u}^{+/-} \tag{2.12}$$

Again Λ is the projection of the total orbital angular momentum onto the internuclear axis. It takes the values 0, 1, 2, ... that are again labeled $\Sigma, \Pi, \Delta, ...$, only now with capital letters. S is the total spin of the electrons, which is the sum of the single spins of all the electrons and can take the values 0, 1/2 or 1 and has the degeneracy of 2S+1 (singlet, doublet or triplet). Due to the Pauli principle the total wave function has to be antisymmetric. If the spin function is symmetric, for example if S=1 (triplet), the wave function has to be antisymmetric under the commutation of electrons. In the other case of a S=0, (singlet) the spin function is antisymmetric and the wave function has to be symmetric.

These solutions are characterized by an additional symmetry. +/- is referring to a reflection inversion at an arbitrary plane with the internuclear axis lying in the plane. For Σ states plus and minus are degenerate in energy.

We introduced the building blocks of the multi-electron wave-function and explained their grouping and ordering by different symmetries. We we will now present, as an important example, the ground state of N_2.
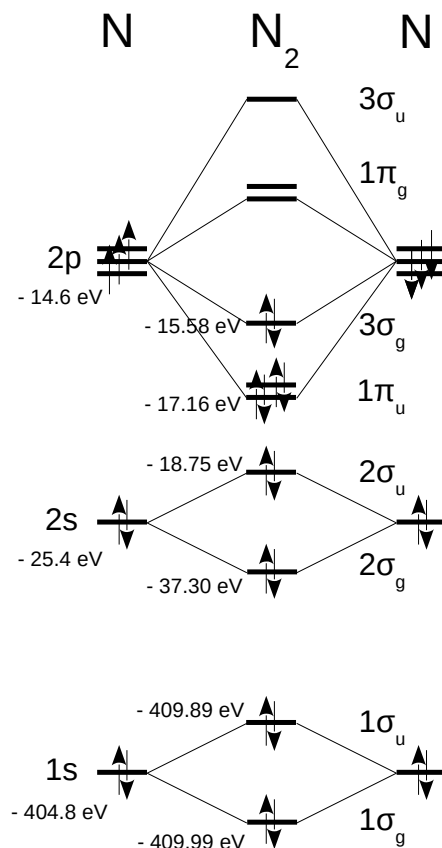
Figure 2.1: Occupation of molecular orbitals of the $^1\Sigma_g^+$ ground state of N_2 and their atomic orbital origin. The energies of the molecular HF-orbitals and also the atomic orbitals are taken from [14].

Ground State of N_2

In figure 2.1 the composition and the shape of the different orbitals of the ground state of N_2 is shown. The presented state is the output of the Hartree-Fock-Method and is the dominant configuration in the actual ground state wave-function with the symmetry

$$\Phi_X^{MS} = {}^1\Sigma_g^+ \tag{2.13}$$

and the occupation of orbitals

$$1\sigma_g^2 1\sigma_u^2 2\sigma_g^2 2\sigma_u^2 1\pi_u^4 3\sigma_g^2 \tag{2.14}$$

The π orbital can be occupied by four electrons due to its double degeneracy with angular momentum projection on the internuclear axis of one. The energetic ordering of

the molecular orbitals depends strongly on the internuclear distance. The occupation of orbitals with electrons is given for the equilibrium internuclear distance of

$$R_{Eq.} = 1.12 \text{ Å} \tag{2.15}$$

Before introducing the potential energy curves we will present a few theoretical aspects of photoionization and, more specifically, how the potential energy curves belonging to N_2 and N_2^+ are connected.

2.2 Photoionization Including Electron Correlations

In the case of photoionization, a molecule (or atom) can be ionized by the absorption of a single XUV photon. After the removal of one or more electrons, the molecule can be in different final ionic states, with different energy ionization thresholds. The probability of exciting specific ionic states with ionization potential smaller than the XUV photon energy is given by the partial photoionzation cross-section:

$$\sigma_\alpha(\epsilon) \propto \left| \left\langle \Psi_{\alpha,\epsilon-\epsilon_0}^N(\vec{r}) \left| \mu \right| \Psi_0^N(\vec{r}) \right\rangle \right|^2 \tag{2.16}$$

Where $\Psi_{\alpha,\epsilon-\epsilon_0}^N$ is the final state and Ψ_0^N is the initial ground state. N is the number of electrons and α denotes the final ionization channel. μ is the multi-electron dipole operator, which is simply the sum of the individual operators acting on a single electron and $\epsilon - \epsilon_0$ is the energy of the electron above the ionization threshold.

The final state consists of the parent ion and the electron that was removed from the ion and placed into the continuum. The final state can be separated into two parts and the total final wave-function then reads.

$$\Psi_{\alpha,\epsilon-\epsilon_0}^{(N)} = \Psi_\alpha^{(N-1)} \otimes \chi_\epsilon \tag{2.17}$$

where $\Psi_\alpha^{(N-1)}$ is the ionic state and χ_ϵ a wave-function describing the electron in the continuum. For large radii this scattering wave-function is converging to the wave-function of a free particle moving with kinetic energy $\epsilon - \epsilon_0$. However close to the nucleus the wave-function has to mimic the electron still moving in the potential of the ionic core $\Psi_\alpha^{(N-1)}$. Here lies the biggest challenge for correctly modelling the energy-dependent cross section.

In order to reduce the complexity we can make the following assumptions that are also applied in [14], where results for the N_2 XUV energy dependent cross-section are presented. First the ground state is approximated by its dominant configuration, i.e. the dominant molecular state that was described in the previous section 2.1.3.

$$\Psi_0^N = \Phi_X^{MS} \tag{2.18}$$

This facilitates the modelling of the wave-function for the electron in the continuum. The final ionic state however can be described again by more elaborate methods, such as the CI method. This is of great importance, since it is highly likely, that in addition to the removal of the single electron also the other electrons absorb energy and are lifted into higher excited states. Usually for these higher excited states the electron-electron interactions cannot be neglected. The final ionic state is then described by a mixture of molecular states.

$$\Psi_\alpha^{N-1} = \sum_l^M a_l \phi_{MS}^l(\vec{\mathbf{r}}, \vec{\mathbf{R}}) \tag{2.19}$$

where l indicates the different configurations, that are again defined by the occupation of molecular orbitals. As we are only dealing with ionization from the ground state, the occupation of the orbitals is usually given only with respect to Φ_X^{MS}, i.e a removal of an electron from an molecular orbital in the ground state, or an excitation of an electron in a different orbital.

2.3 Potential Energy Curves of N_2

In this section the potential energy curves of N_2^+ manifold are presented. In the presented experiments we mostly observe single photon XUV ionization of N_2 and the correct description of the final ionic states is the key element in this case. In figure 2.2 the potential energy curves for the N_2^+ ion are plotted. As a reference also the ground state of the N_2^{++} is shown. On the left a collection of potential energy curves from various sources is presented, [15] and [13]. On the right, calculations performed in our group by Oleg Kornilov and Hans-Herman Ritze are presented. These will be discussed in a separate section.

The PE-curves are categorized by their symmetries omitting any curves with angular momentum larger than 1. The important states with the biggest XUV single photon ionization cross-sections are also labeled by capital letters A,B,C... and so on, for convenience.

In the table 2.2 parameters of most important states taken from [13] and [15] are summarized. The binding energy of the states is given for equilibrium internuclear distance. The labelling of the dominant configuration gives the difference in orbital occupation with respect to the ground state. The states X,A and B are electronic states corresponding to the removal of the two outermost occupied valence orbitals. They have a single hole character and are expected to have a large XUV ionization cross-section. From there on upwards in energy a few states with two holes and a single electron lifted to the first unoccupied orbital π_g can be found. The next single hole state would correspond to a Σ_g manifold and the removal of an electron from the $2\sigma_g$ orbital. This state is expected in the energetic region above the F-state with 28.5 eV. However in this energetic region also other highly excited states are expected and the states differ strongly from the Hartree-Fock states. In the figure 2.2a the set of Σ_g states is marked in grey. They are taken from [15]. The state with the biggest XUV cross-section is the state 6 and marked in blue.
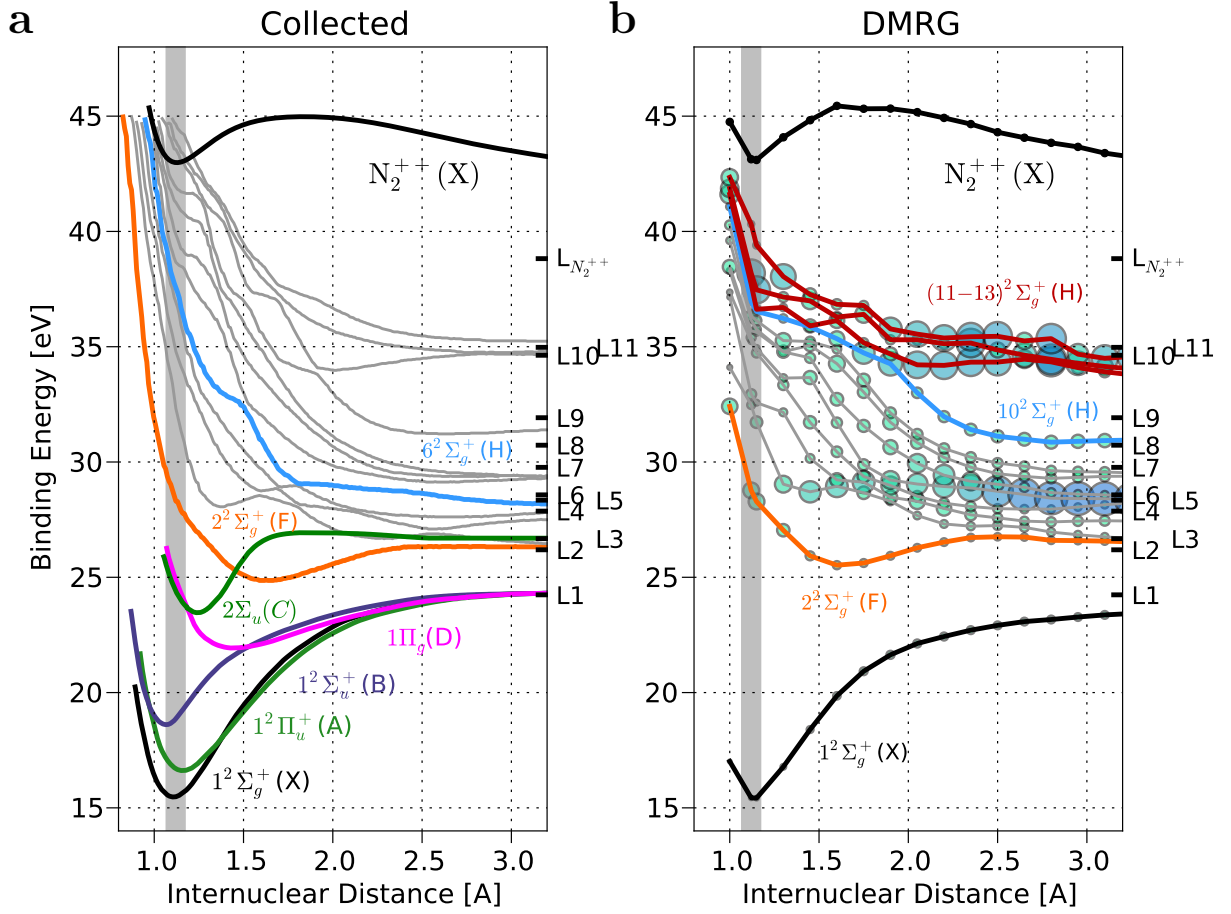
Figure 2.2: a: Potential energy surfaces belonging to the N_2^+ manifold. The ground state of N_2^{++} manifold is given as a reference. The curves are taken from the source [13]. For the energy range above 30 eV only states with Σ_g symmetry are presented. These are from the publication [15]. The exact energies of the dissociation limits are given in table 2.3. **b:** Output of DRMG *ab initio* calculation for states of the N_2^+ manifold with Σ_g symmetry. The size and of the marker indicates the density of the $2\sigma_g^{-1}$ hole density in the complete state.

Manifold	State	Term	EE [eV]	Dominant Configuration	Limit
N_2	X	$1^1\Sigma_g$	0	$1\sigma_g^2 1\sigma_u^2 2\sigma_g^2 2\sigma_u^2 1\pi_u^4 3\sigma_g^2$	9.9 eV
N_2^+	X	$1^2\Sigma_g$	15.5	$3\sigma_g^{-1}$	L1
N_2^+	A	$1^2\Pi_u$	16.9	$1\pi_u^{-1}$	L1
N_2^+	B	$1^2\Sigma_u$	18.9	$2\sigma_u^{-1}$	L1
N_2^+	C	$2^2\Sigma_u$	24.4	$1\pi_u^{-1} 3\sigma_g^{-1} 1\pi_g^{+1}$	L3
N_2^+	D	$2^2\Pi_g$	24.9	?	L1
N_2^+	F	$2^2\Sigma_g$	28.5	$2\sigma_u^{-1} 1\pi_u^{-1} 1\pi_g^{+1}$	L3
N_2^+	E	$3^2\Sigma_g$	32.3	?	L3
N_2^+	H	$6^2\Sigma_g$	37.5	$2\sigma_g$	L6
N_2^{++}	X	$1^1\Sigma_g$	42.9	$1\sigma_g^2 1\sigma_u^2 2\sigma_g^2 2\sigma_u^2 1\pi_u^4$	38.8 eV

Table 2.2: Selection of states of the N_2^+ manifold that have the largest XUV-single photon cross-section for photon energies up to 50 eV, taken from [15] and [13]. EE is the excitation energy of the state at equilibrium internuclear distance. The labelling of the dominant configuration gives the difference in orbital occupation with respect to the ground state. The limit column denotes the dissociation limit that the curve is adiabatically connected to. The highly excited Σ_g states are from [15]. The energy of the limits is given in table 2.3.

At large internuclear distances the electronic states are just the sum of two individual atomic states. The total energy of these limits can directly be calculated from the atomic states given in table 2.1. The total energy for the N_2^+ manifold is then

$$E_{Lim} = E_{N*} + E_{N^{+*}} + E_{N_2} \tag{2.20}$$

which is the sum of a neutral atomic state, a singly ionized atomic state, and the binding energy of the neutral ground state. The binding energy of the neutral ground state is 9.79 eV and the limits are listed in the table 2.3.

2.3.1 New ab initio Results for Inner Valence States

An improved calculation of the Σ_g^+ states above 30 eV is presented in figure 2.2b. It was carried out in our group by Oleg Kornilov and Hans Hermann Ritze and applies the density matrix renormalization group (DRMG) method [16–18] that is especially powerful for linear systems. Starting point is the HF calculation using cc-pVQZ basis set functions [19]. This basis set functions includes functions for highly excited Rydberg like atomic orbitals. The combination of the numerical method and the larger basis set leads to an improved convergence of states in the highly excited region above 30 eV at the equilibrium internuclear distance. A more detailed discussion of the calculation can be found in [8].

The binding energy in the middle of the FC region, the curve's limit and the $2\sigma_g^{-1}$ hole density character is summed up in the following table:

Limit label	Configuration $N^+ + N^*$	Energy (eV)
L1	$^3P +\,^4 S^o$	24.293
L2	$^1D +\,^4 S^o$	26.192
L3	$^3P +\,^2 D^o$	26.676
L4	$^3P +\,^2 P^o$	27.869
L5	$^1S +\,^4 S^o$	28.345
L6	$^1D +\,^2 D^o$	28.575
L7	$^1D +\,^2 P^o$	29.768
L7'	$(2s2p^3)^5S^o +\,^4 S^o$	30.094
L8	$^1S +\,^2 D^o$	30.728
L9	$^1S +\,^2 P^o$	31.921
L9'	$(2s2p^3)^5S^o +\,^2 D^o$	32.478
L9"	$(2s2p^3)^5S^o +\,^2 P^o$	33.670
L10	$^3P + (3s)^4S$	34.629
L11	$^3P + (3s)^2P$	34.973
	$^3P + (2s2p^4)^4P$	35.217
	$(2s2p^3)^3D +\,^4 S^o$	35.729

Table 2.3: Dissociation limits of the N_2^+ manifold.

Kornilov/Ritze													
Σ_g	1	2	3	4	5	6	7	8	9	10	11	12	13
Energy [eV]	15.4	28.8	32.5	32.9	35.2	35.4	35.7	36.2	36.3	37.0	37.7	38.2	40.3
Limit	L1	L3	L3	L4	L5	L6	L6	L7	L7	L9	L10	L10	L11
$2\sigma_g^{-1}$	0.01	0.13	0.04	0.06	0.02	0.05	0.02	0.02	0.07	0.02	0.10	0.42	0.02

Table 2.4: Result of new *ab initio* calculation for equilibrium internuclear distance. Limit denotes the dissociation limit of the state and $2\sigma_g^{-1}$ the hole density of the $2\sigma_g$ orbital.

The presented information in this chapter for different potential energy surfaces, the dissociation limits and the atomic electronic configurations will be used throughout the thesis when dealing with N_2. Especially the interpretation of the experimental results from XUV energy resolved photoelectron and photoion spectroscopy in chapter 6 and 7 relies on the numbers presented in the tables and the PE-curves. If needed, parts of the herein presented information, will be repeated.

3 Time Delay Compensating Monochromator

A major part of the content of this thesis is devoted to the design and implementation of an experimental beamline that combines a high harmonic generation (HHG) source with an XUV monochromator. The beamline is built to perform time-resolved XUV-IR pump-probe spectroscopy with tunable center energy of the XUV pulse. Exchangeable endstations can be connected to the beamline. In the course of this thesis a velocity map imaging spectrometer is used to perform angular resolved photoelectron and photoion spectroscopy on gaseous targets.

In this chapter the theoretical background of the optical layout of the monochromator and the technical implementation of the beamline are presented. In chapter 4 important alignment procedures that have to be carried out during the built-up and the daily operation of the beamline are presented and in chapter 5 experiments that demonstrate the performance of the beamline are analyzed and interpreted.

In the present implementation the HHG source generates XUV radiation with a typical HHG comb spectrum ranging from 10 eV to 60 eV. A typical spectrum is presented in figure 3.1a. The energy positions of the comb maxima are odd harmonics of the IR driver pulse spectral energy, which is equal to 1.57 eV. In the time domain this corresponds to an attosecond pulse train (APT), shown in figure 3.1b (blue), that consists of a train of attosecond pulses with a time spacing of about 1.3 fs and a duration of the envelope of the train of about 17 fs. In many cases only the duration of the envelope of the APT determines the time-resolution of a pump-probe experiment and in the case of photoelectron spectroscopy the spectral width of the XUV pulse directly translates into the energy resolution of the experiment. The pulse duration and minimal bandwidth to support a pulse are linked by the time-bandwidth product. For a Gaussian time profile this relation reads:

$$\Delta\tau = \frac{0.44h}{\Delta E} \tag{3.1}$$

where h is Planck's constant and ΔE is the spectral bandwidth of the pulse. For a pulse with 17 fs duration this results in a minimal bandwidth of only 0.10 eV. It is therefore theoretically possible to strongly reduce the bandwidth of the XUV pulse coming from the XUV source without stretching the envelope of the pulse in time, see figure 3.1. Such a spectrally narrow pulse improves the energy resolution of the experiment, while at the same time leaving the time-resolution unchanged.

The key element of the newly constructed beamline is a XUV monochromator, that can spectrally filter an incoming XUV pulse without changing its pulse duration, as long as

the time-bandwidth limit is not reached. The special design of this monochromator uses gratings and is called a time-delay compensating monochromator (TDCM). The optical design of the implemented version was determined in collaboration with the group of Luca Poletto at CNR-IFN in Padova, Italy, which is specialized in the optical design of XUV spectrometers and monochromators [7, 20–22].

Our collaborator supplied us with the optical layout of the monochromator and the specifications of the gratings. The technical implementation and the alignment of the monochromator was carried out by ourselves. Special attention was paid to create a flexible and stable beamline that is a reliable tool to perform IR/XUV pump-probe experiments where the center XUV energy can quickly be varied.

In the current implementation the monochromator has a transmission efficiency above 6 % , an energy resolution below 0.4 eV and the output pulse duration is below 10 fs. It can transmit XUV energies between 10 eV and 50 eV and stable measurement runs over several days can be performed.

This chapter is split into two sections. In the first section the theoretical background of the optical design of the monochromator is presented and the energy and time resolution are estimated by a simple ray-tracing model. In the second section the technical implementation of the complete beamline is described.

3.1 Spectral Filtering an HHG Source

The HHG process is used in our experimental setup to generate an ultra short XUV pulses, in the present case with a maximal energy up to 60 eV. The generation of the XUV light is a result of the highly non-linear response of a rare gas in a gas cell to the strong electric field of the IR pulse in the focus of the laser. The shape of the emitted XUV pulse in time and energy hereby depends on the response of the individual atoms to the electric field of the IR pulse and collective effects in the synchronized emission of the XUV light of all the atoms in the gas when the IR pulse travels trough the gas cell.

High Harmonic Generation

The single atom response of the atom can be described within the framework of the semi-classical three step model [23, 24]. It separates the modeling of the HHG process into three distinct steps. First a single atom is field ionized by the strong electric field of the IR pulse and an electron is placed into the continuum. Second the electron is accelerated by the oscillating IR field and moves on a trajectory through the vacuum. Due to the oscillatory change of the electric field, some trajectories lead to a recombination of the electron with its parent ion. In this case the accumulated kinetic energy of the electron is released as high energetic photons.

From this model the maximal energy that the emitted XUV light can have can be derived and is given by

$$E_c = I_P + 3.17 U_p \tag{3.2}$$

where U_p is the ponderomotive potential of the free electron in the oscillating electric field given by

$$U_P = \frac{e^2 E^2}{4 m_e \omega^2} \tag{3.3}$$

and I_p is the ionization potential of the atom, E is electric field strength and ω is the frequency of the driver pulse.

To this cut-off energy corresponds a unique trajectory of the electron which starts 18° after the maximum of the IR field. Electrons that are ionized before or after this optimal phase result in the emission of light with lower energy than the cut-off. In fact there are always two trajectories resulting in the same final XUV energy. It can be shown that for the short trajectories the time the electron spends in the vacuum is approximately linearly antiproportional to both the intensity of the IR field and the emitted XUV energy [23]. This will become important later in the discussion.

The temporal and spectral shape of the generated XUV pulse in the HHG depends on the phase matching between the generating IR pulse and the generated XUV pulse. The phase matching hereby depends on the shape of the IR pulse (both spatial and temporal) and the conditions of the gas in the cell. A detailed presentation of the dependency of the XUV pulse shape on all these parameters is beyond the scope of this thesis[1]. We will however discuss certain characteristics of the XUV pulse that are relevant for the thesis.

The temporal and spectral profile of the XUV pulse generated in the HHG cell are connected by Fourier transformations. We therefore can draw conclusions about the temporal shape of the XUV pulse from the spectrum of the XUV pulse: In figure 3.1a the spectrum of the XUV pulse coming from our HHG source is presented. To generate this spectrum an IR pulse with 35 fs duration and 600 μJ pulse energy is used. The focus spot size is on the order of 50 μm to 70 μm and the IR beam is focused with a spherical mirror with a focal length of 62.5 cm. The generation gas is Argon. In the time domain, presented in figure 3.1b, the pulse has a shape of a so called attosecond pulse train (APT) (blue), which consists of individual attosecond short XUV bursts from every half-cycle of the IR driver pulse. This temporal train leads to the XUV energy comb in the spectrum. Generally due to the nature of the Fourier transform of slowly varying functions there are two relations. The width of the envelope of the HHG spectrum defines the duration of the individual attosecond burst

$$\Delta E_{HHG} \propto \frac{1}{\Delta \tau_{A.B.}} \tag{3.4}$$

and vice versa the width of the individual harmonic defines the width of the envelope of the APT.

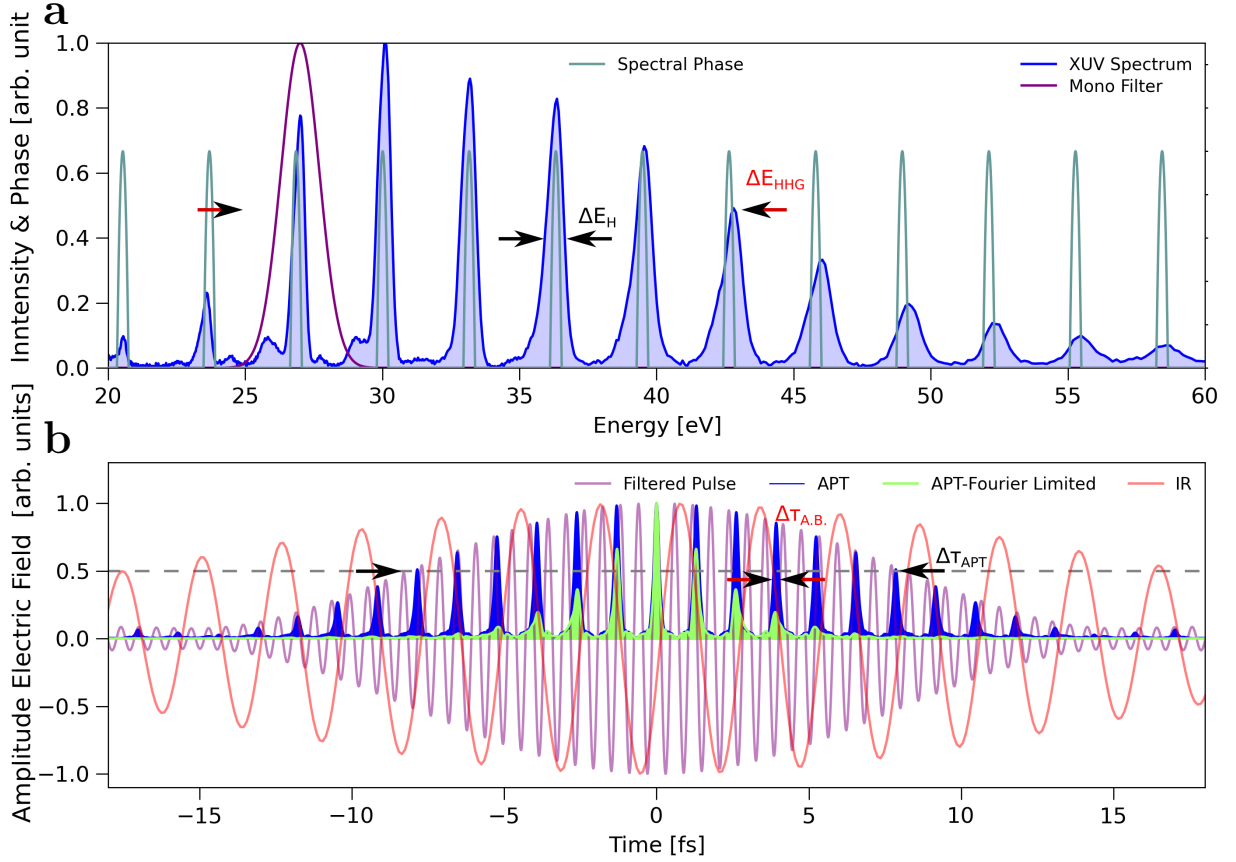[1]A detailed discussion can be found in [25, 26]

Figure 3.1: **a**: XUV spectrum recorded with a 35 fs pulse in Argon. The quadratic spectral phase of the individual harmonics, leads to non Fourier-transform limited pulses in the time domain. The XUV monochromator has an energy resolution that is sufficient to select a single harmonic. The spectral filter function is indicated in purple. **b:** The HHG spectrum leads to an APT in the time domain (blue). The linear chirp of the individual harmonics leads to an APT stretched in time, for comparison a Fourier limited APT is plotted in green. The influence of the spectral resolution of the XUV spectrometer on the recorded spectrum in **a** is neglected in both cases. However, the chirped APT in (blue) in **b** has usually about half the duration of the driving IR field and the amount of chirp in **a** is chosen accordingly by hand. A single filtered harmonic in the spectrum in **a** leads to a pulse with the same pulse duration as the envelope of the APT in **b**.

$$\Delta\tau_{APT} \propto \frac{1}{\Delta E_H} \tag{3.5}$$

In the figure 3.1b two APTs are depicted one in blue and one in green. They are both obtained by taking the Fourier transform of the spectrum presented in the top part of the figure. The green APT is the direct Fourier transform of the XUV spectrum assuming the

spectral phase is flat. It has a pulse duration of the envelope of about 6 fs. This is only an estimation of the shortest possible APT, since in neglects the influence of the spectral resolution on spectrometer on the recorded HHG spectrum. The blue APT is taking into account a quadratic spectral phase centered at the individual harmonics in the spectrum, whose origin will be explained in the following.

The quadratic spectral phase of the individual harmonics originates from the intensity dependency of the trajectories. For a pulse with a Gaussian profile in time the varying intensity results in a temporal varying phase for a given XUV energy, i.e. different trajectories lead to same XUV energy at different moments of time [27].

The top part of a Gaussian curve can be approximated by a quadratic curve, which results a quadratic phase dependency of an individual harmonic in time. The quadratic phase in time also translates into a quadratic phase in the spectral domain, where the individual quadratic dependence of a single harmonic is proportional to the quadratic phase dependency in time. This quadratic phase of the individual harmonics is indicated in figure 3.1a as green lines. As already mentioned the phase in the spectral domain leads to a stretch of the APT in the time domain and we chose the phase in such a way by hand that the envelope of the blue APT in figure 3.1 has half the duration as the IR pulse. (This overestimates the influence of the quadratic phase on the pulse duration of the APT, since we neglected the influence of the spectral resolution of the spectrometer on the recorded XUV spectrum.)

If the monochromator is set to spectrally filter a single harmonic, for example the 17th harmonic around 26 eV, this results in a pulse (purple) in time with a pulse duration equal to the duration of the envelope of the blue APT. The pulse inherits the quadratic phase dependence of the individual harmonic and therefore is linearly chirped. The chirp is negative, i.e the leading edge of the pulse is shifted to higher energies and the trailing edge is shifted to lower energies. The duration of the envelope of the chirped APT, and with that also the monochromatized pulse, is in between one half and one third of the IR pulse duration [28]. In the figure we plot the case where the XUV is of one half of the IR duration.

Since the chirp is linear it might be possible to compensate this chirp. In the case of the presented simulation this would correspond to a recompression of the XUV pulse from almost 17 fs to about 6 fs. It should be pointed out again that this is only assumption of the theoretically lowest limit. We neglect other influences in the measured spectral width of the HHG spectrum, such as the spectral resolution of the used spectrometer. A possible strategy for compensating the chirp is discussed in the outlook section.

3.2 Concept and Simulation of a TDCM

There are different approaches for the optical design of a monochromator in the XUV regime. Multilayer mirrors for the XUV have been available for quite some time and are a successful tool applied to spectrally filter XUV light coming from an HHG source [29, 30]. They are easy to implement, but do not allow a quick change between XUV energies so

far. They offer excellent time resolution but the energy resolution might easily reach a few eV with a non uniform energy dependent reflection profile. Correspondingly, it is difficult to get a high contrast between the desired harmonic and undesired adjacent harmonics.

Grating based monochromators usually offer more tuning flexibility in energy and excellent energy resolution but have to be designed carefully in order to provide good time-resolution too. The challenges in the time domain originate from the diffraction of the pulses from the grating. In the first diffraction order each rays coming from successive grating grooves have to travel an additional wavelength in order to constructively interfere. In the time domain this translates into a delay between the rays coming from the different grooves of the grating. The total time delay between the two edges of the optical mode illuminating the gratings then is

$$\Delta\tau_{Stretch} = \frac{\lambda}{c} \cdot N \tag{3.6}$$

where N is number of illuminated grooves, λ is the diffracted wavelength and c is the speed of light. For ultra short pulses on the order of only few tens of femtoseconds this stretch can be quite significant and completely spoil the time resolution. For example an XUV pulse with 30 nm center-wavelength has an optical cycle of 0.1 fs. With a grating with 300 grooves/mm and a spotsize on the grating of 5 mm, the stretch is already 150 fs.

There are two ways to deal with this problem. The first possibility is that the monochromator is designed very carefully to find the perfect trade-off between energy resolution and stretch by illuminating only a few grooves of a grating. As an example for an implemented version see [31]. However this puts strong constraints on the beam geometry for the HHG process, which might be obstructive for running the HHG source at optimal conditions. We follow a different approach and choose a design that compensates the delay with a second grating that is mounted in reverse diffraction order compared to the first grating and is placed in the beam after the first grating. This second stage recompresses the pulse in time by compensating the delay between the edges of the mode. This design is robust against the input geometry and opens the possibility to produce XUV pulses near the time-bandwidth product limit. The optical layout of this TDCM is discussed now.

3.2.1 Optical Layout of TDCM

The optical layout of a TDCM is presented in figure 3.2. The layout it separated into two stages. In the first stage the XUV light coming from, ideally, a point source is diffracted from a grating and then spectrally filtered by a slit. This stage is called the diffraction stage. The first stage consists of a toroidal mirror collimating the beam coming from the point source followed by a reflection grating dispersing the beam. The beam is then focused by a second toroidal mirror. The imaging of the beams by the second mirror into the focal plane is equivalent to a propagation into the far-field and leads to maximal geometrical separation of different wavelengths in space resulting in an optimal wavelength/energy resolution. The spherically curved toroidal mirrors and a possibly imperfect alignment
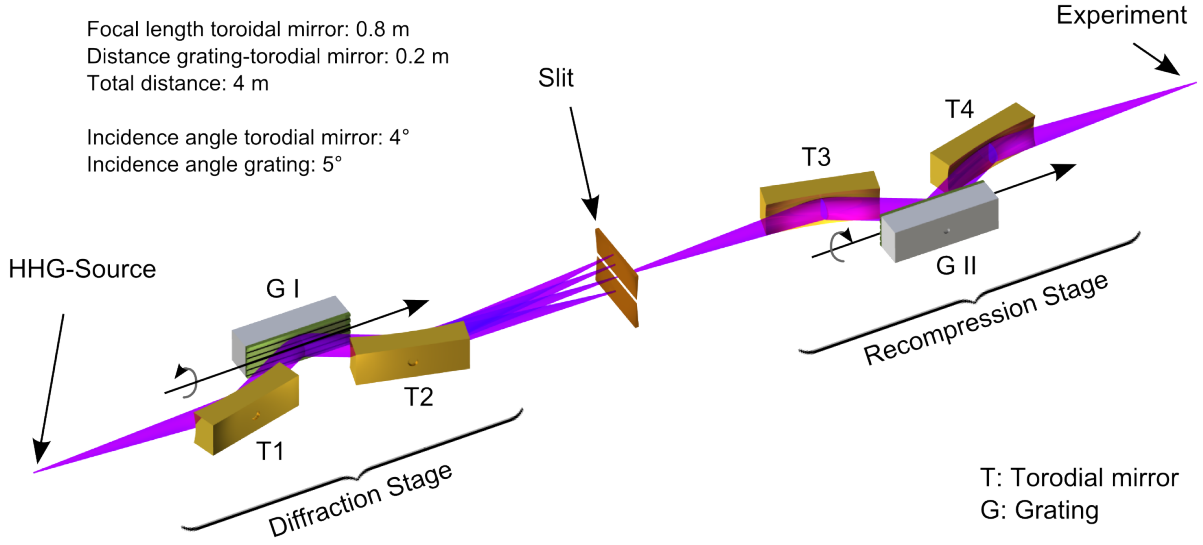
Focal length toroidal mirror: 0.8 m
Distance grating-torodial mirror: 0.2 m
Total distance: 4 m

Incidence angle torodial mirror: 4°
Incidence angle grating: 5°

Experiment

Slit

HHG-Source

T4

T3

G II

Recompression Stage

G I

T1

T2

Diffraction Stage

T: Torodial mirror
G: Grating

Figure 3.2: Optical layout of TDCM, consisting of four toroidal mirrors and two gratings operated in conical diffraction. The XUV beam coming from the HHG source is collimated by the first torodial mirror. The first grating diffracts the beam and separates the XUV energies. The different wavelengths are then focused in the slit plane, where the pulse is spectrally filtered. The gratings are operated in the so called conical diffraction mode, for details see figure 3.3. By rotating the gratings around their conical axis, the desired center wavelength is chosen. The slit position stays fixed. The second stage is symmetric with respect to the first stage, and compensates the time stretch induced by the first grating.

can induce aberrations in the imaging. It can be shown that for one-to-one imaging (no magnification or demagnification) higher order aberrations, such as coma and astigmatism, cancel out. The spherical aberrations remain. This is called Rowland configuration.

The second stage has an optical layout symmetric to the first stage. The grating in the second stage will compensate the pulse stretch that was induced by the diffraction from the grating in the first stage and is named recompression stage.

There is also the possibility to combine the individual stages into a single optical element, by replacing the grating by a spherical grating, that combines diffraction and focusing. A description of an implemented TDCM employing such gratings can be found here [32]. We chose to separate focussing and diffraction in order to ease alignment tasks and use only standard optical elements.

3.2.2 Transmission Efficiency and Conical Diffraction

One of the major design challenges of the monochromator for an HHG source is the over-all transmission efficiency.The toroidal mirrors are gold coated and are operated under 4°incidence angle and can achieve up to 80 % reflection efficiency over the complete spec-
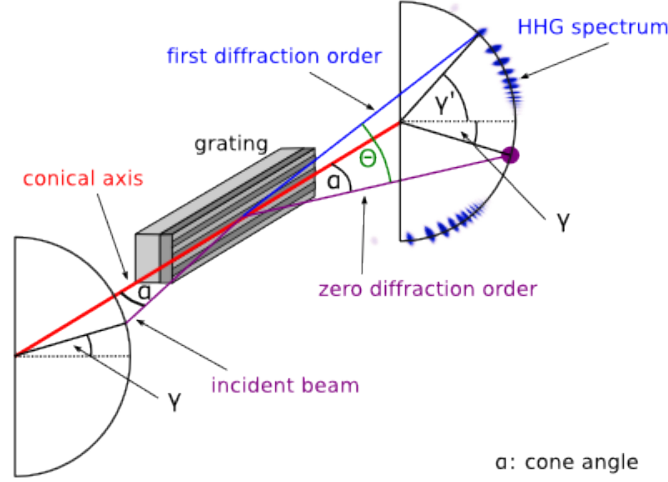
Figure 3.3: Conical diffraction geometry. The diffraction geometry is described in equation 3.7 The grooves of the grating are aligned in the same direction as the incoming beam. For $\gamma = 0$ the grooves are parallel to the projection of the incoming ray onto the surface of the grating. For incoming rays situated on a half cone (same incidence angle), the diffraction pattern is situated on a half cone with the same cone angle. The angle Θ marks the actual angle between two outgoing rays from the grating.

tral range of 10 eV to 50 eV. Concerning the gratings the situation is more complicated. Their reflection efficiency is the product of both coating reflection efficiency and diffraction efficiency. By mounting the gratings in so-called conical diffraction geometry, the diffraction efficiency can reach the coating reflection efficiency [33]. The diffraction geometry is illustrated in figure 3.3.

Compared to the standard mounting of a grating the grooves are (almost) aligned with the projection of the incoming beam on the grating surface. Due to momentum conservation the diffraction pattern is heavily bent. The diffraction pattern of an incoming ray with a cone angle α is lying on an outgoing cone with the same angle α . The modified grating equation reads

$$\sin \alpha (\sin \gamma + \sin \gamma') = m\lambda\sigma \tag{3.7}$$

where σ is the groove density, α the cone angle, m the diffraction order, γ is the angle of the incoming ray in a plane perpendicular to the conical axis, γ' the angle for the outgoing ray in a plane perpendicular to the conical axis (see figure 3.3) and λ the wavelength [33].

In the monochromator the gratings are rotated around their conical axis until the desired wavelength is passing the fixed slit after the first stage. Under rotation the cone angle stays constant and the outgoing diffraction patter is moves on the outgoing cone. For the ray

that is passing through the slit the following relation holds:

$$\gamma = \gamma' \tag{3.8}$$

In order to achieve maximal diffraction efficiency the grating grooves are blazed. For the wavelength passing through the slit the perfect blaze angle (δ) is simply equal to the rotation angle

$$\delta = \gamma \tag{3.9}$$

In this case the surface normals of the individual blazed grooves are lying in the plane of the incoming and outgoing beam and it has been demonstrated, that the diffraction efficiency can reach the coating reflection efficiency, which can be up to 80 % for gold [34][35]. The diffraction efficiency drops for grating rotation angles that differ from the perfect blaze angle. We need three gratings with different groove densities and blaze angles to cover the complete energy range between 10 eV and 50 eV with sufficient transmission efficiency and also energy resolution, which will be discussed in more detail in the next sections.

3.2.3 Optical Layout - Grating and Toroidal Mirror Parameters

The overall design of the optical layout of the monochromator is pretty straightforward. A small incidence angle of the XUV beam onto the optical elements is increases the reflection efficiency while at the same time the elements have to be longer (bigger) to reflect the complete mode. In the design constraints we fixed the mode diameter to a maximum of 6 mm and the incidence angles of the toroidal mirrors to 4°, in order to use standard optics (Hellma Optics). The incidence angle of the gratings (Richardson Gratings) was set to 5°, which is mainly due to energy resolution constraints that will be discussed in the next section. The focal length of the toroidal mirrors was set to 80 cm. It is beneficial that the arm length of the monochromator is relatively long for two reasons. After the HHG focus the residual IR has to be filtered out in order to not deposit its full thermal load onto the optical elements of the monochromator. This is usually done with the help of a thin aluminum foil, that is relatively transparent for the XUV light but reflects and absorbs the IR. Directly after the HHG focus the IR intensity is too high and burns the foil. It is therefore necessary to let the IR mode expand until it can be filtered out. On the other hand it is known that a loose focusing geometry helps to efficiently generate XUV from the IR due to the increased Rayleigh-range. A larger distance between HHG focus and first torodial mirror therefore opens more flexibility for choosing the IR focus geometry of the HHG. The relatively long arm length also is beneficial to fit an experimental endstation at the position of the final focus. We chose the maximum focal length of the toroidal mirror such that the experiment exploits the full length of the laboratory. The distance between the toroidal mirrors and the gratings can be chosen freely, since the beam is collimated. We chose a distance of 20 cm in order to potentially fit diagnostic tools in between toroidal mirror and grating. With these parameters the total length of the beamline sums up to 4 m. The individual parameters are summarized in the table 3.1.

Optical Element	Arm Length [cm]	Incidence Angle [°]	Length [cm]	Height [cm]
Toroidal	80	4°	9	1.5
Grating	20	5°	8	1.5

Table 3.1: Geometrical specifications of the optical elements implemented in the TDCM-monochromator.

Optical Element	Grooves/mm	Blaze Angle
Grating I	150	3.4°
Grating II	300	4.3°
Grating III	600	7°

Table 3.2: Grating specifications.

The selection of the grating specifications is more challenging. The goal is to cover the complete energy range between 10 eV and 50 eV with sufficient transmission efficiency and maintain relatively constant energy resolution, which is determined by the groove density. The transmission efficiency peaks around the center-wavelength with a rotation angle that is equal to the blaze angle of the grating. It is not possible to cover the complete energetic range with just a single grating with a single blaze angle, since the diffraction efficiency drops relatively quick when rotating the gratings away from the the perfect blaze angle. A detailed study can be found here [35]. In our case we are using three gratings with the parameters given in table 3.2. To illustrate the relation between groove density, blaze angle and transmission the rotation angle versus the center energy, or wavelength, is plotted in figure 3.4.

A range of ± 1.5 °around the perfect blaze angle is marked by the shaded areas. This assumes that the diffraction efficiency drops symmetrically around the blaze angle. In this region the transmission efficiency through the complete monochromator is high. In regions where the slope in the rotation angle versus energy is small, the energy resolution is worse. We can separate the energy scale into three regions. From 10 eV to 22 eV the 150 gr/mm is the optimal one. From 22 eV to 30 eV the 300 gr/mm grating is optimal. From 30eV to 50 eV the 600 gr/mm grating is optimal.

3.2.4 Energy Resolution

In this section the expected energy resolution is estimated. For the ray that is travelling perfectly in the horizontal plane of the monochromator the relation $\gamma = \gamma'$ holds. The corresponding wavelength and the rotation angle of the grating are then connected by the grating equation

$$\lambda_c = 2 \sin \alpha \sin \gamma_c / \sigma \tag{3.10}$$

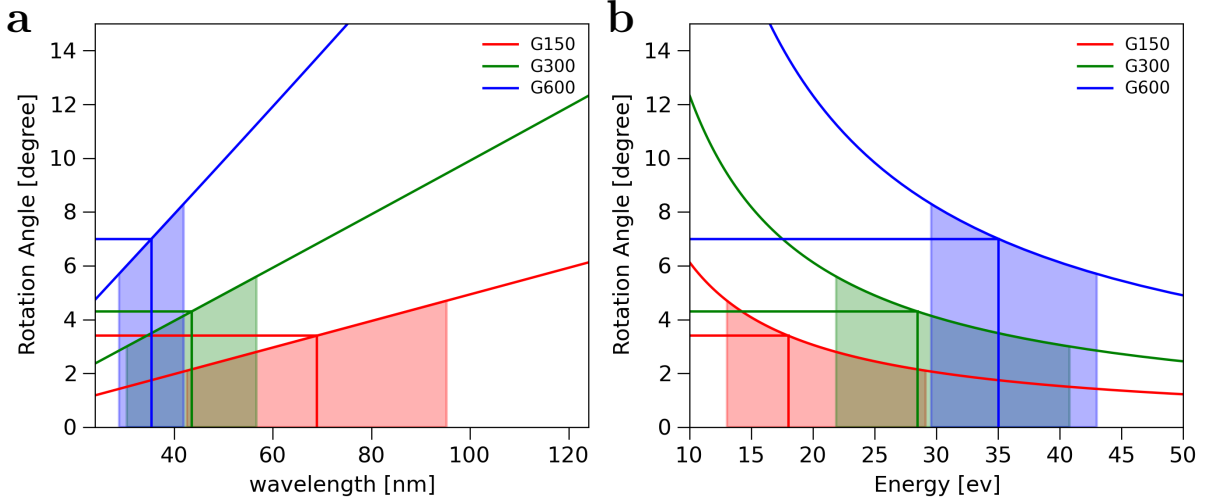$$\gamma_c = \sin^{-1} \left(\lambda_c \sigma / 2 \sin \alpha \right) \tag{3.11}$$

Figure 3.4: a: Rotation angle vs. wavelength for all three gratings. The horizontal solid lines indicate the rotation angles where they are equal to the blaze angle of the grating. The shaded areas indicate a range of ± 1.5° around the blaze angle. In these regions the gratings have the highest diffraction efficiency. **b:** Same plot, but rotation angle versus energy.

where λ_c is labeled as the center wavelength of the transmitted pulse, that is chosen by rotating the grating. The energy resolution is defined as the minimal bandwidth of the transmitted pulse, when the slit goes to zero width. If everything would be perfect only the center wavelength would be transmitted through the slit. However there are three effects allowing also rays with different wavelength to be transmitted through the same virtual slit

- The entrance slit width of the monochromator: In our case this is the width of the XUV source. Generally the XUV spot size in the HHG focus depends on the emitted XUV energy. However in the present estimates this effect is neglected and the source size is assumed to be half the IR focal spot size. We assume that the spot size has a Gaussian distribution with the FWHM diameter $w_{entrance}$.

- The aberrations in the imaging from HHG focus to slit focus: We approximate the aberrations by assuming that a perfect point source in the HHG focus would be focused on a round spot. We furthermore assume that the aberrations are wavelength independent and that the spot has Gaussian profile shape with the FWHM diameter $w_{aberrations}$.

- The spatial resolution of the grating diffraction pattern: In case of Frauenhofer diffraction for a grating with N slits the FWHM width of the Gaussian-shaped center spot of the intensity profile for the first diffraction order in the focal plane of a lens is given by [36]:

$$w_{diffraction} = 2.75 \cdot \lambda/(N \cdot \pi \cdot d \cdot f) \tag{3.12}$$

All three effects lead to a broadened focus in slit plane with an approximately Gaussian intensity profile. The resulting intensity profile of the combination of the three effects is determined by the convolution of the three individual intensity profiles resulting in the FWHM focal diameter of:

$$w_{sum} = \sqrt{w_{entrance}^2 + w_{aberrations}^2 + w_{diffraction}^2} \tag{3.13}$$

The broadened focus translates into a minimal spectral bandwidth that is transmitted through the (infinitely small) slit in the following way: We assume that a given XUV wavelength is diffracted from the first grating under a fixed angle defined by the grating equation 3.7. The wavelength that is exactly focused in the slit will be labeled λ_c. The broadening of the focus in the slit plane also allow parts of beams associated with rays corresponding to different wavelengths than λ_c to be transmitted through the slit. The two rays traveling through the (FWHM-)edges of the broadened focus in the slit plane correspond to two different wavelengths, labeled λ_+ and λ_- therefore define the minimal spectral width of a transmitted pulse:

$$\Delta\lambda(\lambda_c) = \lambda_+ - \lambda_- \tag{3.14}$$

The wavelength associated with the two rays can be deduced from the geometry of the optical layout and the grating equation 3.7 in the following way. The angle between the center ray (corresponding to λ_c), that travels perfectly in the horizontal plane of the monochromator, and two rays corresponding to the edges of the broadened focus is given by

$$\Theta_\pm = (w_{sum}/2)/R \tag{3.15}$$

where R=0.8 m is the focal length of the toroidal mirror and w_{sum} is the diameter of the broadened focus and w_{sum} is small with respect to R. The center wavelength λ_c corresponds to the rotation angle γ_c of the grating. The angle between the rays translates into a slightly different angles between incident and outgoing beam in the ($\gamma \neq \gamma'$) grating equation. For small angle approximation the relation

$$\gamma'_\pm = \Theta_\pm/\alpha \tag{3.16}$$

holds [2] and the corresponding wavelengths are given by:

---

[2] The relation between the real angle between two rays and the angle in the cone plane is not trivial and if the small angle approximation is not applied, it reads

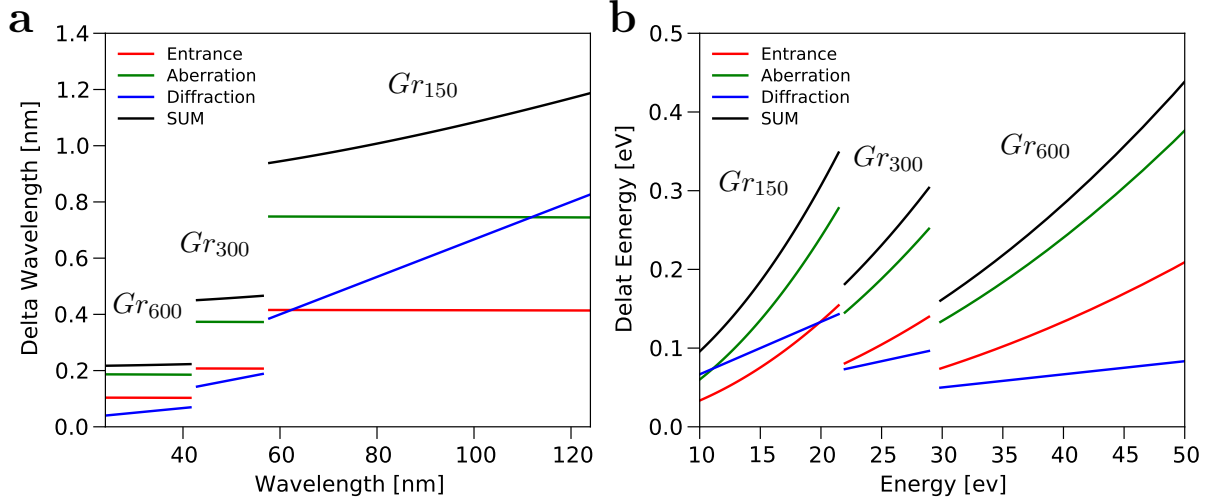$$\tan(\Delta\Theta/2) = \frac{\sin(\Delta\gamma/2)}{\cos(\Delta\gamma/2) + 1/\tan(\alpha) - 1} \tag{3.17}$$

Figure 3.5: a: Wavelength resolution versus center wavelength. The three regions correspond to the individual gratings that have the highest diffraction efficiency in these wavelength regions. The individual contributions to the total wavelength resolution are given. The total sum is the convolution of the three distributions that are assumed to be Gaussian. **b:** Energy resolution versus center energy. The total energy resolution is dominated be the aberrations in the imaging.

$$\sin\alpha(\sin\gamma_c + \sin\gamma'_\pm) = m\lambda_\pm\sigma \tag{3.18}$$

We now present a simulation of the energy resolution using experimentally obtained values for $w_{entrance}$, $w_{aberrations}$ and $w_{diffraction}$:

- During the alignment of the monochromator we measure an FWHM diameter of the IR focus at the position of the HHG cell of about 100 μm. Since we assume that the spatial region we the XUV light is generated is about half the size as the IR focus diameter and wavelength independent this results in $w_{source} = 50\ \mu m$.

- During the alignment of the monochromator layout we are able to image a 100 μm pinhole spot in the HHG focus onto a Gaussian spot of 135 μm in the slit focus. If we assume that the aberrations have a Gaussian shape, the spotsize in the HHG focus is convoluted with the aberrations. This results in a diameter for the sport size originating from spatial aberrations of $w_{aberations} = 90\ \mu m$. It is unclear if the aberration are originating from a misalignment of the optical elements in the monochromator or are an intrinsic limit of the toroidal mirrors.

- The XUV divergence coming from the HHG focus is constant for almost all XUV energies [37] and is about 0.2 of the divergence of the IR beam. We observe an IR mode with about 5 mm diameter (FWHM) on the first grating and conclude that the

37

mode diameter of the XUV beam is about 1 mm. The number of illuminated groves N depends on the chosen grating groove density and with equation 3.12 the diameter $w_{diffraction}(\lambda)$ in the slit plane can be calculated

In figure 3.5 the energy resolution for the given parameters is presented. For the individual gratings only the regions with high diffraction efficiency of the gratings are shown. This is done in agreement with the assignment of optimal energetic transmission regions of the specific gratings in the previous section. The impact of aberrations and the HHG source width is almost constant for different wavelengths. In the plot of resolution against energy it becomes evident that different gratings with different groove densities are necessary to cover the complete energy range, while at the same time keeping a comparable energy resolution. According to our estimates the limiting effect are the aberrations in the system. The impact of the XUV source width and the spatial resolution of the diffraction pattern of the gratings is almost negligible. This also justifies the assumption that the XUV source width is constant over the covered energy range. The calculated values have to be taken with caution, since we assumed for all of them to all have a Gaussian distribution, which might not necessarily be realistic. This will be discussed again in section 5.2 where experimentally obtained results on the energy resolution are presented.

3.2.5 Time Resolution

The time resolution of a pump-probe experiment is determined by the pulse duration of the two pulses, in our case the IR pulse and the XUV pulse at the output of the monochromator. The XUV pulse duration hereby depends on the IR pulse duration, as already described in the section 3.1 on the relation between the APT and the filtered XUV pulse duration, the settings/layout of the monochromator and the alignment of the monochromator. In this section we concentrate on a single factor, namely the dependency of the minimal possible XUV pulse duration on the the slit width and the optical layout of the monochromator. Other dependencies are only briefly discussed.

If we neglect the chirp of the XUV pulses coming from the HHG source, the fundamentally shortest possible pulse duration is limited by the bandwidth of the transmitted pulse. If we assume Gaussian pulse shapes in time the relation between bandwidth and time is given by the time-bandwidth product [38].

$$\Delta\tau = \frac{0.44h}{\Delta E} \tag{3.19}$$

where h is Planck's constant. In order to shorten the pulse duration the bandwidth of the transmitted pulse has to be increased, which directly corresponds to an increase of the slit width. However an increase of the slit width results in a larger residual delay between the outermost rays traveling through the edges of the slit. This effect should not be confused with the tilting of the pulse front induced by the first grating. The second stage compensates this delay between the spatial edges of the pulse. The effect discussed
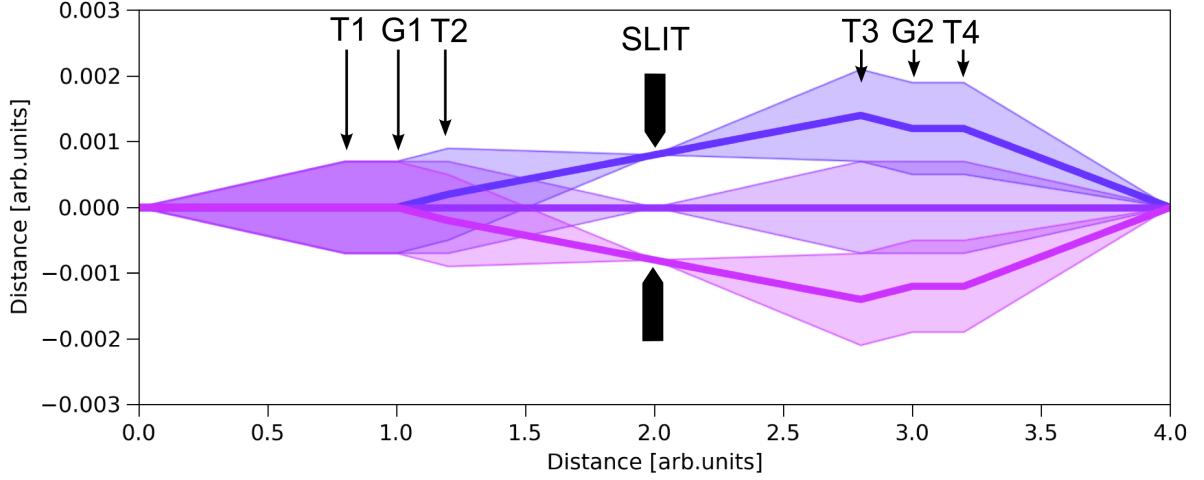
Figure 3.6: Ray-tracing image of the monochromator. All optical elements are replaced by transmission optics. This approximation is valid for small differences in diffraction angles from the first grating. The thick lines with different colors indicate the center rays corresponding to different XUV energies that are transmitted through the slit. The shaded areas indicate the beams corresponding to the individual center rays. The differences in path length between the center rays corresponding to different XUV energies translate into a residual delay between the energies. This stretch in time is not compensated by the symmetric layout of the monochromator.

here is additional and can not be overcome and shall be explained in more detail in the following: To properly quantify this residual stretch of the pulse we are simplifying the optical layout of the monochromator by replacing all optical elements by transmitting optics. This assumption is feasible since the conical shape of the diffraction pattern can be neglected for the small angle differences we are dealing with in this situation. The diffraction pattern is spread in the vertical plane of the monochromator. A simple ray-tracing image of the described effect is presented in figure 3.6.

It shows the three rays corresponding to the middle and the two edges of the bandwidth of the transmitted pulse. The center of the individual beams is marked by a thick line. One directly observes that for different energies the total distance traveled through the complete setup is not equal. The center wavelength travels the shortest distance, which is exactly 4 m. The other two rays are slightly longer. The ray-tracing model takes the realistic distances and the delay can directly be calculated from the differences in distances. The diffraction angle of the beam coming from the first grating is calculated in complete analogy to the estimate of the energy resolution, replacing the finite width of the focus in the slit plane by the width of the slit. Aberrations are neglected for this calculation.

In figure 3.7 we present the calculated scaling for a given center energy at 42.3 eV and the 300 gr/mm grating, as an example. For a slit width larger than 600 μm the bandwidth of the pulse is still increased, however the pulse duration will get longer again. This sets an
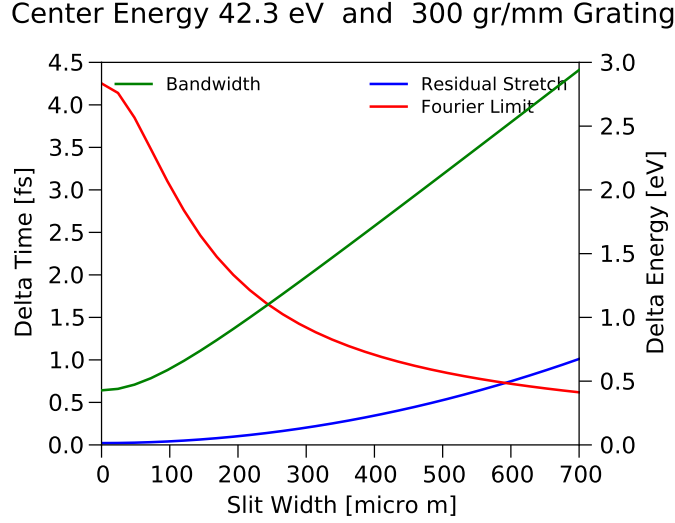
Figure 3.7: The plot shows the interplay for an example pulse with center energy at 42.3 eV for a sample. For an increasing slit width the transmitted bandwidth through the slit of the monochromator is increasing. The larger bandwidth corresponds to a shorter pulse duration, if the pulse is bandwidth limited. At the same time the residual stretch is increasing with a larger slit width. At a slit width of 600 μm an increase of slit width does not pay off anymore. As an absolute fundamental limit the monochromator cannot transmit pulses with a pulse duration below 0.6 fs.

absolute fundamental limit to the pulse duration of 0.6 fs. For other gratings and varying center wavelengths this value is quite stable and only varying in a range of about 0.2 fs. It should be pointed out that in decrease of the focal length of the toroidal mirrors would also decrease the induced stretch, however in practice we are not reaching these fundamental limits yet, and are rather limited by the alignment and the aberrations in the system. There are various publications dealing with the impact of the aberrations of toroidal mirrors on the pulse duration, since this is of special interest when dealing with attosecond pulses. To quantify these stretches, the monochromator has to be ray-traced completely in all 3 spatial dimensional. This has not been done so far for our case, but a general discussion about the influences of a misalignment of elements can be found here [20].

Additionally it has to be kept in mind, that reaching this Fourier limit would require a mechanism to compensate the linear chirp in the XUV pulse coming from the HHG process. A possible strategy for this is discussed in the outlook section 5.5. After this introduction to the general concept of a TDCM and a presentation of the interplay between the various performance aspects of the design we will now introduce the newly constructed experimental setup.
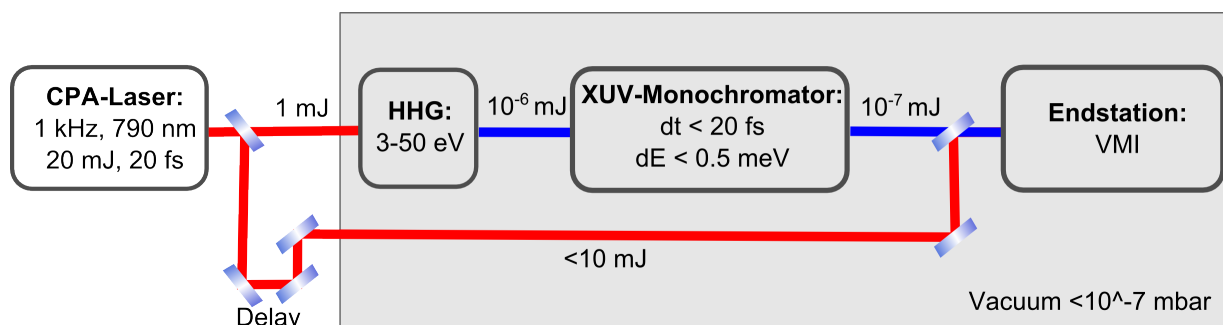
Figure 3.8: Complete overview of the experimental setup. A short IR pulse delivered by the commercial laser is split into two parts at the beginning of a pump-probe setup. One arm of the setup is guiding a part of the pulse to directly to the experimental endstation. In the other arm XUV radiation is generated via High Harmonic Generation (HHG). The XUV light is subsequently spectrally filtered by a Time-Compensating Monochromator (TDCM). The monochromator is designed to provide good energy and time resolution delivering almost bandwidth-limited pulses in the energy range from 3 eV to 50 eV with pulse duration below 10 fs. The XUV and IR pulses are recombined to perform time-resolved pump-probe gas-phase photoelectron and photoion spectroscopy with a velocity imaging spectrometer (VMI).

3.3 Technical Implementation

This section describes the technical implementation of the complete beamline. A schematic overview of the different constituents is given in figure 3.8. The laser system is a commercial system and only the output parameters are summarized here. The IR pulse coming from the laser is entering a pump-probe setup where one arm consists of the HHG source plus the XUV monochromator and the other arm only transmits the IR pulse. As a spectroscopic endstation a velocity imaging spectrometer (VMIS) is used throughout this thesis. The VMIS was adopted from another beamline and is only described briefly here.

The conceptual planning, design and implementation of the various parts of the beamline was done by the author and took more than two years until first signals could be detected in the VMIS. Most parts were pre-designed with the CAD software Autodesk Inventor and all the rendered 3D images presented in this chapter are produced with this software. Technical details of some parts are also designed by our internal workshop or external companies. It will be marked who was involved in the production of the individual parts. Although this section is kept short it should be pointed out that it actually corresponds to a large amount of work in the laboratory. The alignment of the system is described in a separate chapter.

3.3.1 Laser System

The laser system is a commercial state-of-the-art chirped pulse amplification (CPA) laser (Amplitude Systems) that provides ultrashort pulses in the IR, with a central wavelength

at 795 nm. It has a dual output delivering pulses with 1 kHz or 10 kHz repetition rate with the pulse energy being either 20 mJ or 2 mJ. The pulse duration in both arms can be varied between 20 fs and 35 fs. Additionally the system offers the possibility to stabilize the carrier-envelope offset (CEP) of the pulses. This feature is not used for the experiments presented in this thesis.

Roughly 4-5 mJ of pulse energy are sufficient to easily operate the experiment in the current status without having to take care about all possible energy losses in the optical layout. This is beneficial during the setup phase. Therefore the 1 kHz output of the laser is used so far. For experiments with lower pulse energy requirements in the IR arm also the 10 kHz output of the laser could be used in the future. This would decrease the data acquisition time. The 20 mJ/1kHz output is shared with other experimental installations by means of a broadband dielectric beamsplitter. Typically 10 mJ are available for the experiment. The pulse characteristics are adjusted for each experiment individually and will be given with the description of the experiments.

3.3.2 Optical Layout Outside Vacuum

The optical layout of the pump-probe setup outside the vacuum chambers is shown in figure 3.9. The incoming pulse is split by a beamsplitter into two arms. About 70 % of the energy is transmitted and is used as one arm of the pump-probe setup and will be labeled the IR arm (red). The reflected beam (blue) is used for the XUV generation.

The mode diameter of the IR arm is telescoped down to a size of about 2 cm. The IR size is determined by the geometry constraints of the IR beam inside the vacuum system, which is designed to house a beam with 2 cm diameter. A large IR mode will be beneficial when the beams are recombined at the end of the pump-probe setup. By tuning the telescope distance, the final focus of the IR beam in the experimental chamber can be shifted along the beam direction and can be adjusted to the experimental requirements. The IR arm passes over to a delay stage with a range of about 1 ns and a time resolution of about 6 fs, which is sufficient for the current requirements of the experiments. The pulse energy can be tuned by the combination of a $\lambda/2$-wave plate and a thin film polarizer. After this section a second $\lambda/2$-wave plate is used to tune the polarization to the final experiment. Next the mode is cleaned with the help of an iris, that is slightly clipping the edges of the beam. Finally the beam is periscoped from a height of 11 cm to 26.5 cm. The new height is defined by the geometry of the beam inside the vacuum system, which is 19.5 cm above the optical table. The vacuum system is placed on a different table that is about 7 cm higher than the optical table housing the part of the pump-probe setup that is outside the vacuum. The total arm length of the pump-probe setup inside and outside the vacuum is more than 6 m.

The XUV arm is telescoped down to a mode diameter of about 1 cm. Its power can be tuned by a combination of $\lambda/2$-wave plate and a thin film polarizer. For this arm it is especially important to be able to tune the power without changing the mode diameter. The power needs to be tuned to optimize the phase matching of the HHG process, at the same time the beam geometry of the HHG source has to be stable in order to not change
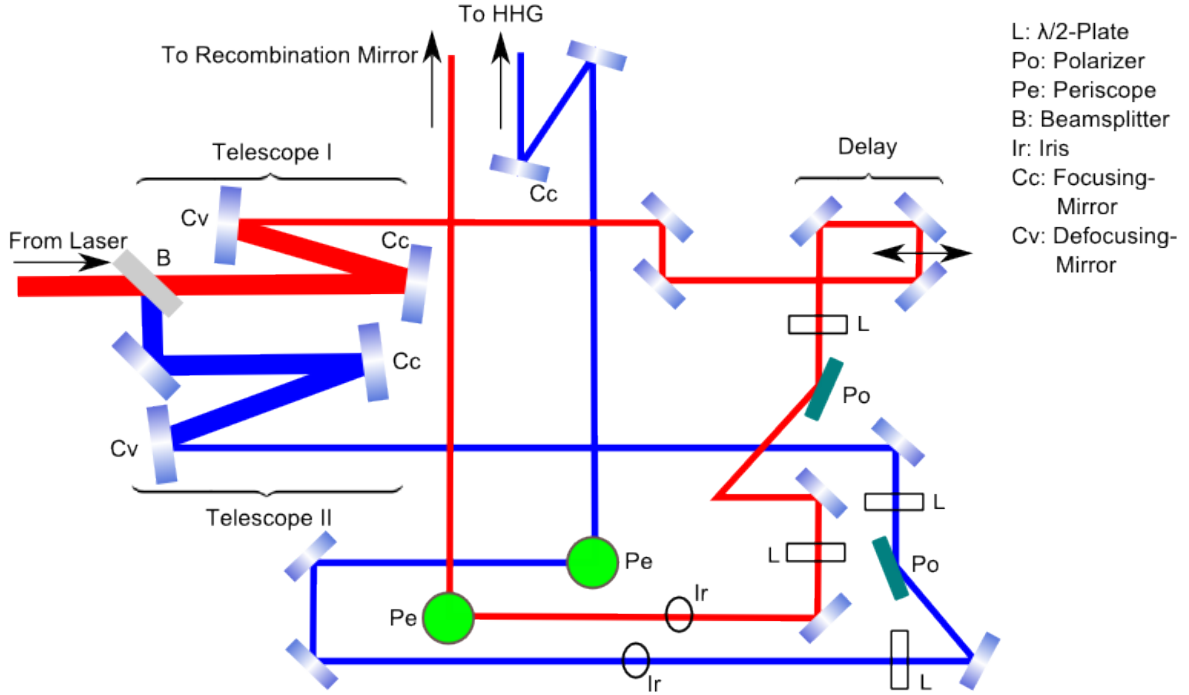
Figure 3.9: Optical layout of the pump-probe setup outside the vacuum system. The pulse from the laser is split into two arms. Both arms a telescoped down to reduce the mode diameter. The IR arm (red) can be delayed and tuned in power. The power tuning is done by a combination of $\lambda/2$-wave plate and polarizer. The beam is then persicoped up and enters the vacuum system via a Brewster-window. The XUV can be tuned in power and is also periscoped to the height of the entrance window of the HHG chamber. It is then focused into the HHG chamber.

the XUV monochromator performance.

After the section that is tuning the power the polarization can be tuned by a second $\lambda/2$-wave plate to compensate small polarization changes that may be induced by the periscope. The mode is cleaned by an iris. The beam then has a mode diameter of about 7 mm to 8 mm. The beam height after the periscope is 22 cm. The XUV beam is focused with a focal length of 62.5 cm into the HHG chamber.

All optics used for the IR beams have a dielectrical coating. We will now continue with the main part of the setup and describe the optical layout of the pump-probe setup inside the vacuum system.

3.3.3 Vacuum System

In the overview figure 3.8 it is indicated that both beams are guided inside the vacuum after leaving the first part of the pump-probe setup that is described in the previous section 3.3.2. The vacuum beamline (and experimental endstation) are in a experimental room separated from the laser room. By guiding the IR close to the XUV beam and inside
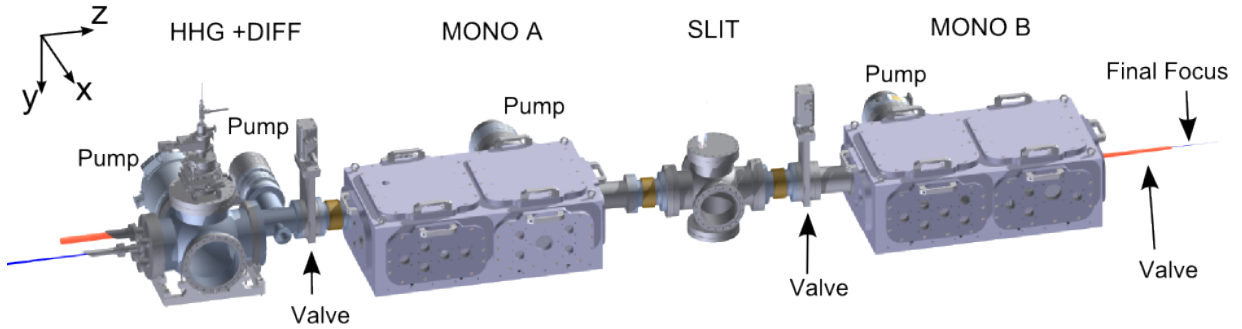
Figure 3.10: Complete exterior of the XUV-monochromator beamline. It is sectioned into four major parts. The first part is the HHG chamber, which is connected to the first stage of the monochromator by a differential pumping section. This part is labeled HHG+DIFF. The first section of the monochromator is labeled section MONO A. This is followed by a chamber housing the slit. At the end the second part of the monochromator follows. This is labeled section MONO B.

the vacuum chambers in the experimental room the stability of the pump-probe setup is increased, since this part is sheltered from the environmental conditions in the experimental room. The laser room is not entered during measurement runs and both temperature and air humidity are controlled more thoroughly in the laser room. This combination allows for stable measurement runs over days, while at the same time work in the experimental room on other experiments can be carried out. The complete exterior of the beamline is presented in figure 3.10.

The beamline is separated into four major sections. Namely the HHG generation chamber, the monochromator chamber MONO A, housing the first stage of the monochromator, the slit chamber (SLIT) and the monochromator chamber MONO B, housing the second stage of the monochromator. Between the HHG chamber and the first stage of the monochromator a differential pumping section is included to reduce the gas leakage from the HHG cell into the rest of the beamline. The experimental endstation is not shown. The HHG and the two monochromator chambers are separated by valves, making it possible to vent different parts of the experiment separately. The valves are motorized and can be controlled by an interlock system, that however currently is not in use yet. The complete system is pumped by four turbo molecular pumps listed in the following table:

The pressure in the four sections is monitored by separate vacuum gauges. The pressures can be tracked over time synchronized with other parameters associated to an experimental scan.

The HHG chamber and the slit chamber are standard vacuum pieces. The HHG chamber is a CF 200 5-way cross and the slit chamber a CF 160 6-way cross. The size of the HHG chamber is determined by the the size of the pump flange connection, which is a CF 200 connection in case of turbo pump we are using with a pumping speed of 1500 l/s. In order to have sufficient space to guide both beams through the system the chambers are

Name	Model	CF Flange	l/s	Pressure [mbar]
HHG	Turbovac MAG	DN 200	1500	$2.7 \cdot 10^{-4}$
Diff. Pump.	Turbovac MAG	DN 100	300	$1.0 \cdot 10^{-6}$
MONO A	Turbovac MAG	DN 160	600	$2.5 \cdot 10^{-7}$
MONO B	Turbovac MAG	DN 160	600	$2.0 \cdot 10^{-7}$

Table 3.3: Turbo molecular pump specifications of beamline and pressure in the different chambers. The gas pressure in the HHG cell is 53 mbar. All turbo pumps are purchased from Oerlikon.

connected by tubes with 10 cm inner diameter.

The two square monochromator chambers are custom made by the company ATLAS. They are made out of aluminum and each has eight rubber sealed doors. For the connection of the CF flange of the pump to the door a special steal to aluminum welding technique is used by the company. The doors are customized by our internal workshop by adding various KF sealed ports. This opens the possibility to add or change vacuum connections during or after the design of the interior of the chambers perfectly matching the inside arrangement of elements. It is also possible to completely manufacture new doors in the workshop if needed for future developments of the system. The possibility to completely remove the doors at the side is of great help during difficult phases of the alignment of the XUV monochromator. The top doors do not house any ports and can quickly be removed. This allows for quick access to almost the complete beamline at any time.

The base plates of the square chambers are 50.8 mm thick and equipped with a breadboard thread pattern, essentially providing an optical table inside vacuum. The thick base plates are minimizing the deflection of the breadboard between vented and evacuated chambers. This assures that the alignment of the optical elements that is performed during vented chambers is maintained when the chambers are evacuated. We simulated the stiffness of the base plate with a deformation calculation provided by the CAD software, resulting in less then 5 μm deflection of the center point of the base plate.

In terms of vacuum technology the only part that needs special attention is the differential pumping stage between HHG chamber and the first part of the monochromator. This is described now.

Differential Pumping and Optical Layout of HHG Chamber

Under typical experimental conditions the pressure in the HHG chamber can reach up to 10^{-3} mbar. In order to operate the multi channel plate (MCP) of the XUV spectrometer in chamber MONO A, the pressure needs to be, at least, reduced below 10^{-6} mbar. This is achieved by a simple differential pumping section. In figure 3.11 a horizontal and vertical cut through HHG chamber and differential pumping section is presented. Both IR beams are entering the HHG chamber via Brewster-windows in order to minimize power losses. Generally the complete beamline is designed to house a beam in the IR arm with 2 cm mode diameter. The XUV beam part is designed to house a beam with maximal size of 8
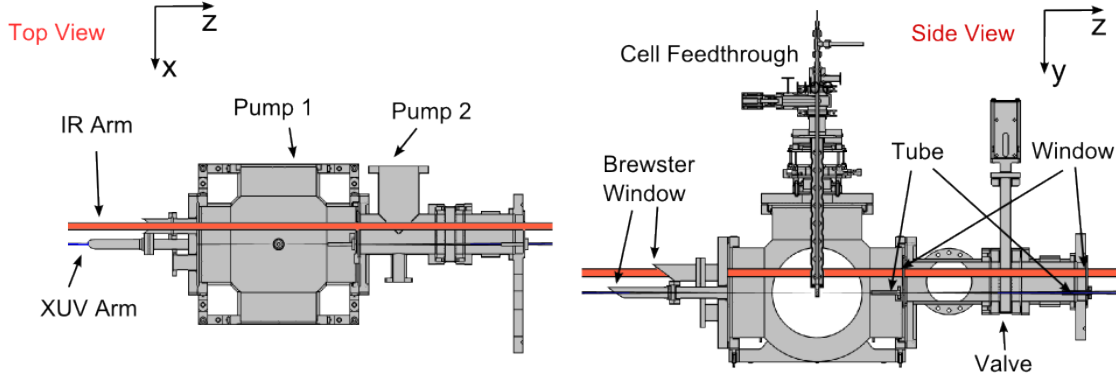
Figure 3.11: HHG chamber and differential pumping section. Both beams enter the HHG chamber via Brewster-windows. For the IR beam the differential pumping section is sealed by 200 μm thick glass windows. The XUV beam travels trough two tubes with inner diameter below 1 cm in order to reduce the gas leakage from HHG chamber into the rest of the beamline.

mm. The IR beam is 4.5 cm displaced to the side and 4.5 cm higher than the XUV beam.

The IR beam is entering the differential pumping section via a 200 μm thick glass window and is also leaving the section through another window. The differential pumping stage is therefore perfectly sealed off for the IR beampath. For effects on the IR pulse duration see section 4.

For the XUV beam we are reducing the pressure by guiding the XUV beam through small tubes that have a low gas conductance. The tubes can be manually pre-aligned to the XUV beam, both in angle and position. The freedom in alignment is crucial, since the XUV cannot be moved. Its direction is defined by the layout of the XUV monochromator. The conductance for a tube is given for molecular flow by [39] :

$$C_{tube}[l/s] = 12.1 \frac{d^3 \, [cm^3]}{l \, [cm^2]} \tag{3.20}$$

where d is the diameter of the tube and l the length. The pressure reduction is given by

$$a_{reduction} = \frac{C_{tube}}{S_{pump}} \tag{3.21}$$

where S_{pump} is the pumping speed of the pump. The actual parameters of the tubes are given in the table 3.4.

The different tube diameters take into account that the XUV beam is divergent when coming from the HHG source. A single tube might already be enough to reduce the pressure significantly. In practice the differential pumping stage works flawless, since we achive a pressure in chamber MONO A of less than $3 * 10^{-7}$ mbar under operation of the beamline. This is sufficient to operate the MCP in the chamber MONO A.

46

Wall	l [cm]	d [cm]	C_{tube} [l/s]	C_{pump} [l/s]	$a_{reduction}$
HHG to DIFF	10	0.6	0.26	350	7e-4
DIFF to MONO A	10	1	1.21	750	1.2e-3

Table 3.4: Specifications of the differential pump sections.
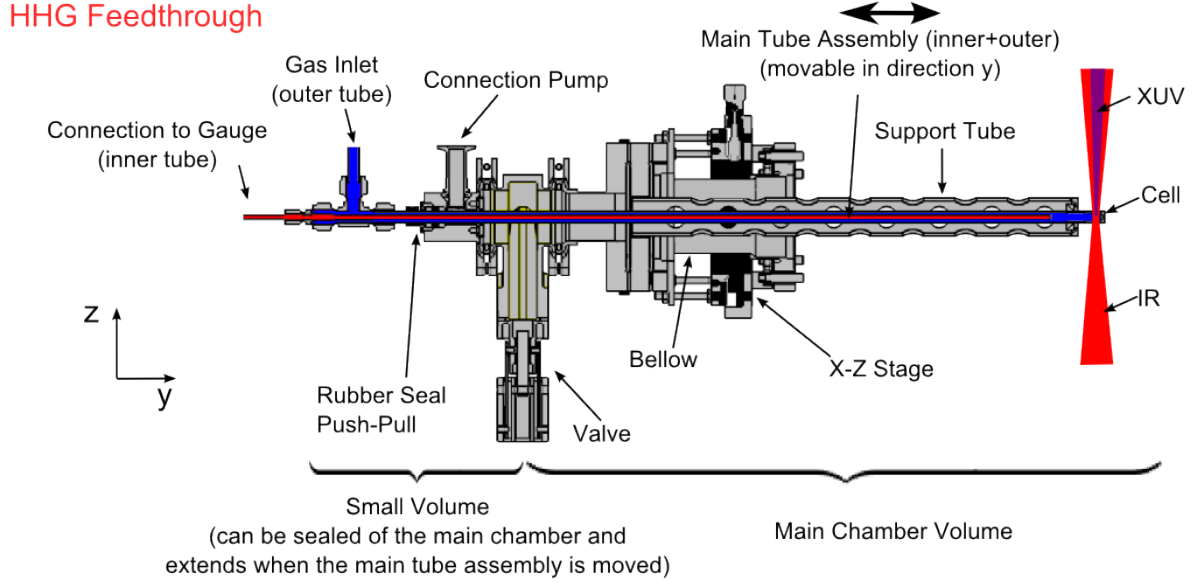
Figure 3.12: HHG cell with manipulator. Blue tube is the gas feedthrough into the vacuum. Red tube is connected to a pressure gauge, measuring the pressure directly in the gas cell. The complete assembly of red and blue tube can be moved out of the chamber in a volume that can be eVacuated separately. This allows for a change of the aluminum foil that is sealing the gas cell.

3.3.4 HHG Gas Inlet

The HHG process takes place in a gas cell. The gas cell needs to be aligned in all spatial dimensions to the XUV beam, since the XUV beam geometry cannot be changed and is defined by the monochromator layout. The manipulator holding the gas cell is presented in figure 3.12.

The cell is mounted onto the tip of a straight tube, which serves as the gas feed-through into the vacuum chamber. The cell is sealed with a thin aluminum foil (50 μm) from the vacuum chamber. With the first laser shot a small hole is burned in the foil, resulting in a perfect alignment of the laser beam to the hole. The complete tube is mounted on an x-y stage that allows to move the cell in the horizontal plane with a travel range of ± 5 cm and a precision of 0.1 mm. Two technical features of the manipulator should be emphasized.

Inside the tube guiding the gas (blue), a smaller tube is mounted (red). The red tube is connected to a pressure gauge allowing to measure the gas pressure directly in the gas cell, since there is no gas flow in the red tube.

Second the complete assembly of the red and and blue tube can be moved out of the HHG chamber in a separated small vacuum volume that can be sealed off from the main chamber by closing the valve. The position of the gas cell in the HHG chamber along the axis of the push and pull feedthrough is locked by a small pin, in order to reproduce the height of the cell after moving it in and out. This feature allows for a quick change of the aluminum foil that is sealing the HHG cell, without venting the main chamber.

The gas pressure in the main gas pipe is monitored and actively stabilized by a motorized valve that is controlling the flow. The system is a commercial control system from MKS systems and allows to keep the pressure in the HHG cell constant over long times. This is helpful, since the hole in the aluminum foil can increase when the measurement is running over days. The flow then has to be increased to keep the same pressure, and thus the perfect phase matching conditions in the cell. The cell length can have a maximum value of 1 cm, which is determined by the diameter of the blue tube.

3.3.5 Layout of Elements Inside the Beamline

The chambers MONO A and MONO B house the two stages of the TDCM and the IR arm of the pump-probe setup. We will first describe the general layout of all the elements inside the vacuum and then present the design of the individual elements. A general overview of all the elements inside the two chambers is given in figure 3.13.

XUV Arm

The optical path of the XUV arm is marked in blue. The optical layout consists of the four toroidal mirrors and the two gratings as introduced in section 3.2.1. In the figure the four toroidal mirrors are elements 5, 8, 15 and 18 and the two gratings are elements 7 and 16. The length and position of the chambers is defined by these main optical elements.

For the daily alignment of the XUV arm into the monochromator the irises 1 and 14 are used. They are monitored by cameras through the viewports a and c marked by the dotted red lines. The irises are set to a fixed diameter, such that the IR beam generating the XUV can be seen, but the XUV, which has a smaller divergence, is not clipped. The general initial alignment and the daily alignment will be described in more detail in a separate chapter 4.

A thin aluminium foil can be inserted into the XUV beam directly in front of the first toroidal mirror (5). It is mounted on a slide (3) that can manually be shifted by a push and pull feedthrough. The aluminium foil filters out the residual IR coming from the HHG source. This is helpful for various alignment steps, but it should be pointed out that during a normal experimental run the foil can be removed since the IR is also separated from the XUV by the first grating. We will especially mention when it is necessary to insert the foil.

1: Aligment Iris XUV I
2: View Mirror for 1
3: Slide for Al-Foil
4: View Mirror for 9
5: Toroidal I
6: Mirror for Backup
7: Grating Holder A
8: Toroidal Mirror II

9: Alignment Irirs IR II
10: IR Mirror I
11: IR Mirror II
12: XUV-Spectrometer
13: View Mirror for 14
14: Alignment Iris XUV II
15: Toroidal Mirror III
16: Grating Holder B

17: XUV Photodiode
18: Toroidal Mirror IV
19: Motorized Recombination Mirror
20: Slide for Screen & Outcople Mirror
21: Focusing Mirror IR
22: Motorized Steer Mirror IR
23: Periscope IR

Figure 3.13: Elements inside the chambers MONO A and MONO B. the XUV arm is blue, the IR arm is red. The dotted blue lines (e-g) indicate alternative routes for the XUV arm. The dotted green line (h) is a possible route that can be taken by the XUV and the IR arm (see text). The red dotted lines (a-d) indicate a possible monitoring of optical elements via viewports that are equipped with CCD cameras. The labels View 1 and View 2 refer to the view angle of the images presented in figure 3.14. For more details on all elements see the text.

View 1 View 2

Figure 3.14: View 1: Second half of chamber MONO A. The beams are traveling from left to right. If the gratings are moved out of the beam by the grating holder (7) the XUV beam hits the entrance slit of the XUV spectrometer (12). View 2: Second half of chamber MONO B. The beams are traveling from right to left. If the gratings are moved out 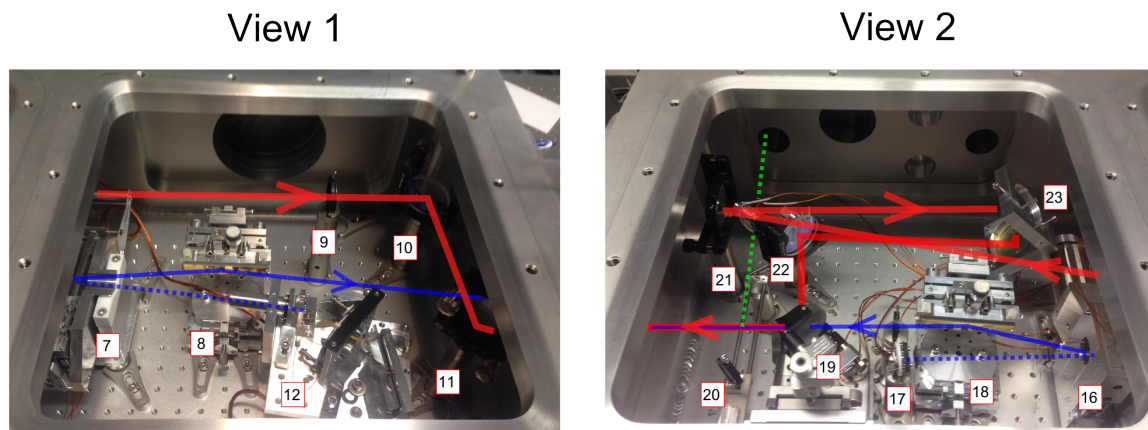of the beam the XUV beam hits the XUV photodiode (17). The IR beam is focused by mirror 21, is periscoped down by 23 and can then be overlapped with the XUV beam by the motorized mirrors 22 and 23. The XUV beam is passing through a hole in mirror 23. Mirror 23 can be moved in a plane perpendicular to the XUV beam in order to overlap the hole with the XUV beam. The slide 20 can move a mirror into the beam, to monitor the focus of both arms outside the chamber. This pathway is indicated green.

For diagnostic and alignment reasons the XUV beam can take four different routes that are marked in the figure as dotted blue lines e, f, g and one dotted green line . The routes f and g are for diagnostic purposes.

The gratings are mounted on a motorized linear stage and can be completely moved out of the optical path. When the collimated beam reflected from the first toroidal mirror is bypassing the first grating it directly enters a small XUV spectrometer (12). The complete XUV spectrum generated in the HHG source can be recorded. In figure 3.14a a picture of the second half of the chamber MONO A is shown. The normal path is indicated by the solid line and the route f as a dotted line.

In the chamber MONO B the XUV beam can take a second alternate route (g) when the second grating is moved out of the beam. In this case the beam hits a calibrated XUV photo diode, that measures the absolute XUV photo flux. This enables to quickly (< 20s) record the XUV pulse energy during a measurement run and is an absolutely crucial tool for the daily alignment and optimization of the monochromator. See also chapter 4 on alignment and chapter 5 on performance of the monochromator for more details.

The route e can only be taken by the IR contribution in the XUV arm (no aluminum filter) when the chambers are vented. The first toroidal mirror (5) can be manually moved

out of the beam. When the beam is not reflected by the first toroidal mirror it is deflected by a small mirror (6) and guided to the outside of the chamber where an iris is defining an additional alignment point. In combination with the iris (1) this gives two alignment points independent of the optical elements of the monochromator. Of course this route can only be taken for the IR beam coming from the HHG source, since the chambers are vented and the XUV would be absorbed by the air. Again see chapter on alignment 4, for more details.

The last route is h. With the slide (20) a mirror can be moved into the beam path after the recombination mirror and both XUV (only IR contribution) and IR can be guided outside of the chamber where the overlap between the foci can be diagnosed. This only works for the an IR contribution in the XUV arm transmitted through the monochromator when the gratings are operated in zero order and the aluminum foil is removed. The XUV contribution is absorbed in the window. Additionally a small screen can be moved into the beam with slide (20) and the overlap between the arms directly after the recombination mirror can be monitored by a camera via the viewport d. The alternate routes are also presented in figure 3.14.

IR Arm and Recombination

In figure 3.13 the IR beam is marked in red and it enters chamber MONO A 4.5 cm above and 4.5 cm to the side of the XUV beam. An iris (9) that is monitored by a camera via the viewport (b) fixes the beam alignment through the windows in the differential pumping stage. The beam is then manually aligned through the tube connecting chamber MONO A and MONO B with the two mirrors (10,11). The layout of the beam in chamber MONO B is presented in figure 3.14b. The beam hits a spherical focusing mirror (21) (f=125 cm) under a small incident angle, to minimize aberrations. The focused beam is periscoped down (23) incidence to the beam height of the XUV arm. Two motorized mirrors (22,19) are then used to overlap the IR beam with the XUV. The second mirror (19) has a small hole (3 mm) in the middle, such that the XUV beam can pass through it from the back without clipping. The recombination mirror is mounted onto two motorized linear stages in order to align the hole position to the XUV beam. The steering of the IR arm is done by tilting the mirror, which is motorized. Together with the first mirror (22), the complete pointing of the IR arm can be controlled. The whole path of the IR beam through the chamber is designed to preserve the polarization of the beam. This is necessary since the polarization is already defined by the orientation of the Brewster window.

3.3.6 Toroidal Mirror Holder

A picture of the toroidal mirror holder is presented in figure 3.15 on the left side. The toroidal mirror holders are commercially purchased from ALCA and offer a few possibilities for alignment marked in the image. The mirror can be tilted around all three spatial dimensions that are labeled yaw, pitch and roll. The mirror can be moved in height (y) and horizontally in and out of the beam in direction x. After aligning the mirror the
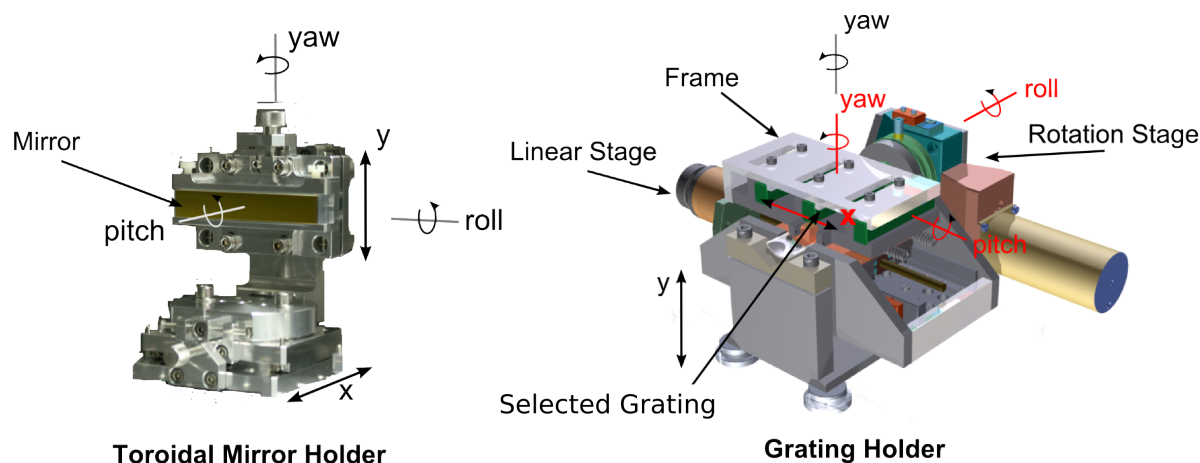
Figure 3.15: Toroidal mirror holder and grating holder. The adjustment angles of the grating frame with respect to the rotation stage are labeled in red. The overall adjustment angles of the grating holder with respect to the mounting surface are marked in black.

positions can be fixed permanently with small set screws. The alignment of the yaw angle of the mirror is too imprecise and a cross talk into other angles can be observed. We keep the angle fixed and rotate the complete assembly instead. This turns out to be more precise and stable. The complete assembly is fixed to the floor of the chamber with clamps. We furthermore altered the holders by implementing small set screws as position markers for the movement in direction x, marked in the image. This allows to move the mirror in and out of the beam without losing the initial alignment. The general alignment procedure for a toroidal mirror is relatively simple and described in chapter 4.

3.3.7 Grating Holder

The grating holders are the most challenging technical part of the monochromator. They have to fulfil two tasks. The holders should provide the possibility to quickly change between the three gratings in the beam path. This feature requires motorization in order to also work under vacuum conditions. At the same time the holder shall rotate the selected grating precisely around its conical axis in order to transmit the desired XUV center energy through the monochromator. Additionally the holder size is limited by the IR arm that is traveling next to the XUV beam, with the IR being 4.5 cm sideways and 4.5 cm higher above the XUV arm. This imposes strong spatial limitations on the design. We chose to completely design and assemble the holders ourselves. A CAD drawing of the holder is presented in figure 3.15 on the right side. The alignment angles and translation degrees of freedom of the complete holder with respect to the chamber are labeled in black and the alignment angles of the gratings with respect to the holder in red.
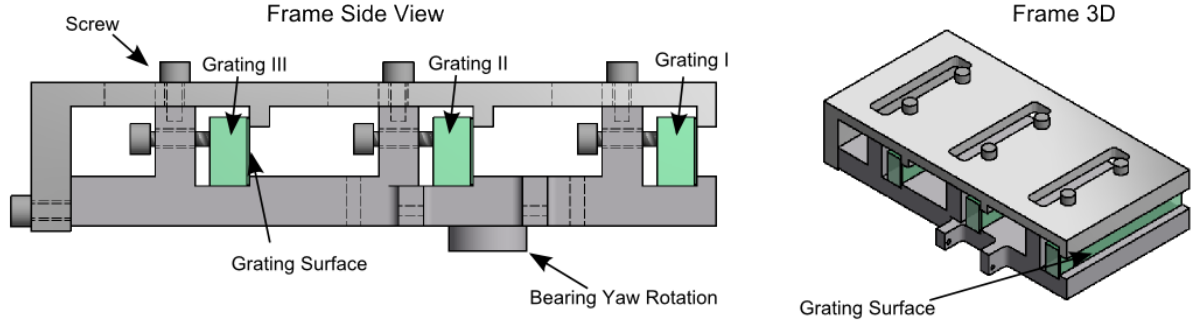
Figure 3.16: Frame housing three gratings (green). The grating surfaces are pressed against the lips of the frame from the back. All three grating surfaces normals are pointing in the same direction within the mechanical precision of the grating holder.

The main components are two motorized stages. A vacuum compatible linear stage (PI-micos, LS-65) can move the three different gratings into the beam along the dimension x. The gratings are mounted in a frame each with its surface normal pointing into direction x. For a given position of the linear stage the conical axis of one of the gratings overlaps with the rotation axis of a motorized rotation stage (PI-micos, DS-65 N). The rotation stage rotates the whole assembly of linear stage and gratings around the roll axis in order to select the desired center energy.

The frame, see figure 3.16, ensures that the surfaces normals of the three gratings are pointing in the same direction. It is built from two L-shaped pieces of aluminium. The grating surfaces are pushed from the back against the lips of the frame and within the mechanical precision of the frame all surfaces normals are pointing in the same direction. The frame has to be aligned to the rotation stage, such that the conical axis of the selected grating overlaps with the rotation axis of the rotation stage. The adjustment angles of the frame with respect to the linear stage are marked in red. The yaw and pitch angle need to be pre-aligned and the position x corresponding to the individual gratings needs to be calibrated. This is challenging and will be described in detail in the alignment chapter 4.

The alignment angles of the complete holder are marked in black, see figure 3.15. The incident angle (yaw) of the XUV beam onto the grating is aligned by manually rotating the complete holder and fixing it with clamps to the chamber floor. The height of the gratings can be adjusted by choosing feet with appropriate height.

To relieve the torque from the rotation stage around the pitch angle the whole assembly of linear stage and frame is supported on the opposite side of the rotation stage by a simple bearing. Additionally the torque around the roll axis has to be kept minimal. Therefore the linear stage assembly should be balanced in weight on both sides of the rotation axis. The torque is close to the specifications of the rotation stage and special attention has to be paid to the acceleration settings of the rotation step motor. The whole assembly should accelerate slowly in order to avoid any jumps between steps, which would spoil the calibration of the roll angle.
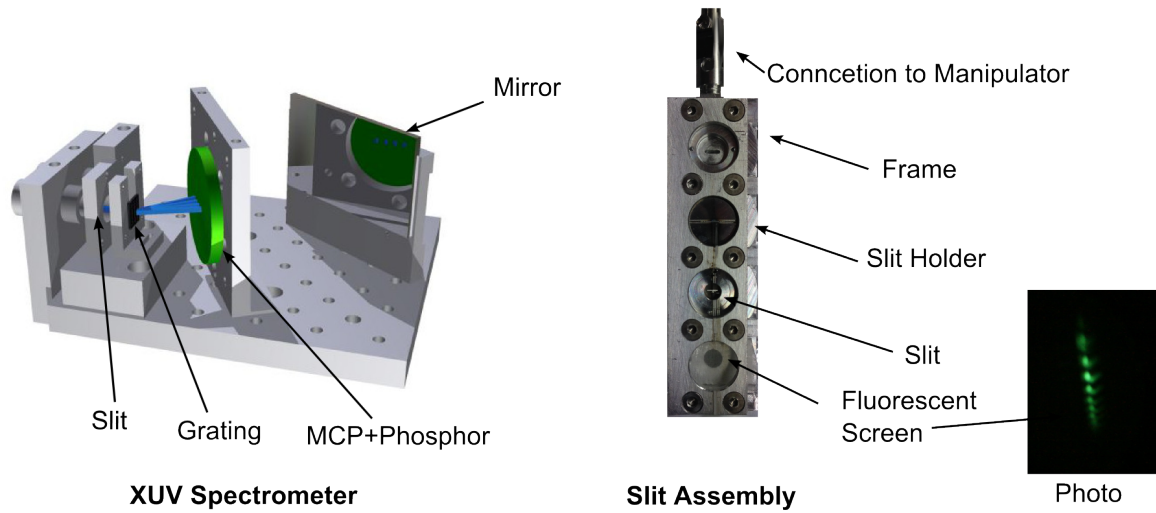
Figure 3.17: XUV spectrometer and slit assembly. The photo shows the diffraction pattern of the beam coming from the first grating on a fluorescent screen moved to the focus at the slit position.

3.3.8 Slit Assembly

The slits used in the present state of the experiment have a fixed width. This allows to reproduce the width reliably and avoids additional calibration. The slits are home built with razor blades that are spot welded on a small holder. The width is measured with a microscope. The slits are mounted into a frame that can house up to four slits. A picture of the frame housing the slits is presented in figure 3.17 on the right side. The frame is vertically sliding on rails in the slit chamber and is moved by a motorized push-pull feedthrough. Currently the slit widths used are:

Label	S1	S2	S3	S4
Width [μm]	48	109	207	650

Table 3.5: Currently implemented slits with fixed width in the the slit holder.

Alternatively a fluorescent screen can be mounted instead of a slit to observe the diffraction patter of the XUV in the slit region. An photo of the diffraction pattern in the screen is shown in figure 3.15.

3.3.9 XUV Spectrometer

The XUV-spectrometer has a footprint of about 15 cm x 10 cm. It consists of an entrance slit with 50 μm width followed by a transmission grating with a grating spacing of 100 nm. The diffraction pattern is recorded by a multi-channel-plate (MCP) in combination with a phosphor screen. The image on the phosphor screen is recorded by a CCD camera situated

outside of the vacuum chamber. A detailed description of the spectrometer is found in [40] and the calibration procedure is explained in [41] and [42]. The spectrometer records the full XUV spectrum generated in the XUV-source and is a helpful tool while optimizing the HHG process.

3.3.10 Velocity Map Imaging Spectrometer

The velocity map imaging spectrometer (VMIS) only differs from the standard implementation [43] by having a gas inlet included into the repeller. This inlet close to the interaction region of the spectrometer allows higher gas densities in comparison to a conventional molecular beam. The MCP in the spectrometer can be gated with a time resolution below 300 ns and in combination with a flight tube length of 26 cm this allows to mass select the ionic fragments generated in the interaction region. The VMI images presented throughout this thesis show a 2D cut through the 3D momentum distribution of the generated charged fragments. The momentum cuts are reconstructed from the raw data by using the BASEX [44] routine to perform the Abel-transformation. The 3D momentum distribution is hereby reconstructed from the 2D cut by exploiting the cylindrical symmetry of the generated fragments around the laser polarization axis, which is a necessary requirement in order to perform an Abel-inversion. The presented images are always oriented such that the linear polarization of the electric field of the optical pulses is vertical. If an angular integrated momentum or energy distribution is presented this refers to full integration over the 3D momentum distribution.

4 Alignment and Calibration of the TDCM

In this chapter the alignment of the XUV-monochromator is presented. The alignment of the monochromator can be separated into two main tasks. The first task is the initial set-up, which consists of the pre-alignment of each optical element and the alignment of the complete optical layout. The second task is the day-to-day alignment of the optical beams that is necessary to reproduce the initial conditions after the set-up phase.

The degree of accuracy in the alignment of the monochromator directly translates into the performance specifications that are achieved. A proper alignment of the optical layout reduces the aberrations in the imaging to a minimum, which is crucial if the high requirements in time and energy resolution that are set for the beamline have to achieved. In addition to the aberrations also the symmetry between the two stages determines the degree of recompression that can be achieved in the second stage. A general discussion on the influence of the misalignment of an individual element in the optical layout, grating or toroidal mirror, on the final pulse duration is presented in [20].

Additionally to the proper alignment of the optical layout, there are also more practical alignment issues that influence the usability of the beamline for experiments. The major task here is to pre-align the grating holders correctly in order to cover all the XUV energies between 10 eV and 50 eV in an experimental run without having to re-align the IR arm of the pump-probe setup. The ability to not only spectrally narrow the XUV pulse but also to vary the center energy is the great advantage of the beamline. Another practical issue is the day-to-day alignment. The degree of reproducibility that can hereby be achieved reduces the daily time to set up the beamline.

4.1 Alignment of Grating Holders

The pre-alignment of the grating holders is a stand alone problem and absolutely crucial for the performance of the complete monochromator. The technical requirement for the holder is to keep the pointing of the beam, that will travel through the slit, stable when the holder is switching between different gratings or rotates a single grating in order to select a different XUV energy. Because the XUV light is spectrally filtered by the slit in the focus of the second toroidal mirror, we weaken the requirement by only expecting that the angle of the outgoing beam should be stable. A lateral displacement does not lead to a shift of the focal spot, however when the torrodial mirrors are not hit in the center, the aberrations are increased and the total distance the beam travels through the monochromator is changed, which shifts the delay between pump and probe pulse in a time-resolved experiment. We therefore also try to keep lateral displacements small.

rc: con. diff. radius before rotation   x: horizontal displacement
rc': con. diff. radius after rotation   φ: precession angle
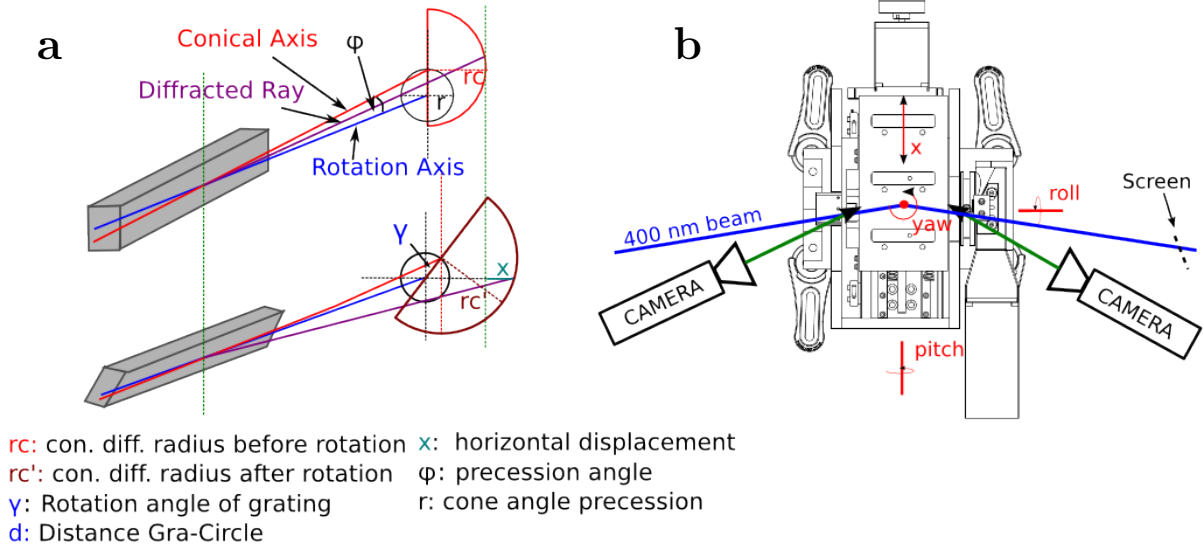γ: Rotation angle of grating   r: cone angle precession
d: Distance Gra-Circle

Figure 4.1: a: A misalignment between the conical axis of the grating and the rotation axis of the grating holder leads to a precession of the conical axis when the grating holder rotates the grating. This also leads to a change of the cone angle. In the horizontal plane this leads to a change of the pointing of the outgoing beam given by equation 4.1. **b:** The experimental setup used to align the pitch and yaw angle of the frame and the linear stage positions x for the the individual gratings: For the alignment of yaw angle and x positions the front edges of the gratings are monitored from both sides by a CCD camera. The exact procedure is described in the text. For the alignment of the pitch angle a 400 nm beam is diffracted from the 150 gr/mm grating and the diffraction pattern is monitored on a screen behind the gratings holder.

Technically the requirement of a stable outgoing beam pointing translates into the problem of overlapping the conical axis of the gratings with the rotation axis of the rotation stage. When the gratings are not perfectly rotated around their conical axis, both the cone angle and the pointing of conical axis is changing with the rotation angle. A possible misalignment between these two axes is shown in figure 4.1a and 4.1b. The angle between the rotation axis of the holder and the conical axis is defined as χ. For the alignment of the complete monochromator only the horizontal angular beam pointing change after rotation of the grating is relevant, since a vertical misalignment will always be compensated by the calibration of XUV energy versus grating roll angle. In figure 4.1a such an initial vertical misalignment is indicated. The situation after the grating rotation is presented in figure 4.1b. In comparison to a perfectly aligned grating the beam is displaced in the horizontal plane by a distance x. It can be shown that this translates into change of the pointing angle in the horizontal plane by:

$$\frac{\cos \chi_\phi - \cos \chi_0}{\sin \chi_\phi + \sin \chi_0} = \tan \phi \sin \gamma, \tag{4.1}$$

where ϕ is the angle between the conical axis and the rotation axis, γ is the grating rotation angle and χ_0 and χ_ϕ are the outgoing pointing angles for a perfect beam and misalignment beam after rotation. In the small angle approximation this expression simplifies to

$$\chi_\phi - \chi_0 = 2\phi\gamma. \tag{4.2}$$

As a goal for the maximal tolerable ϕ we require that we keep the overlap with a final IR focus of 100 μm after the maximum roll rotation of 20° (γ) that holder can perform. The requirement of keeping an overlap a 100 μm spot in the focal plane of the toroidal mirror (f=0.8 m) translates in requirement for the pointing stability in the horizontal plane of $\chi_\phi - \chi_0 = 125$ μrad. For the misalignment between the conical axis and grating holder axis this yields (by using equation 4.2):

$$\phi \leq 238 \; \mu rad \tag{4.3}$$

The holder provides the flexibility to adjust the grating frame with respect to the rotation stage in yaw and pitch angle. Since all the gratings surfaces in the frame are parallel the adjustment is done for all gratings at once by adjusting the complete frame. We hereby also rely on the fact that the grooves of all the gratings are parallel, since the three grating substrates are all sitting on the same base plate of the grating holder. The positions x of the linear stage for the individual gratings however has to be calibrated.

4.1.1 Yaw Angle and Linear Stage Positions

The experimental setup for the alignment of the yaw angle and the calibration of the linear stage positions x for the gratings is shown in figure 4.1b. A high quality CCD camera equipped with a zoom lens is used to take high resolution images of the front-side edge of the grating from both sides of the grating. The images are taken for different linear positions x and for each of the linear positions for a set of rotation roll angles. In figure 4.2 images are presented as examples.

With a self-written image evaluation algorithm the grating edge in the image is found and furthermore single characteristic marks (green and red) on the grating edge can be identified. For all positions x and roll angles the marked tracking points in the images rotate around a center point (yellow). This center point is the point that the rotation axis of the rotation stage points to. We apply a global fit to all data points and can find the center and directly can deduce the position x where the grating edge overlaps with the rotation axis of the holder. Hereby the precision is below $\Delta x = 5$ μm. The yaw angle of the frame is aligned by tuning the yaw angle manually until the linear stage position x for both sides of the grating are equal. This is done iteratively, first tuning the angle, then running the complete measurement and the algorithm. It is not possible to perfectly match both x values due to the mechanical precision of the manual adjustment procedure resulting an error in the yaw angle. We are therefore not limited by the measurement but by the manual precision in adjusting the yaw angle. The linear stage positions and the

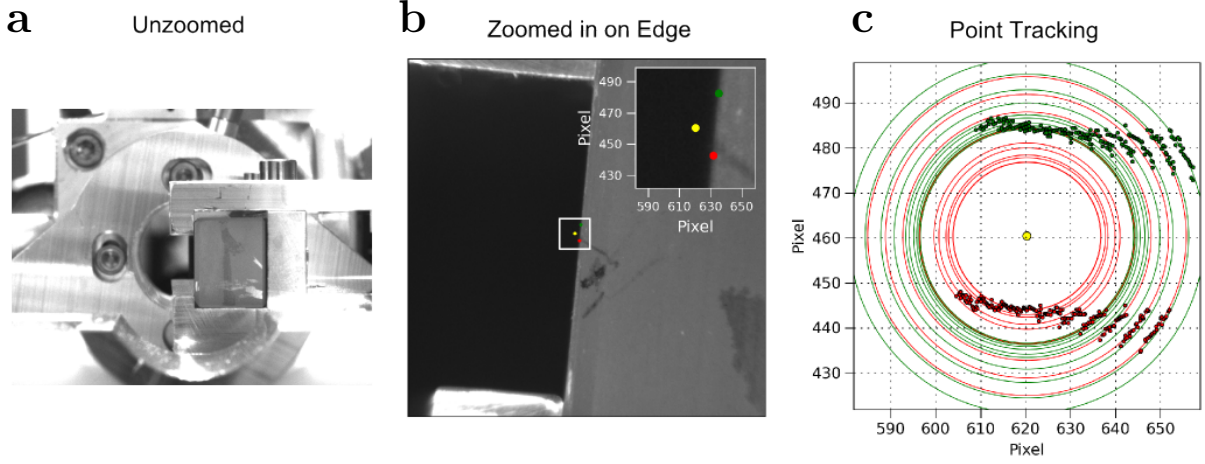**a** Unzoomed **b** Zoomed in on Edge **c** Point Tracking

Figure 4.2: a: Image of grating edge from the right side. **b:** Zoomed in image of the grating edge, with special lighting conditions the have a high contrast for the edge. The edge is fitted by a algorithm and marked as blue line. Individual points (green and red) are marked on the edge and can also be tracked in the images. **c:** Tracking of green and red point on the grating edge for different roll angles and linear positions x. A global fit fits the center rotation pixel (yellow) of the camera, that corresponds to the rotation axis of the grating holder.

pointing error are listed in the table 4.1. The error of the yaw angle is within the constraint we formulated in 4.3. However the pitch angle also needs to be aligned to assure a stable pointing after of the outgoing beams after the rotation within the formulated constraint.

	x-Gr. 1 [mm]	x-Gr. 2 [mm]	x-Gr. 3 [mm]	Δx_{edge} [μm]	Δ yaw [μrad]
Holder A	6.0685	50.986	95.975	14.6	182.5
Holder B	6.017	51.012	95.972	18	225.0

Table 4.1: Linear stage positions for the individual gratings and both grating holders.

4.1.2 Adjustment of Pitch Angle

For the alignment of the pitch angle we exploit diffraction of a 400 nm beam from the gratings. This way we make sure that we align the pitch angle of the grooves and not only the pitch angle of the glass substrate of the gratings. This precaution is taken in case the grooves are not parallel to the glass substrate. The grating holders are designed to be able to roll the gratings by more than 20°. This is sufficient to transmit a 400 nm beam with the 150 gr/mm grating when the grating is rolled to about 18°. The 400 nm beam can easily be produced by generating the 2nd harmonic of the IR laser in a BBO crystal. This opens the chance to fully check the grating holder alignment in operational mode with a beam in the visible. This will be exploited to align the pitch angle and to check the complete

alignment of the optical layout in operation mode, i.e when the gratings are rotated to transmit the first diffraction order.

If the yaw angle and the linear stage positions are aligned the only remaining degree of freedom is the pitch angle. It order to adjust the pitch angle the position of the beam in zero diffraction order after the grating holder is marked on a screen. The grating is then rotated and the pitch angle is adjusted until the beam overlaps with the mark. It should be stressed again that this strategy only works if the yaw angle is already aligned.

4.1.3 Precision of Grating Frame and Zero Order Roll Angle

The grating frame was manufactured by the institute workshop with highest precision. To test the parallelism between the grating surfaces we check the tilt between the individual grating surfaces within the frame in roll and jaw angle. We record the position of an alignment beam on a screen at a distance of about 9 m behind the grating holder with a CCD camera. The linear stage positions for the individual gratings are already calibrated and we can directly deduce the yaw tilt angle by simple geometry. For the tilt in roll angle we simply rotate the gratings until the positions from different gratings are in a horizontal plane. With the help of the camera we are able to identify the beam position on the screen with a precision below 10 μm. The results are given in the following table.

	Grating 1-2		Grating 1-3	
	Δ roll [μrad]	Δ yaw [μrad]	Δ roll [μrad]	Δ yaw [μrad]
Holder A	170	59.1	470	10.8
Holder B	1470	8.2	2007	56.7

Table 4.2: Difference in yaw and roll angle between individual grating surfaces mounted in the frame. These values give the mechanical precision of the grating frame.

The tilts in roll angle do not influence the usability of the grating holder, they only lead to a small offset in the calibration curve that connects the roll angle of the rotation stage with the reflected wavelength from the grating. The tilts are not only due to the precision of the frame, but mainly due to some play in the rotation stage. When the linear stage is moved to different x positions the applied torque to the rotation stage is changing, which is causing a small additional tilt with respect to the actual step value of the rotation stage. The error in yaw angle is below the constraint formulated in equation 4.3. A tilt of 60 μrad translates into a mechanical precision in the manufacturing of the frame of about 5 μm. This is below the guaranteed precision of the workshop that is quoted to be 10 μm.

The same measurement that is used to deduce the error in the yaw angle also yields the step motor positions that correspond to a vertical position of the grating surfaces, i.e. the roll positions for zero order diffraction. These calibration values are of great importance and listed in the following table

Zero Order Roll Angle[°]	Grating 1	Grating 2	Grating 3
Holder A	23.792	23.811	23.819
Holder B	21.080	21.164	21.195

Table 4.3: Roll angles of grating holders that correspond to vertical grating surfaces in the frame.

4.2 Alignment of Optical Layout

The alignment procedure for the optical layout is performed sequentially for each of the optical elements in the order T1, G1, T2, T3, G2, T4. As a light source a 100 μm pinhole illuminated from the back by a He-Ne laser is used. The pinhole is positioned at the spot where the HHG focus will be. This fixes the position of the source. The pointing of the beam is fixed by the iris 1. The position of the pinhole and the first iris is sufficient to completely define the beam pointing of the source. Additionally the iris at the end of path e in figure 3.13 is set to record the beam pointing. This iris is used to align a laser beam into the monochromator when the pinhole is removed after the initial alignment is completed.

For the alignment of the individual optical elements a beam profile camera is used to monitor the beam after the element. The doors of all chambers are removed such that we can track the shape of the mode after each element over a distance of a few meters. The toroidal mirrors are either collimating the beam, for T1 or T3, or focusing the beam, for T2 and T4.

In both cases the projection of the mode of the beam onto the toroidal mirror is slightly bigger than the length of the mirrors. A small diffraction pattern from the side edges of the mirrors can be observed, making it easy to center the beams in the middle of the mirrors. The roll angle defines the height of the beam and is set such that beam is travelling parallel to the optical table. In the case of T1 and T3 the distance to the HHG focus and the slit focus has to be set correctly in order to collimate the beam. This is achieved by tracking the mode size over a few meters behind the mirror and ensuring that the mode size does not change. The remaining angles are the yaw and pitch angle. For mirrors T1 and T3 we examine the mode a few meters after the mirror. For mirrors T2 and T4 we check the focus after the mirrors. In both cases a wrong yaw angle leads to astigmatism, i.e. the mode is elongated, either horizontally or vertically depending on the distance of the camera after the element. A wrong pitch angle leads to a tilting(twisting) of the mode. Both angles are adjusted until the aberrations are minimized. The grating holders are set up in zero order. The incidence angles and distances to the mirrors are set by fixing the distance with the help of a ruler.

After the alignment we are able to image the 100 μm pinhole onto a 135 μm round spot in the slit focus. If we assume that the HHG focus has a Gaussian shape and the broadened spot size in the slit focus is a convolution of the HHG focus with also Gaussian shaped aberrations we estimate the aberrations to be $w_{aberrations.} = 90$ μm (FWHM). It is unclear if the aberration are originating from a miss-alignment of the optical elements
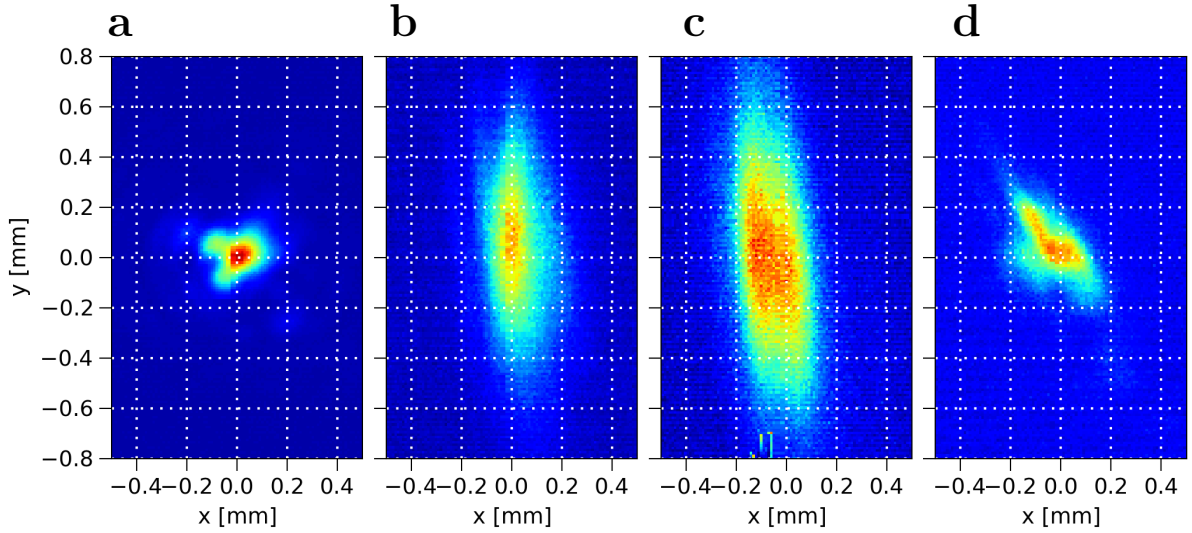
Figure 4.3: a: Mode of a 400 nm beam at the final focus of the XUV monochromator recorded with a beam profile camera. Both gratings are operated in zero order. **b**: In comparison to the left image, the grating in stage one of the monochromator is rotated into first diffraction order, the roll angle is about 18°. One can observe the diffraction due to the bandwidth of the 400 nm pulse. **c**: First grating in zero order and the grating in the second stage is rotated into first diffraction order. **d**: Both gratings rotated into first diffraction order. The beams are collimated again after the second stage grating and are focused into the same spot. This indicates that the compensation by the second stage of the pulse front tilt is working. The center of the final focus is shifted in the horizontal plane by less than 20 μm to the left. Within this precision the beams are rotating on a cone.

in the monochromator or are an intrinsic limit of the toroidal mirrors. The aberrations have consequences for the energy resolution of the monochromator as it is discussed in the theory chapter 3.2 and the performance chapter 5.

After the alignment with the pinhole the complete alignment is checked with the 2nd harmonic of the actual laser beam we will use. The beam profile camera is placed in the final focus. When an experimental endstation is connected to the beamline the mirror 20 can be moved in the beam and the final focus can be monitored at the end of path h. In figure 4.3 the result is presented.

In the image A, both gratings are in zero order. The images B and C correspond to the case where one holder is in zero order the other in first diffraction order. The image D corresponds to the setting where both gratings are turned into first diffraction order.

For both images with only one grating rotated into first diffraction order we can observe an elongated mode in the vertical direction, originating from the conical diffraction of the 20 nm bandwidth of the at 400 nm center wavelength. The vertical position of the mode can always be adjusted by rotating the gratings. The vertical displacement of the modes for images B and C is less than 50 μm, translating into a pointing stability after rotation of the gratings of about 60 μrad. When both stages are operated in first diffraction order

the compensation of the angular dispersion induced by the first grating can be observed. After the second grating the different rays corresponding to the different energies within the bandwidth of the pulse are parallel again and then focused by the last toroidal mirror onto the same focal spot. The mode is rather round and the center is shifted in the horizontal plane by less than 20 μm to the left.

To recall, the gratings are rotated more than 18° for a 400 nm beam to overlap the first diffraction order with the pointing of the zero order. This demonstrates that the pre-alignment of the grating holder was successful. The pump-probe overlap with a IR beam bigger than 20 μm is not lost. In practice the pointing stability will even be higher, since the rotations angles between XUV energies are always smaller than the 18°. We can conclude that both the pre-alignment of the grating holders and the alignment of the complete setup was successful.

4.3 Daily Alignment

After the initial alignment of the complete layout two challenges remain. How to reproduce the alignment on a daily basis and how to maintain the alignment when evacuating the vacuum system. The obstacle here is that any beam entering the chamber through a window, will change its pointing for vented or evacuated chambers, due to the bending of the window under the different pressure conditions.

It is necessary to have alignment points within the vacuum system. The alignment points within the monochromator have to be chosen carefully and can be counter-intuitive. The monochromator is an optical imaging system with different focal planes. It is therefore fundamentally different to the usual alignment of a collimated beam, where one can think of the beam as a straight line that is fixed by two points in space. In an imaging system different beams can go through the same focus.

In figure 4.4 a ray-tracing simulation of the monochromator is presented. The toroidal mirrors are replaced by lenses and the gratings are neglected. For the alignment the gratings are the holders are operated in zero order. As a first alignment point we chose again the iris in front of the first toroidal, see iris 1 in figure 3.13. This will fix the beam in space. In figure 4.4 this is illustrated as a point source 5 cm before the first toroidal mirror.

The second iris in the monochromator fixes the angle of the beam in space. It should be emphasized that the figure 4.4 does not show the divergence and focusing of a single divergent beam, but rather the guiding of a set of rays traveling with different angles through the first iris. Placing the second iris in the "focus" of these rays would make this alignment point completely useless for fixing the angle of beam. The maximum deviation of the beams is in front of the third toroidal. The second alignment point is therefore iris 14 in figure 3.13. In figure 4.5 images of the iris recorded with cameras through viewports a and c are presented. The circular diffraction pattern results from the iris in the XUV arm of the optical layout outside the vacuum system. It helps to center the beam on the iris.

It should be stressed again that the alignment via the two irises inside the monochromator
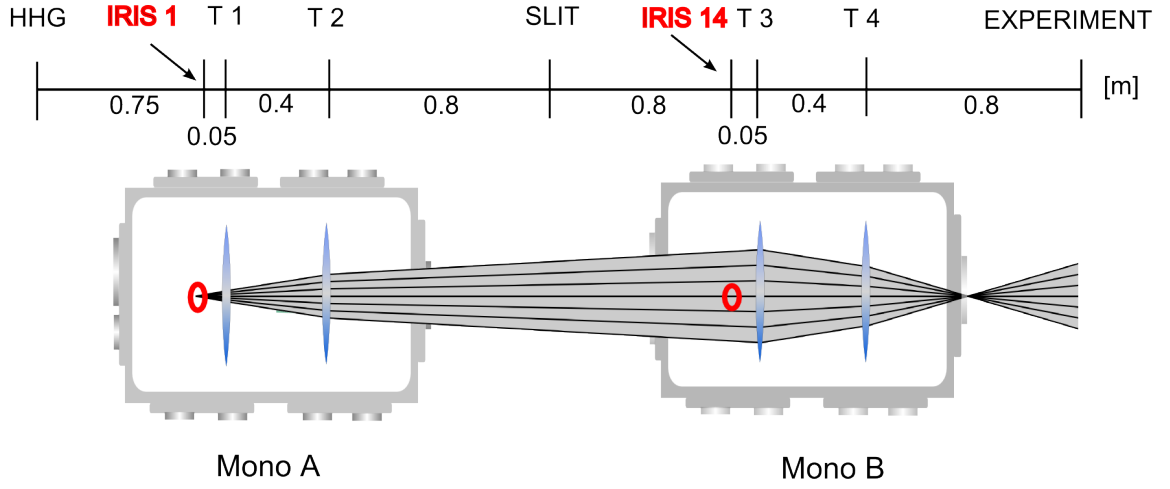
Figure 4.4: Position of irises for daily alignment inside the vacuum chambers. The first iris (1) is fixed in front of toroidal mirror 1. This fixes the beam in space. The second alignment iris (14) has to fix the pointing of the beam. A ray-tracing simulation shows different beams going through the monochomator. Mirrors are replaced by lenses and gratings are neglected. The maximum deviation of beams is in front of toroidal mirror 3, where also the second iris (14) is placed.
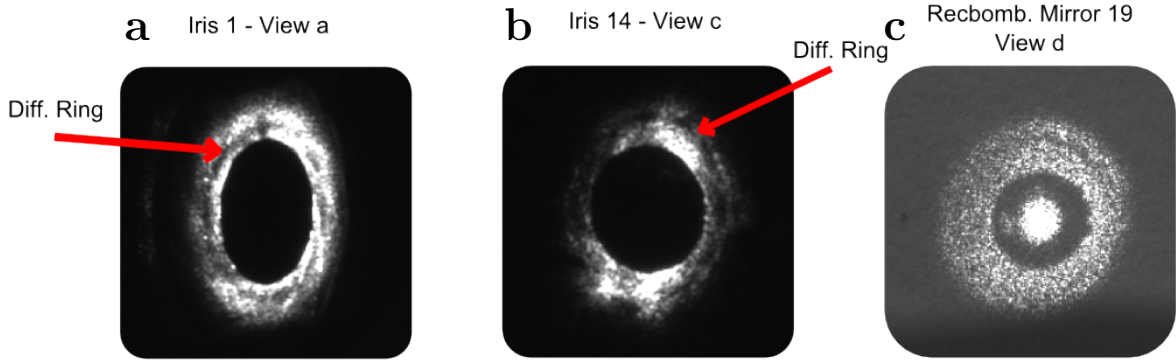
Figure 4.5: **a:** View a of iris 1. The circular diffraction from the iris outside the vacuum before the periscope in the XUV arm of the pump-probe setup can clearly be seen. **b:** View c of iris 14. The circular diffraction ring is indicated. **c:** View d of recombination mirror. IR arm is the outside ring. The IR beam going through the monochromator operated in zero order, with the aluminium foil removed is the beam in the middle.

layout requires that alignment of the individual optical elements does not change. This is of special importance for the grating holders. When a beam is aligned into the monochromator the gratings have to be always rotated into the zero order position given by the step motor values in the table 4.3, in order to reproduce the same alignment. The alignment points inside vacuum only serve as a method to transfer the alignment from vented to evacuated vacuum system. In practice they are also conveniently used for the daily alignment of the IR beam into the setup. If however a misalignment of an optical element inside the monochromator occurred one has to go back to the alignment iris at the end of path e, instead of iris 14. However this only works for vented chambers.

The slit would also serve as a possible alignment point according to the ray-tracing simulation. However the slit position only fixes the beam in the horizontal plane. Additionally the beam is focused in the slit plane and alignment can only done by optimizing the throughput trough the slit by measuring the power with the XUV diode. This alignment procedure relies on the shape of the optical XUV mode which can change with different laser settings and therefore is not recommended for alignment of the beam. However the XUV intensity measured by the XUV diode can be used to align the slit to the already aligned beam.

Once the slit position is fixed, the first grating is turned and the throughput through the slit is monitored with the XUV diode. It is easy to distinguish the individual harmonics. However the stepmotor positions for the individual harmonics have to be recalibrated after the alignment of the IR beam into the monochromator was renewed. This will be also discussed in the next chapter referring to the performance of the monochromator, in the section about the energy resolution 5.2.

4.4 Summary

The potential to align three gratings at once in combination with the freedom to check the alignment with a visible beam turns out to be a great advantage that eases many alignment issues. The pre-alignment of the grating holder is time-consuming and is a demanding stand alone mechanical problem due to the two-dimensional nature of the conical diffraction geometry. However a stable pointing of the outgoing beam from the grating holders for all XUV energies simplifies all following alignment and makes it possible to exploit the full capabilities of the experimental setup.

5 Performance of the TDCM

This chapter presents the actual a achieved performance characteristics of the beamline. The topics covered are the energy resolution, time resolution, transmission efficiency and the calibration of the IR intensity in the final focus. The results on transmission efficiency and IR intensity calibration are already covered in [41] and only the main results are briefly repeated here.

For the determination of the energy resolution and time resolution, photoelectron spectroscopy in combination with IR induced sideband generation is performed. For a the energy resolution a systematic study is conducted covering the complete spectral transmission range of the beamline from 10 eV to 50 eV. The achieved time resolution is demonstrated for a single XUV center energy.

At the end of the chapter a summary of the present status of the the beamline is given, which also includes general remarks on usability and stability. This is completed by an outlook section that summarizes a few possibilities for further technical developments of the beamline.

5.1 Transmission Efficiency

The overall transmission through the complete optical layout is measured with calibrated XUV diodes. We record the XUV intensity before toroidal mirror 3 and after toroidal mirror 4, see figure 3.13. We directly can deduce the transmission of a single stage of the monochromator. The complete transmission is the square of the transmission of a single stage. The transmission is measured for XUV energies that correspond to the maxima of an HHG frequency comb. An XUV spectrum generated in the HHG source and recorded with the XUV spectrometer is presented in figure 5.1a. The corresponding transmission efficiencies for two of the three gratings is presented in the the figure 5.1b.

The energy calibration of the XUV diodes and a detailed description of the measurement procedure can be found in [41]. For the energy range from 25 eV to 50 eV we have an overall transmission above 6 %. It becomes evident that gratings with different blaze angles are needed to cover the complete energy range with sufficient transmission efficiency. The 150 gr/mm grating is not studied systematically for the following reason. In order to operate the XUV diode, the Aluminum filter has to be inserted in the XUV beam to filter out the IR contribution in the XUV arm in order to avoid any stray light of the IR in the chambers, which is also detected by the XUV diode (When the Aluminum foil is not inserted, the IR contribution in the XUV arm is separated from the XUV after the first grating and is hitting the wall of the chamber.) At the same time the transmission efficiency of the filter
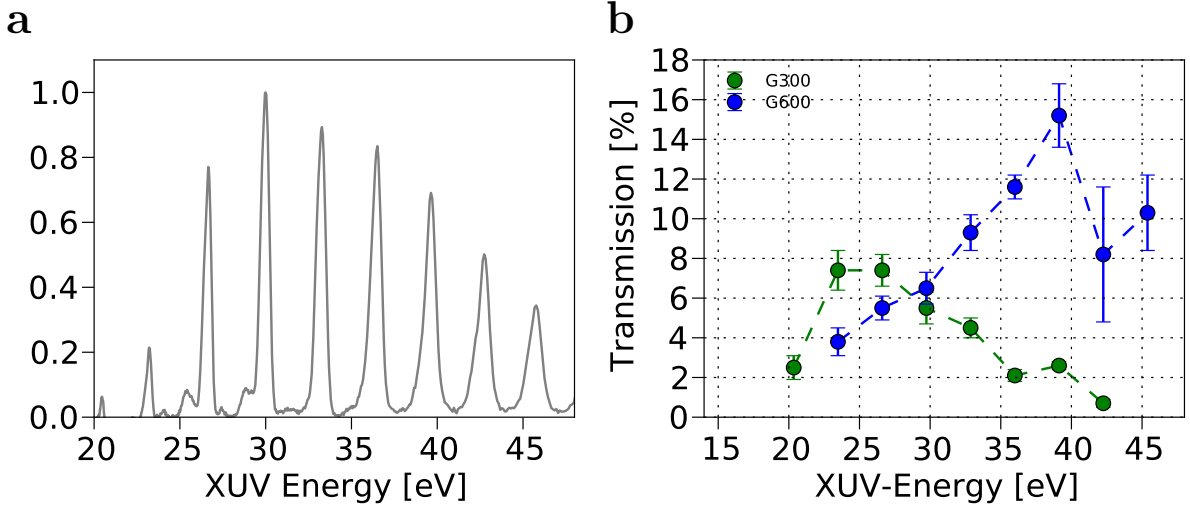
a

b

Figure 5.1: a: HHG spectrum recorded with the XUV spectrometer. The generation gas is Argon and the IR pulse duration is 25 fs (FWHM). **b:** Overall transmission efficiency through the complete monochromater measured with calibrated XUV photodiodes.

drops dramatically for XUV energies below 20 eV, which is covering part of the energy range the 150 gr/mm grating is optimal for and therefore a systematic study of the low energy region is not possible. As a reminder we want to point out that it is however possible to operate the final XUV-IR pump-probe experiments without inserting the Aluminum foil, since the amount of IR stray light entering the experimental chamber is negligible.

After the calibration of the overall transmission one of the diodes is permanently placed after toroidal mirror 3. At this position it is used to monitor the absolute XUV power during measurement runs and is used to monitor the XUV power during the daily optimization of the HHG-source. The relation between the power measured at the permanent position of the diode and the pulse energy in the final focus is not calibrated but can be estimated in the following way. If we assume that the overall transmission is always above 6 % and the grating and toroidal mirrors have the same reflection efficiency we get a reflection efficiency for a single optical element of about 62 %. The pulse energy in the final focus is then about 38 % of the measured pulse energy after the toroidal mirror 3. The XUV pulse energy at the permanent diode position is recorded on a daily basis. We observe that we achieve a XUV pulse energy in the final focus varying in the range of 10^6 to 10^7 photons per pulse, depending on the daily conditions of the laser and the selected XUV photon energy.

5.2 Energy Resolution and Bandwidth

In this section we present experimental data on the scaling of energy bandwidth of the XUV pulse with the slit width (first subsection) and the XUV energy (second subsection). In both parts the agreement of the experimentally obtained data with the theoretical model

presented in section 3.2.4 is discussed.

5.2.1 Dependence on Slit Width

The spectral width of a pulse passing through a single slit is given by the product of the transmission profile of the monochromator and the intensity profile of the XUV spectrum that is filtered:

$$I_{Tr}(E) = T_{Mon}(E) \cdot I_{In}(E) \tag{5.1}$$

where T_{Mon} is the transmission profile of the slit in energy space I_{In} is the spectrum of the XUV pulse before the slit. In our case, where the XUV spectrum is strongly modulated, the actual transmitted bandwidth depends strongly on both contributions in the equation. For the transmission profile we assume a rectangular function with a given width that is deduced from the slit width. The rectangular transmission profile is convoluted with a Gaussian profile, to account for the energy resolution of the monochromator that was introduced in chapter 3.2.4. The transmission profile then reads:

$$T_{Mon}(E, E_C, w, \sigma) = \frac{1}{2}(ed(E, (E_C - w_{Sl}/2), \sigma) \tag{5.2}$$

$$+ ed(-E, (E_C + w_{Sl}/2), \sigma)) \tag{5.3}$$

where the function for the edge is

$$ed(x, x_0, \sigma) = erf\left(\frac{1}{\sqrt{2}}\frac{x - x_0}{\sigma}\right) \tag{5.4}$$

and E_C the center energy, w the energy width of the transmission profile deduced from the the slit width and σ is the width of the Gaussian profile that is convoluted with the rectangular function. We refer to σ directly as the energy resolution from now on. In figure 5.2 the characteristics of the transmission profile are illustrated. In a the transmission profile is plotted for various ratios between the width w and the resolution σ. The resolution is set to one and is fixed for all plotted curves. For comparison a Gaussian profile with $\sigma = 1$ is plotted in dotted lines and normalized to the maximum of the transmission profile. We can see that for ratios smaller than eight we observe a reduction in amplitude of the center energy. In b the reduction of the center energy is plotted against the ratio between w/σ. For ratios smaller than one the transmission profile can safely be approximated by a Gaussian profile.

We experimentally investigate the spectral shape of the transmitted XUV pulse through the slit and the dependence of the spectral shape on the slit width by performing photo-electron spectroscopy of Argon using the VMIS endstation. Presented in figure 5.3a we do so, as an example, for a range of XUV energies covering the width of single harmonic (H19,
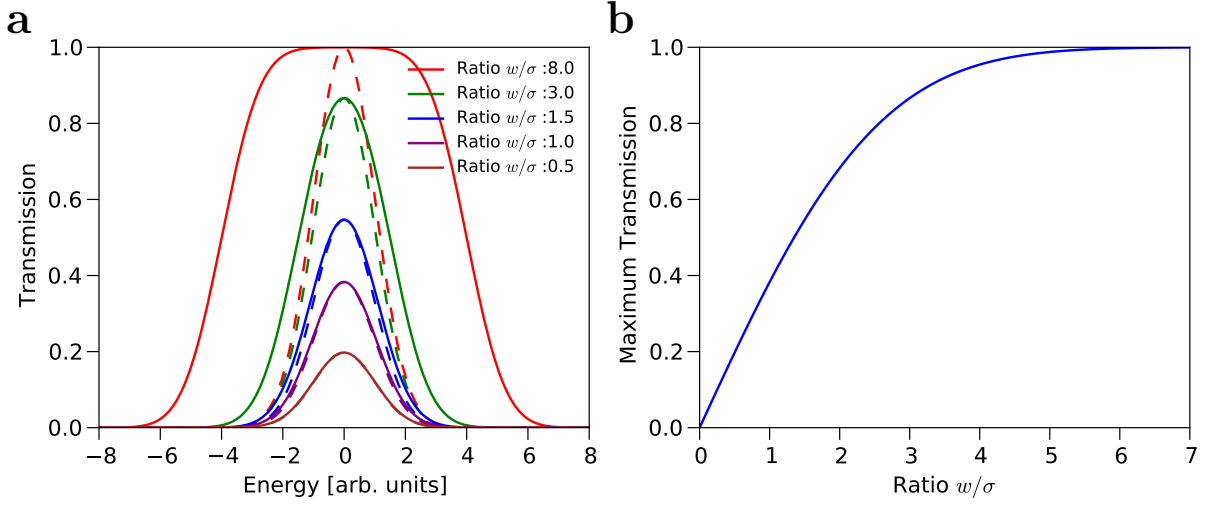
Figure 5.2: a: The transmission profile from equation 5.2 is plotted for a fixed energy resolution $\sigma = 1$ and varying spectral width of the transmission profile with w. For all ratios a Gaussian function with the width of 1 and the amplitude normalized to the transmission profile is plotted for comparison with the actual transmission profile. For ratios below 1 the transmission profile can be approximated by a Gaussian function. **b:** When the energy resolution becomes comparable to the width of the transmission profile, the maximum of the transmission profile becomes smaller than one. Here the reduction in transmission with respect to the ratio between w/σ is plotted.

29.8 eV), using a slit with a width of 106 μm and using the the grating with 300 gr/mm. The x-axis is the expected calculated XUV energy deduced for the grating equation 3.7. The y-axis gives the measured kinetic energy of the photoelectrons. We observe ionization ending in the 3p ionic state of Argon with an IP of 15.76 eV. The final ionic ground state ($^2P^o$) is split into two close lying states due to spin-orbit coupling. The states are separated by 0.18 eV [45]. The measured spectral width of the spectrum therefore does not directly reflect the spectral width of the XUV pulse, however for this measurement the difference is small and neglected in the discussion. From the scaling of the measured kinetic energy with the calculated XUV energy we can estimate that the incidence angle of the XUV beam on the first grating is 4.78°. For further analysis we first analyze the measured spectra for a single XUV energy in more detail:

In the figure 5.3b photoelectron spectra corresponding to the calculated XUV energy of 29.8 eV are presented. Here we show the spectra for four slit widths that are, no-slit, 48 μm, 106 μm, and 206 μm. The spectra are normalized to the maximum of the H19 peak in the no-slit spectrum. The reduction in transmission with smaller slit widths can be observed. In order to compare the reduction with the expected reduction presented in figure 5.2b we need theoretical values for w and σ. The theoretical estimation of the energy resolution of the monochromator was presented in section3.2.4. The result for the the given XUV energy of 29.8 eV and the calculated spectral widths of the slits are summarized in the table 5.1.
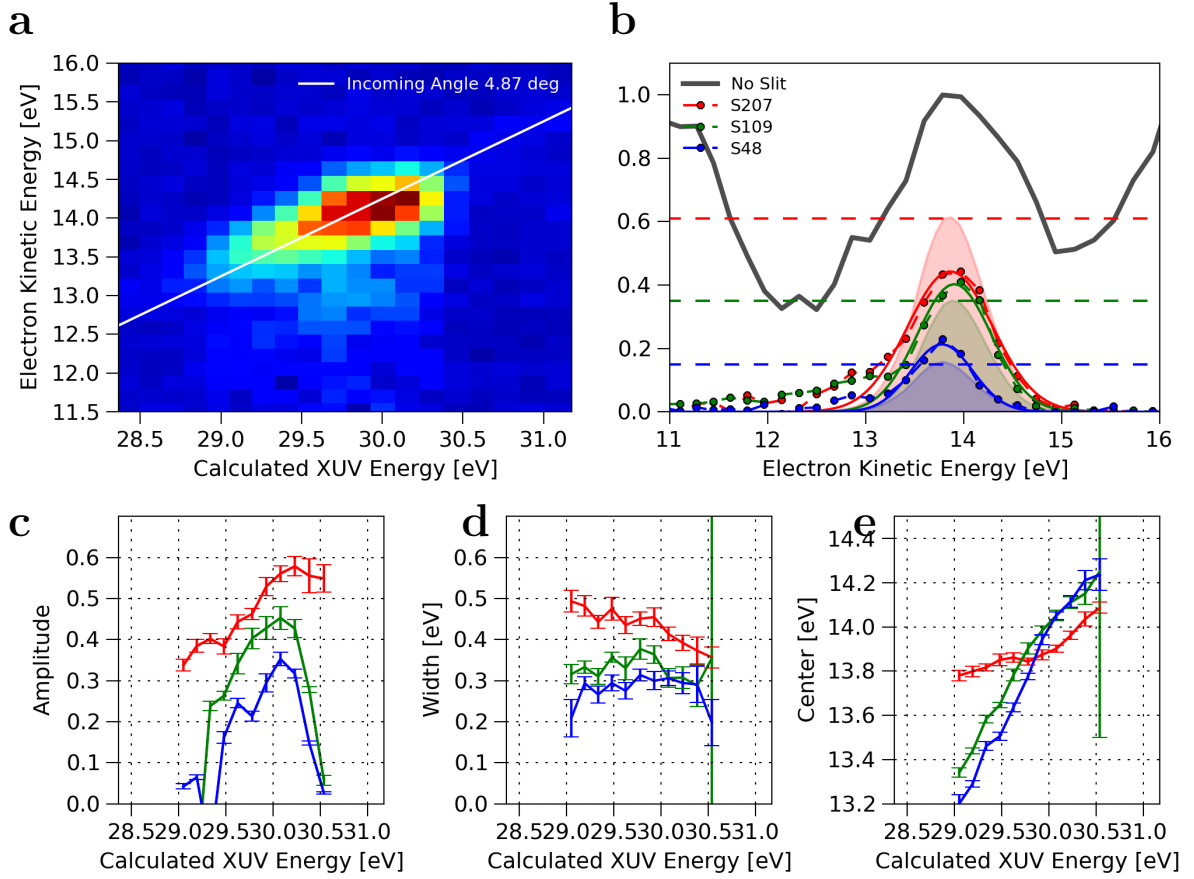
Figure 5.3: a: Photoelectron spectra obtained in Argon for H19, grating 300 gr/mm and a fixed slit width of 106 μm. The monochromator gratings are scanned over the complete energy profile of the harmonic peak. The expected XUV energies are calculated via the grating equation 3.7 and are in agreement with the measured spectra for an incidence angle of 4.87° of the XUV beam on the first grating. **b:** Spectra for no-slit and three slit widths of 48 μm, 106 μm, and 206 μm. The energy resolution σ is taken from section 3.2.4 and is equal to 0.35 eV. The different slit widths correspond to a spectral width w of the transmission profile of 0.14 eV, 0.32 eV and 0.61 eV. The dotted lines indicate the transmission amplitude reduction with respect to the maximum of the no-slit spectrum. The shaded areas indicate the product of the no-slit spectrum multiplied by the transmission profile given by energy resolution and slit width. Gaussian profiles are fitted to the spectra. **c, d and e:** Result of Gaussian profile fit to the scan. Discussion is in the text.

	S1	S2	S3
Width [μm]	48	109	207
w [eV]	0.14	0.32	0.61
σ [eV]	0.35	0.35	0.35

Table 5.1: Energy resolution σ and width w of the transmission profile calculated from the slit width and the groove density of 300 gr/mm. The XUV center energy is 29.8 eV (H19)

The reduction in transmission amplitude reduction deduced from the values in the table 5.1 and plot 5.2 and is indicated as dotted horizontal lines in figure 5.3b. The shaded areas are the product of the no-slit spectrum with the transmission profile T_{mon} defined by the values in the table 5.1. For the slits with 498 μm and 109 μm the results of the theoretical estimation are in good agreement with the experimental data. The data for the slit width with 206 μm has a too low amplitude. A possible reason might be a change in the XUV intensity between the different measurements for different slits.

To gain even more information, a Gaussian profiles are fitted to the line shapes, marked as solid lines in the figure. The assumption of using a Gaussian profile is feasible since the ratio of w to σ is below 2, according to the theoretical expected values given in table 5.1, see also figure 5.2a. For lower kinetic energies lower than 13.2 eV the Gaussian fit does not reproduce the long tails of the measured spectra. We attribute the tails to an artefact in the VMI focusing conditions and assume the induced error in the fit is negligible. In the plots in figure 5.3 c, d, and e the fit parameters for the scan of the harmonic peak are presented. The amplitude is slightly asymmetric with respect to the energy, which might be due to the shape of the XUV spectrum, but can not fully be explained by it. The fitted width stays rather constant over the complete scan range. We deduce that the influence of the shape of the XUV spectrum on the transmitted spectral width for these small slit widths can be neglected. After all the expected spectral width for the slits with 48 μm and 109 μm are anyway close to the energy resolution with 0.35 eV. For the slits 48 μm and 109 μm we see a similar slope for the center energy, but the lines are slightly offset. The slope just resembles the slope of the white line in figure 5.3a, corresponding to an incidence angle of 4.78° of the XUV beam on the first grating. The reason for the offset between the slits is a slightly different position in height of the slits when setting up the slits in the slit chamber, resulting in a different transmitted XUV energy for the same step-motor settings of the grating holder. Again the curve for the 207 μm slit exhibits a different behaviour that is not explained so far.

In summary we can claim that the measured transmitted bandwidth of the pulses for different slit widths scales as expected from our theoretical modeling. The energy resolution of the monochromator is sufficient to resolve the individual harmonics in the XUV spectrum and special care has to be taken to exactly calibrate the transmitted XUV center energy. However for most experiments it is sufficient to know the exact XUV energy within the range of a single harmonic and it is additionally possible to calibrate the XUV energy
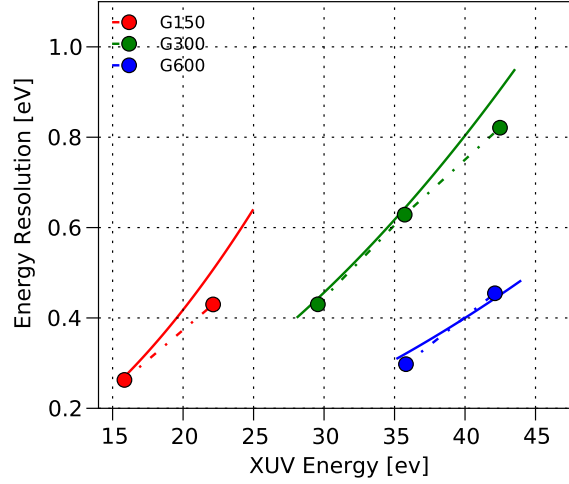
Figure 5.4: Bandwidth σ of transmitted pulses through a 106 μm slit for all three gratings. The datapoints below 25 eV are obtained from photoelectron spectra of Xenon, while for the data point with higher XUV energies Helium is used. The simulation assumes a 50 μm HHG source width and aberrations of 90 μm. The resolving power of the gratings is taken into account, and the resolution of the VMI is assumed to be 2 % of the kinetic energy of the measured electrons.

from the spectroscopic data. We further conclude that a slit width under 100 μm does not improve the energy resolution and is only reducing the XUV pulse energy. If the energy resolution of the final experiment is not the most crucial requirement it is beneficial to take a bigger slit. However in the simulation in chapter 3.2.4 it was derived that slit widths larger than about 600 μm starts to spoil the time resolution again.

5.2.2 Energy Scaling of Bandwidth

In the previous section the scaling of the transmitted bandwidth of the XUV pulse for different slit sizes is presented. In this section the slit width is fixed to 106 μm but the center XUV energy is varied, covering almost the complete energy range between 10 eV to 50 eV and using all three gratings with different groove densities. In the previous section it was demonstrated that the influence of the XUV spectrum on the transmitted bandwidth can be neglected for slit with width of 106 μm. For the lower XUV energies, up to 25 eV, photoelectron spectroscopy on Xenon is performed (IP=12.13 eV). The splitting of the final ionic state $^2P^o$ of 1.3 eV, that is due to different spin-orbit coupling [45], can be resolved and a fit of a sum of two Gaussian profiles to the data is performed. For XUV energies above 25 eV Helium is used as a target gas with an ionization potential of 24.49 eV and a final ionic state ^2S with no orbital angular momentum. Here a single Gaussian profile is fitted to the spectra. The results for σ and all energies are presented in figure 5.4

According to their duty the gratings cover different energetic regions, where the bandwidth transmitted through the slit is small. From the scaling with the slit width we

concluded that below a slit width of 100 μm the bandwidth can not be reduced further by closing the slit, we are operating close to the limits of the energy resolution of the monochromator. We compare the result with the simulated energy resolution from section 3.2.4. (We also include the finite slit width of 109 μm into the simulation). Additionally the VMI resolution is included by adding 2% of the kinetic energy of the measured spectra. The simulation is in excellent agreement with the measured spectra. Since the input parameters for the simulation are obtained from independent sources we can conclude that the monochromator energy resolution scales according to the expectations.

5.3 Time Resolution

We employ sideband generation in Argon to study the temporal resolution of the XUV/IR pump-probe setup. During the temporal overlap between the IR pulse and the XUV pulse, the electric field of the IR pulse can accelerate or decelerate the electron that is emitted from the atom after the ionization by the XUV pulse. The final accumulated energy depends on the time of emission of the electron during the optical cycle of the IR field. For a multi-cycle IR pulse, the interference in the accumulated phase between electrons with same kinetic energy but emitted during different optical cycles leads to a discrete energetic structure in the photoelectron kinetic energy distribution. Essentially the interference in time leads to sidebands in energy to the unperturbed kinetic energy of the electron. The energy spacing of the sidebands are exactly multiples of the IR photon energy resulting in electrons with kinetic energies of:

$$E_{kin}^n = E_{kin}^0 + n \cdot E_{IR} \tag{5.5}$$

where E_{kin}^0 is the kinetic energy of the electrons without any disturbance of the IR field, E_{IR} the IR photon energy and n is the sideband order. The probability of creating an electron with a kinetic energy E^n at a fixed time delay between the XUV and IR pulse is given by

$$p(E^n(\tau)) \propto \int_{-\infty}^{\infty} I_{XUV}(t) \cdot (I_{IR}(t - \tau))^n \, dt \tag{5.6}$$

where $I(t)$ denotes the Intensity of the pulse at a given time. The assumption that the creation of the n-th sideband is proportional the intensity of the I_{IR}^n only holds for sufficiently small intensities. For large IR intensities ($> 5 \ TW/cm^2$ [46]) also interference within an optical cycle lead to additional modulation of the sideband creation probability [47]. However these are not observable for intensities presented in this section.

If both the IR and the XUV pulse have a Gaussian shape in time, also the transient profile, i. e. the cross-correlation, in equation 5.6 has a Gaussian profile with the following FWHM width of [48, 49]:
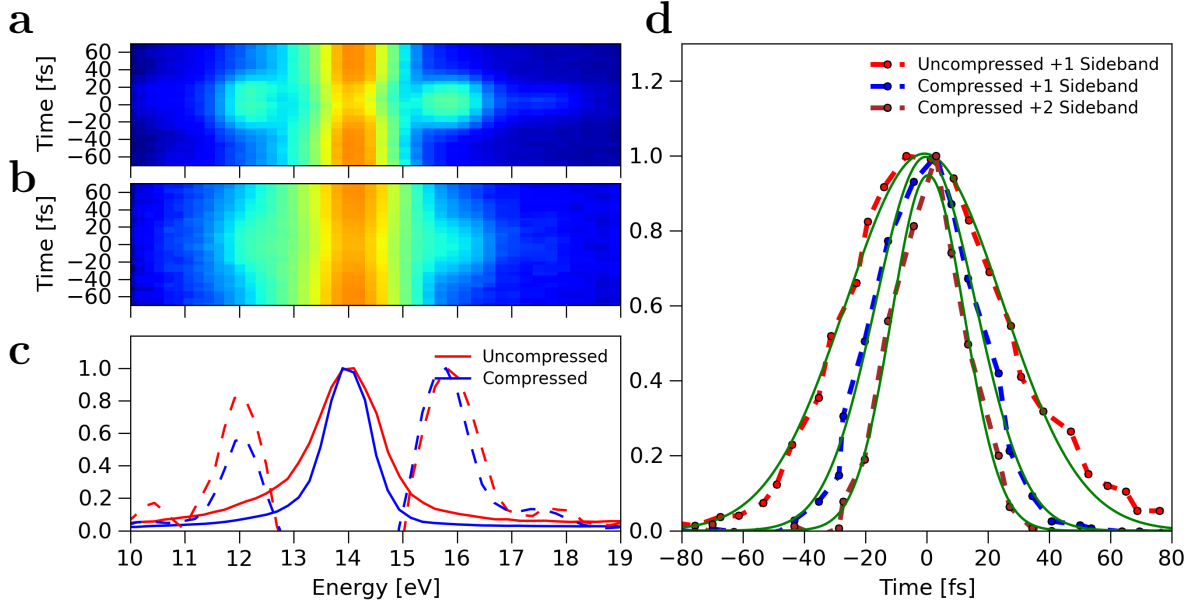
a

b

c

d

Figure 5.5: a,b: Time-resolved photoelectron spectra of sideband generation in Argon with an XUV energy of 29.8 eV (H19). **a** shows the map for the monochromator in normal operation mode, **b** for the second stage of the monochromator operated in zero order, essentially turning off the recompression. **c:** Spectra at time-zero. For both cases two positive sidebands are visible. **d:** Transients of first two positive sidebands for the compressed case and of the first positive sideband for the uncompressed case.

$$\Delta t_X^n = \sqrt{\Delta t_{XUV}^2 + \frac{\Delta t_{IR}^2}{n}} \tag{5.7}$$

In figure 5.5 time-resolved photoelectron spectra of Argon (IP=15.57 eV) ionized with an XUV energy of 29.8 eV (H19) are presented. The grating with 300 gr/mm is used and the slit width is 106 μm. Two time delay scans are shown. One for the monochromator in normal operation mode and the other for the second grating operated in zero order, essentially turning off the time delay compensation by the second stage.

We observe two positive sidebands for the normal case and fit a Gaussian profile to transients yielding for the FWHM:

$$\Delta t_X^{+1} = 38.8 \ \pm \ 0.4 \ fs \qquad \Delta t_X^{+2} = 28.8 \ \pm \ 0.6 \ fs \tag{5.8}$$

From the ratio of the pulse duration of the two sidebands and equation 5.7 the individual pulse duration of the XUV and IR pulse can be deduced:

$$\Delta t_{XUV} = 12 \ \pm \ 3 \ fs \qquad \Delta t_{IR} = 37 \ \pm \ 1 \ fs \tag{5.9}$$

The IR pulse duration at the laser output is in the range of 21 fs to 23 fs and therefore the observed pulse duration for the XUV pulse with about 12 fs is in good agreement with the expectation being about one half of the IR pulse duration. Additionally the results are in agreement with pulse XUV durations observed in the TDCM in Milano [28], where an XUV pulse with a duration of about 13 fs is observed for a comparable IR pulse used to generate the XUV pulse.

The mismatch between the IR pulse duration in the final focus with 37 fs and the IR pulse duration coming from the laser can have various reasons. Most likely the dispersion control via the glass plates in the IR arm is not optimal, but also the final focus geometry or the narrowing of the bandwidth of the pulse by optical elements could result in an effective longer pulse duration.

In order to test the performance of the second stage of the monochromator the second grating is turned into zero diffraction order. The grating only reflects the XUV pulse coming from the first stage and the pulse is not recompressed. The data again is presented in figure 5.5 and a fit to the cross correlation with the IR pulse yields for the first sideband:

$$\Delta t_X^{+1} = 60 \ \pm \ 1 \ fs \tag{5.10}$$

For a pulse duration of the IR with 37 fs this results in an XUV pulse duration of the stretched pulse of

$$\Delta t_{XUV,str.} = 47 \ \pm \ 1 \ fs \tag{5.11}$$

In order to verify if the expected stretching is in agreement with the theoretical stretching, we assume that in case of the second stage operated in diffraction mode, the pulse was perfectly recompressed. We then have a stretching from 12 fs to 47 fs. We additionally assume that the mode of the XUV beam on the first grating also has a spatial Gaussian profile. The stretched pulse duration after the first grating is the convolution between the Gaussian pulse shape in time of the incoming pulse and the induced stretch of the spatial Gaussian shape which results in

$$\Delta t_{XUV,str.} = \sqrt{\Delta t_{XUV,HHG}^2 + \left(w_m \sigma_{gr} \frac{\lambda}{c} \right)^2} \tag{5.12}$$

where w_m is the FWHM size of the mode on the first grating and σ_{gr} is the groove density of the grating. This results in

$$w_m = 1.10 \ mm \tag{5.13}$$

This is in reasonable agreement with our expectations, since we roughly observe an IR mode of about 5 mm on the first toroidal mirror and the XUV divergence of the HHG source is about 0.2 of the IR divergence [37].

During the various experiments carried out in the course of the thesis the time resolution was varying in a range less than 10 fs, which was mostly due to the daily laser performance. One can generally observe a shorter XUV pulse duration when going to higher XUV energies, which is expected for the HHG process. However these effects only have a minor influence on the time resolution. To make statements about the limits of the performance in terms of the time resolution and to asses the quality of the alignment of the monochromator, the initial IR pulse duration and the dispersion control of the IR arm has to be improved. This will be discussed in more detail in the outlook section.

5.4 IR - Focus and Intensity

Sideband generation can be exploited to calibrate the IR intensity in the final focus. The maximal number of sidebands that are observable can be deduced from the accumulated momentum of the electron during the IR cycle after it is removed from the atom by an XUV photon. The energetic region where sidebands can be observed is given by [49, 50]

$$E_{c\pm} = 0.5 * (\sqrt{2E_0} \pm \sqrt{4U_p})^2 = E_0 \pm \sqrt{8E_0U_P} + 2U_p \tag{5.14}$$

where E_0 is the energy of the unperturbed electron and U_p is the pondermotive potential given by

$$U_p = \frac{e^2 I_L}{2\epsilon_0 c m_e \omega^2} = 9.338 \cdot 10^{-8} \cdot \lambda^2 [nm^2] \cdot I_L [TW/cm^2] \tag{5.15}$$

where I_L is the intensity of the IR field averaged over the optical cycle. In figure 5.6 a photoelectron spectrum for ionization of Argon with an XUV energy of 40.75 eV is presented, i.e. the two dimensional momentum distribution and the angular integrated energy spectrum. The IR photon energy is 1.63 eV.

The intensity of the electron kinetic energy spectrum is plotted on a logarithmic scale and up to seven positive sidebands are visible. Since the probability of creating an electron in the n-th sideband is proportional to I_{IR}^n a linear decay in intensity with the sideband order can be observed. In fact two regions with different linear decay of intensity can be seen and the kinetic energy where the slope is changing is commonly identified as E_c, the cut-off energy. For a center energy of 25.1 eV and a cut-off of 32.5 eV, this translates into an IR intensity in the focus of

$$I_L = 4.11 \ TW/cm^2 \tag{5.16}$$

The IR pulse energy after the output window of the VMI is 132 mJ. If we assume an IR pulse duration of 37 fs (FWHM), in agreement with the result from the section on time resolution, we get for a Gaussian shaped pulse in time and space a focal spot size of
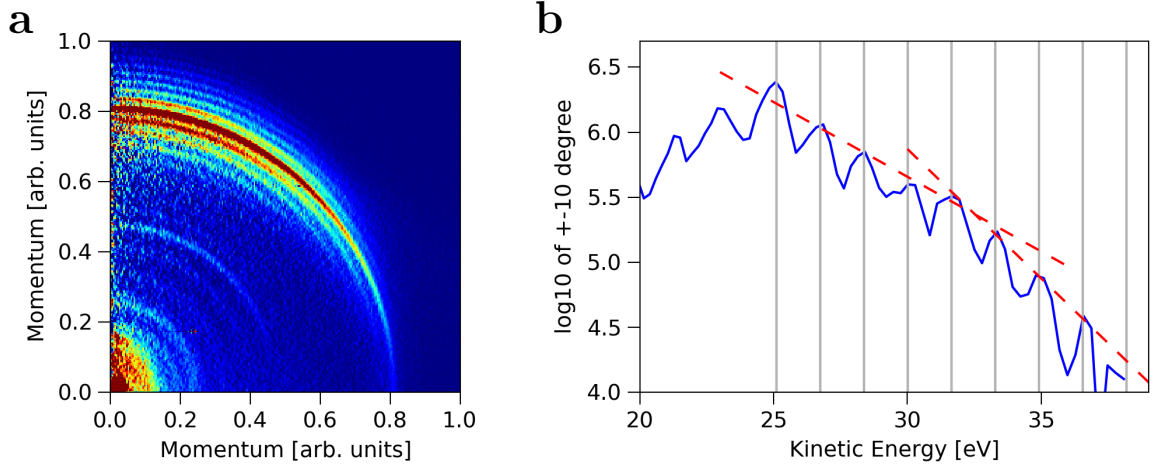
Figure 5.6: **a:** Cut through photoelectron angular distribution, originating from sideband generation in Argon with an XUV energy of 40.75 eV and an IR peaks intensity of 4.11 TW/cm^2. The IR photon energy is 1.63 eV. **b:** Logarithmic plot of angular integrated photoelectron spectrum. Up to seven sidebands to the center kinetic energy are visible, with two regions of linear decay in intensity between the individual sidebands. The energy E_c is associated with the cut-off energy of the sideband generation which is linked to the intensity of the IR pulse in the focus.

$$w_{IR,FWHM} = 75 \ \mu m \tag{5.17}$$

which seems reasonable. If we neglect the hole in the IR beam that is created by the recombination mirror and assume that we focus a 2 cm mode over 125 cm we expect a focus of 37 μm FWHM. The discrepancy can be explained by the hole in the mode and aberrations in the focusing.

This technique can be used to calibrate the IR intensity in the focus with respect to the measured pulse energy behind the VMI. However this calibrations needs to be taken with caution. The IR mode homogeneity depends on the settings of the laser and sometimes hotspots can be observed in the mode and subsequently in the focus. The sideband calibration however will average out these effects.

5.5 Summary and Outlook

In the present status the monochromator covers XUV energies in the range of 3 eV to 50 eV. An energy resolution of 0.5 eV or better can be achieved for the complete energy range, although this corresponds to the smallest throughput due the small slit size. The transmission efficiency through the monochromator ranging from 6 % to 17 %, which is quite remarkable, considering the six optical elements, and is due to the off-plane mounting of the gratings, that is far superior to the conventional mounting. This translates into 10^6

to 10^7 photons per pulse at the end of the monochromator, depending on the XUV energy and the daily performance of the laser.

The conceptual design of the monochromator opens the possibility for excellent time resolution, due to the second recompression stage. Currently we are able to achieve a cross correlation between the XUV and IR pulse of about 35 fs . We are able to demonstrate that the recompression stage currently recompresses the XUV pulse by a factor of 0.18 and is necessary to achieve the excellent time-resolution. We conclude that we are limited by the IR pulse duration coming from the laser and are not reaching the theoretical limits in time-resolution below 5 fs yet.

Overall the monochromator alignment is now stable for over 2 years and allows quick online changes of XUV energy over the complete energy range during an experimental run without losing pump-probe overlap with the IR pulse. A change between gratings takes less than 10 seconds, a change between XUV energies using a single grating takes less than a second.

In the future two performance specifications can be improved. The time-resolution and the efficiency of the HHG process. In order to improve the time-resolution efforts are carried out to generate IR pulses with below 10 fs pulse duration by spectrally broadened IR pulses coming from the laser by means of self phase modulation inside a gas filled hollow fiber [51]. When the short IR pulse is used to generate the XUV pulse the small XUV spectrometer in the first chamber of the monochromator will be of great help, since it is beneficial to monitor the complete XUV spectrum while optimizing the HHG process. Additionally it might be interesting to see if the negative linear chirp of the XUV pulse coming from the HHG process can be compensated by an Aluminium (Zirconium) foil in the beam in order to further reduce the XUV pulse duration [52] .

Generally it can be said, that there are numerous possibilities for the improvement of the HHG source flux. Most interesting would be the generation of the HHG with a combination of IR plus the 2nd harmonic of the IR. This would generate harmonics with any IR photon energy, increasing the possible XUV energies that can be selected by the monochromator. Additionally it is expected that a shorter driver wavelength for the HHG process has a larger conversion efficiency into the XUV.

6 XUV Ionization of N_2

This chapter presents the results of static photoelectron and photoion spectroscopy on XUV light-induced dissociation of N_2. For six XUV energies in the energy range between 32.8 eV and 48.8 eV, photoion and photoelectron spectra are recorded using a velocity imaging spectrometer (VMIS). The static spectra are obtained simultaneously with the time-resolved data by recording XUV ionization of N_2 at large negative time delays, i.e. when IR pulse arrives at the interaction much earlier than the XUV pulse and does not affect the XUV ionization. The spectroscopic interpretation of the static N^+ ion fragment and electron spectra, and especially the relations between the two, are necessary for the interpretation of the time-resolved spectroscopy presented in the next chapter.

Static spectroscopy on XUV light-induced N_2 dissociation has a long history reaching back decades, when light sources ranging from VUV-lamps [53] to synchrotrons [54] were used. The interpretation and comparison with literature of the static spectra serves as a benchmark test for the monochromator beamline and will be essential for the interpretation of the time-resolved spectroscopy. However to our surprise we could not find N^+ fragment spectra for the complete XUV range covered in our experiment in the literature. A mismatch between the published literature on the potential energy curves relevant for describing the dissociation via the H-band of the N_2^+ manifold and the experimentally observed spectra, stimulated the new *ab inito* calculations that are presented in section 2.3. The degree of agreement between the new theoretical results and the experimental data is also discussed in this chapter.

6.1 Experimental Data

The photoelectron and photoion time-resolved XUV-IR pump-probe spectra are recorded for six different XUV energies in the range from 32.8 eV to 48.4 eV. The monochromator was tuned to transmit the maximum of each single harmonic. The bandwidth of the XUV pulse was not calibrated, but can be estimated from the slit width (226 μm) to be in the range between 0.4 eV to 0.6 eV, see also chapter 5.2. The central wavelength of the IR laser pulse is 795 nm (1.56 eV). This yields the following XUV energies:

	H21	H23	H25	H27	H29	H31
Energy[eV]	32.8	35.9	39.0	42.1	45.2	48.4

Table 6.1: XUV energies for the individual harmonics. The energy of the IR photon is 1.56 eV corresponding to a wavelength of 795 nm.

From now on we refer to the XUV energy by the harmonic number. For each harmonic, time-resolved photoion (N^+) and photoelectron spectra are recorded. This is done in four separate measurement runs, in blocks of three neighbouring harmonics (H21,H23,H25) or (H27,H29,H31), for photoelectrons or photoions. The data sets are listed in the table 6.2.

Dat.	HH	E/I	Steps	Range [fs]	Frames	#Av.	Du.[hrs]	En.Cal. (a)
A1	H21	El	81	800	500	10	7.6	1.822e-3
A2	H23	El	81	800	500	14	10.6	1.841e-3
A3	H25	El	81	800	500	12	9.1	1.876e-3
B1	H27	El	81	800	500	11	8.3	2.761e-3
B2	H29	El	81	800	500	18	13.6	2.755e-3
B3	H31	El	81	800	500	25	18.9	2.780e-3
C1	H21	Ions	100	1000	500	7	5.3	9.7727e-4
C2	H23	Ions	100	1000	500	7	5.3	9.7727e-4
C3	H25	Ions	100	1000	500	7	5.3	9.7727e-4
D1	H27	Ions	81	800	500	10	7.6	1.47503e-3
D2	H29	Ions	81	800	500	20	15.2	1.47503e-3
D3	H31	Ions	81	800	500	24	18.2	1.47503e-3

Table 6.2: The labels A, B, C and D indicate the separate measurement runs. Within the measurement run, the pump-probe delay was scanned back an forth for a single XUV energy before switching to the next one. The column "Steps" gives the number of recorded pump-probe delays in a single scan and the column "Range" gives the scan range in fs. "Frames" refers to number of camera shots recorded for each delay step. The camera is recording the VMIS images with about 30 fps. "#Av." gives the number of scans recorded and "Du." the corresponding time. "En." gives the energy calibration factor defined in equation 6.2, see text for detailed discussion.

The VMIS settings are slightly different for the individual groups and first the energy calibration procedure for the spectra shall be presented.

6.2 Energy Calibration

Energy calibration of both electron and ion spectra is important to extract precise information on their kinetic energies. The calibration parameters depend on the geometry of the VMI, voltage and position of the interaction region within the spectrometer and are not always straightforward to calculate. The most reliable method, also applied here, is to use spectroscopic features with known kinetic energies to calibrate the energy axis at given experimental conditions.

6.2.1 Ions

In figure 6.1 2D-slices through the 3D momentum distribution for N^+ for all six harmonics are shown. The magnification of the VMIS was set differently for the two ion measurement
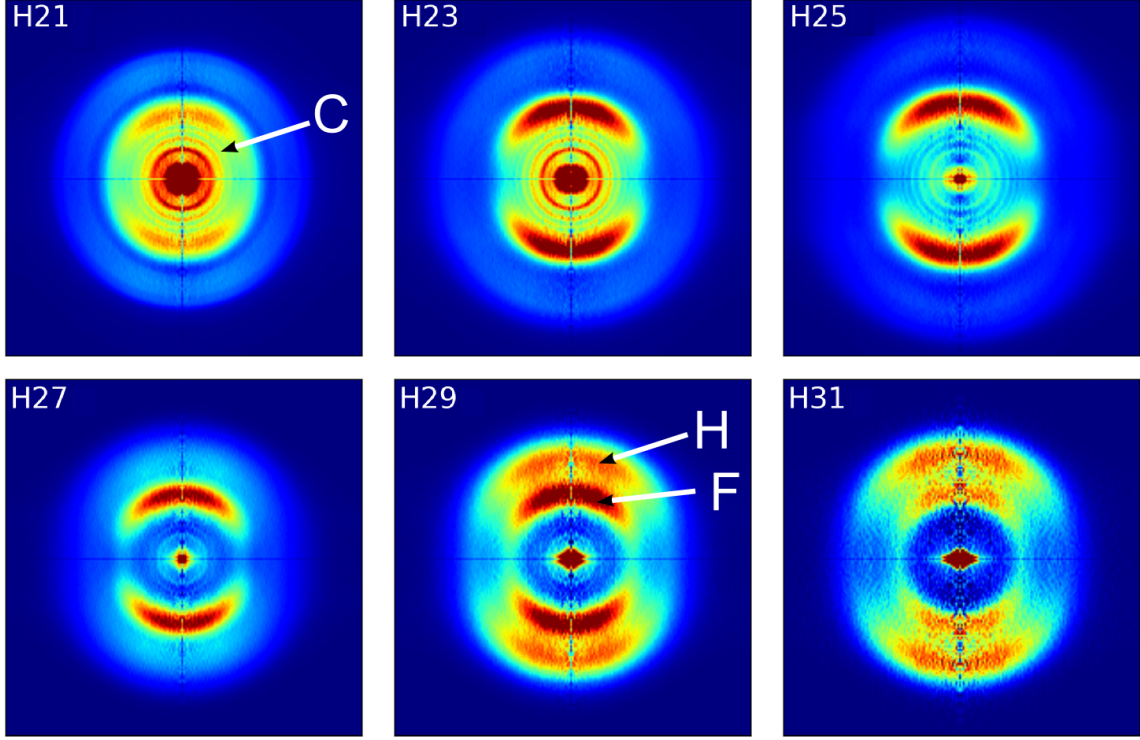
Figure 6.1: 2D cut through 3D momentum distribution of N^+ fragments. Images are normalized to the intensity of the feature F, see 6.2.1. With increasing XUV energy the ratio in signal strength between H and F is changing. For all six harmonics the vibrational progression of the C-State dissociation is visible, being the strongest for H21. Note: The VMI voltages are set differently for H21-H25 and H27-H31.

ν	1	2	3	4	5	6	7	8
Energy[eV]	23.583	23.831	24.083	24.331	24.576	24.871	25.054	25.286

Table 6.3: Vibrational states of the C state.

runs C (H21-H25) and D (H27-H31), resulting in different energy calibrations for the sets. For the energy calibration the relatively sharp spectral features at small velocities in the middle of the image are used. They are easily visible for the lower harmonics and start to vanish for higher XUV energies. They arise from the vibrational progression of the pre-dissociative C-State. The C $\left(^2\Sigma_u^+\right)$ state itself is a bound state with the lowest vibrational level having a binding energy of 23.583 eV which is slightly below the first dissociation limit L1 with 24.293 eV. However for vibrational levels higher than four ($\nu \geq 4$) the total energy is above the L1 limit and the C-state can pre-dissociate by vibrational coupling to the D $\left(2\Pi_g\right)$ state which is connected to the L1 limit [55, 56]. The binding energies of the vibrational C-states are listed in the table 6.3. For a diatomic molecule there is a direct connection between the initial excited ionic state and the final kinetic energy
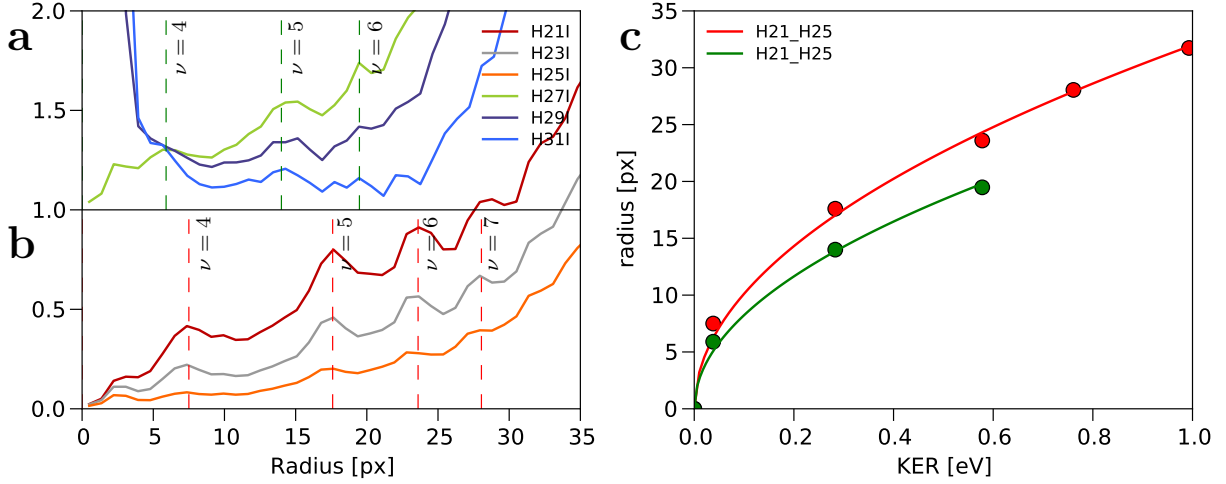
Figure 6.2: **b:** Radially integrated N^+ distribution for harmonics H21-H25, corresponding to measurement set C_{1-3}. **a:** Radially integrated N^+ distribution for harmonics H27-H31, corresponding to measurement set D_{1-3}. The spectral KER features at small radii are the vibrational progression of the pre-dissociating C-state. Vibrational states with $\nu \geq 4$ of the bound C-state can dissociate by coupling to the D-state which is adiabatically connected to L1 limit. **c:** For sets C_{1-3} and D_{1-3} the vibrational states are used to calibrate the KER-spectra of the N^+ spectra using a quadratic dependency given by equation 6.2. The calibration is different for the sets C_{1-3} and D_{1-3} due to the different VMIS setting used in the measurement runs.

of the dissociating atomic fragments. The excitation energy in the ionic state is split between kinetic energy of the fragments upon dissociation and the electronic excitation of the fragments. Due to momentum conservation the kinetic energy is equally split between the two fragments. The complete kinetic energy release (KER) is then given by

$$KER = E_B - E_L \tag{6.1}$$

where E_B is the binding energy of the ionic state and E_L is the dissociation limit. The electronic excitation stored in the individual fragments results in different dissociation limits E_L and the full KER can then directly be deduced by measuring the velocity of a single N^+ fragment. In figure 6.2a the angular integrated radial distributions are plotted, showing the vibrational states of the C-state. It is assumed that there is a quadratic dependency of energy on radius, see also section 3.3.10:

$$E(r) = a \cdot r^2 \tag{6.2}$$

where a is the calibration factor and r is the radius. A fit to the vibrational states is shown in figure 6.2c and the calibrations factors a are listed in table 6.2. The calibrated
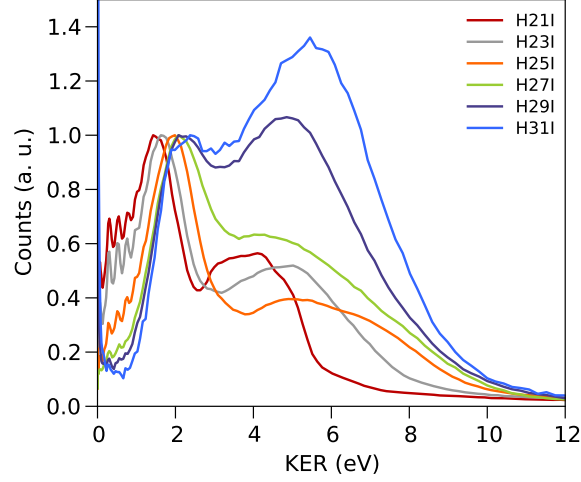
Figure 6.3: Static N^+ KER spectra for the six harmonics. The spectra are normalized to the F-feature around 1.8 eV. A broad feature appearing at 6 eV for harmonics H27-H31 is commonly association with the dissociation via the H-band [6].

KER spectra are presented in figure 6.3. They are normalized to a pronounced feature at 1.8 eV that is associated with the dissociation via the F-state with a binding energy of 28.5 eV and connected to the L3 dissociation limit at 26.7 eV, resulting in a KER of 1.8 eV. For higher KER around 6 eV a broad peak is observed that is changing its width and amplitude with harmonic order. For XUV energies above 37.5 eV (H25-H31) the dissociation is assumed to proceed via the H-state [6]. A more detailed discussion will follow in section 6.3.

6.2.2 Electrons

In figure 6.4 2D slices through the 3D momentum distribution for all six harmonics are shown. Sets A (H21-H25) and B (H27-H31) are recorded with different VMIS settings. For set B higher voltages are used to reduce the size of the VMI image to fit the electrons with higher kinetic energy onto the detector. For all images the strong feature corresponding to the fastest electrons is clearly visible. These electrons are originating from ionization into the ionic ground state (X) and the next two excited states of the N_2^+ ion, the A and B state. The A state has the largest XUV ionization cross section of the three [14] and its ionization potential of 16.9 eV in combination with the XUV energies in table 6.1 is used to calibrate the kinetic energy scale. For the ionization by a single XUV photon the kinetic energy of the electron is simply the difference between the binding energy and the photon energy.

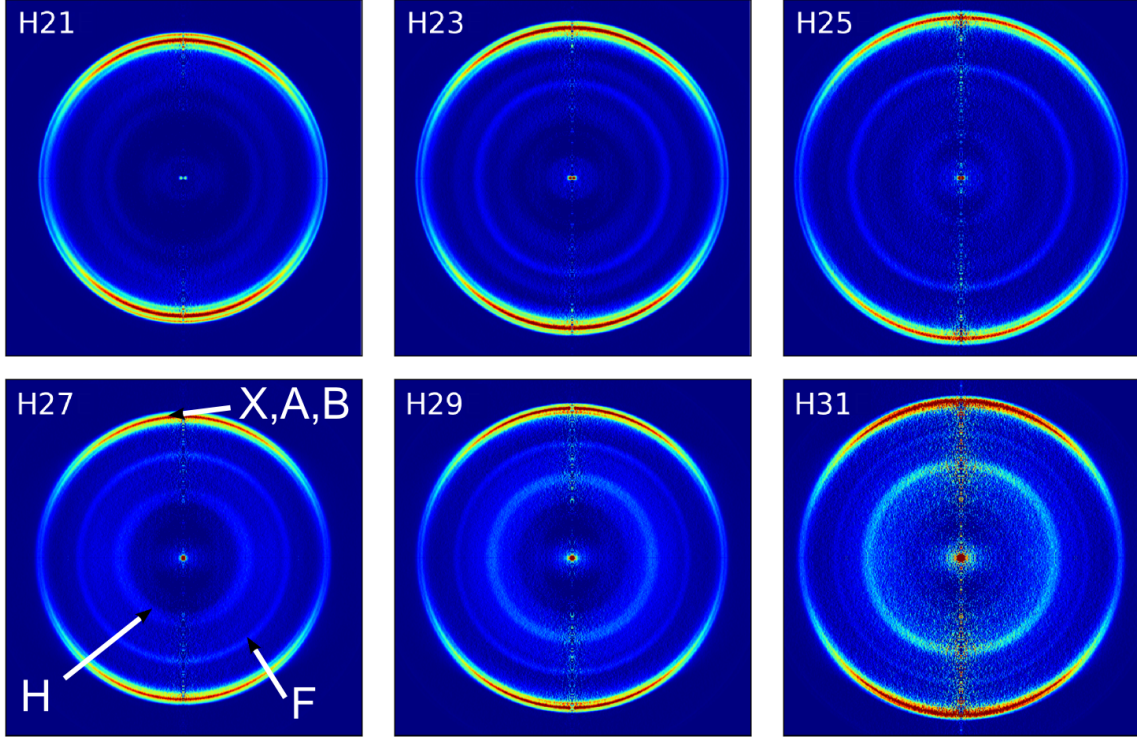$$E_{kin} = E_{XUV} - E_B \tag{6.3}$$

Figure 6.4: 2D slice through the 3D momentum distribution for photoelectrons and all six harmonics. H21-H25 (set A_{1-3}) and H27-H31 (set B_{1-3}) are recorded with different VMIS settings. For all six harmonics the electrons corresponding to the ionic states X,A and B are the most dominant feature in the images. The distributions are normalized to the maximum of this feature. The increase in momentum with increasing XUV energy is clearly visible. For H25 and higher harmonics both the F-state and the H-band can be seen clearly.

The calibration is performed for each harmonic individually, and the calibration factors are listed in table 6.2. The changes in calibration factors of equation 6.2 within the sets are only minor. The small variations in the factors probably originate from the monochromator not being tuned exactly to the maximum of the harmonic peaks. The variation in calibration factors corresponds to an error in the energy scale that is below 0.2 eV and therefore within the spectral width of the XUV pulse. In the following this error is assumed to be negligible.

In figure 6.5 the calibrated spectra are presented. The increasing kinetic energy of the electrons associated to the X, A and B state with harmonic order is visible. The energy resolution for the spectra belonging to the B set is slightly worse. The reason is the stronger magnification of the VMIS, that is used to focus the high energy electrons on the detector. The interpretation of the other features in the spectra is given in the next section.
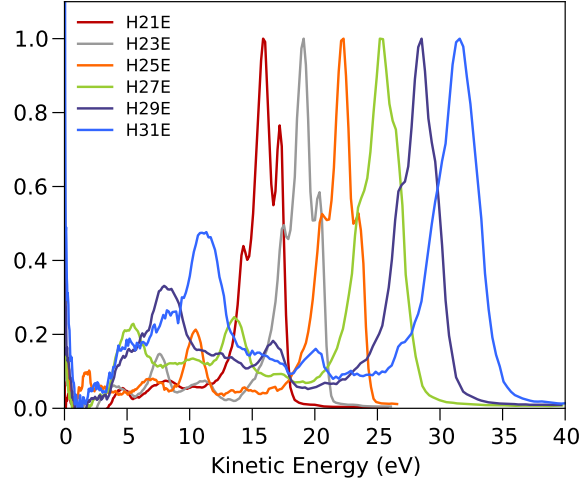
Figure 6.5: Electron kinetic energy spectra for all six harmonics. The ionic states X, A and B result in a strong photo-line in the photoelectron spectrum that has increasing kinetic energy with increasing XUV energy. For the set of harmonics H27-H31 the three states are less resolved in energy due to different magnification settings of the VMIS. The spectra are normalized to their maximum.

6.3 Photoion and Photoelectron Spectra

This section presents the spectroscopic interpretation of the photoion and photoelectron spectra and highlights the connection between the two. The obtained results demonstrate the advantage for time-resolved photoionization studies of a spectrally filtered HHG source over the complete HHG frequency comb. Thanks to the well-defined photon energy of the filtered source it is possible to directly deduce the photoionization cross-section of different ionic states from the photoelectron spectrum and then associate different dissociation channels with these ionic states. With the energy resolution of about 0.4-0.6 eV the photoelectron spectra are not comparable with results obtained from high resolution photoelectron spectroscopy [54], but good enough to clearly resolve the major ionization channels.

We can make use of the scaling of different features in the photoelectron spectrum with XUV energy to establish the correspondence between the photoelectrons and photoions. In figure 6.6a the photoelectron spectra are plotted against the binding energy of the electrons, by subtracting the XUV energy from the measured kinetic energy. Three distinct features are visible. The strong peak extending from 15 eV to 20 eV is originating from ionization into the ionic states X, A and B. At 28.5 eV the F-state is observable and the feature around 37 eV is the H-band, see also chapter 2. The spectra are in agreement with the literature, see for example [54]. The states that lead to dissociation must have a binding energy that is above the L1 (24.29 eV) limit. This energy region is plotted again in figure 6.6c. To compare the spectra for different XUV energies also in intensity, the spectra are
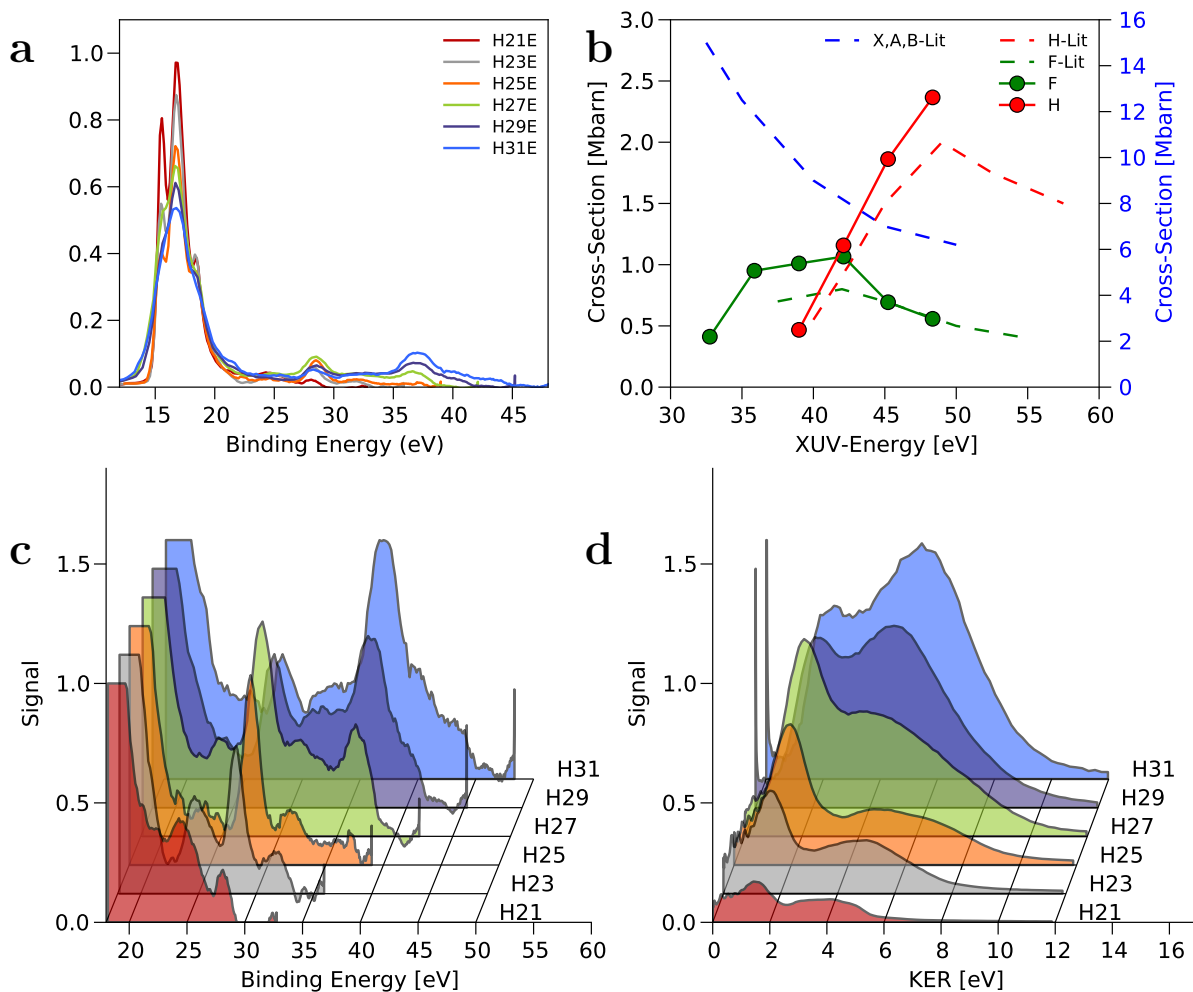
Figure 6.6: a: Photoelectron spectra plotted against the binding energy of the electrons. The spectra are normalized to the XUV-dependent cross section of the X,A and B state, given in [14]. **b:** Comparison of the cross-section for F-state and H-band with the literature values. **c:** Energy range of photoelectron spectra that possibly can lead to dissociation of the molecule. **d:** KER spectra normalized to the peak at 1.8 eV and the literature value for ionization into the F-state.

normalized to the area under the X,A,B feature multiplied by the literature values for the XUV energy dependent collective cross-section of this feature, taken from [14]. The cross section values are plotted in figure 6.6b. Note that the values for the sum of X,A,B feature (blue) has a different y axis.

In the normalized electron spectra in figure 6.6c we see that the amplitude of the F-state at 28.5 eV first increases with XUV energy and then decreases. The H-band at 37 eV can be accessed starting from harmonic H25 and its amplitude is increasing with energy. In fact, the area under the two features agrees with the cross-section values from the literature,

and confirms that the normalization to the X,A,B feature is successful. Additionally there are two minor features visible: The C-state is visible at 24.4 eV and another state with a binding energy around 32 eV, labeled the E state.

The ion KER spectra are presented in 6.6d. The feature around 1.8 eV originating from the F-state dissociating to the L3 threshold is normalized to the cross-section values for the F-state that are presented in the 6.6b. This way the scaling of different features in both the electron and ion spectra can be compared. For harmonics H29 and H31 a strong peak at zero KER is visible. These harmonics have a XUV energy above the N_2^{++} threshold, producing stable doubly-ionized molecules that appear in the same mass channel as N^+ and are therefore also within the gate time window of the VMIS.

One can observe that the height of the feature at 5.5 eV shows the same increase towards higher XUV energies as the H-state in the photoelectron spectrum starting from H25, see figure 6.6c. The higher energy KER contributions were always attributed to dissociation via the H-Band, see [6] or [57]. However, to our surprise, the observed kinetic energies are not reproduced by the calculation for the PE-curves in [15]. There the dominant state of the H-band around 37.5 eV is connected to the L6 dissociation limit, which results, for adiabatic dynamics, in a KER of 8.9 eV. We observe the peak near 5.5 eV. The disagreement between data and theory triggered the efforts to improve the *ab initio* calculations for the H-band. The calculations are presented in section 2.3.

6.3.1 Comparison of the Electron and Ion Spectra

In figure 6.7 electron spectra (a) and ion spectra (b) for H27-H31 are plotted separately to facilitate the assignment of the features. The F and H features are marked in the electron spectra by shaded areas. In the ion spectra the same areas are plotted with a shift on the energy scale assuming that the F-state dissociates towards the L3 limit, in agreement with theory, and the H-band dissociates towards the L9 (31.9 eV) limit. The good agreement observed in figure 6.7b demonstrates that the KER feature at 5.5 eV indeed corresponds to dissociation of the H-band (37.5), but the dissociation limit is L9 contrary to the results of [15]. The next threshold lower in energy is L8 (30.7 eV), which results in a KER of 6.8 eV, which is too high and does not reproduce the observed KER position around 5.5 eV. A dissociation towards the L10 (34.6 eV) limit leads to a KER of 2.9 eV, which is too low. Not only is the energy of the KER reproduced but also the shape is in good agreement. This leads to the conclusion that the dominant part of the H-band dissociates towards the L9 threshold. This is not at all expected since the H-band is made up from a series of states, see 2.3, that are connected to different limits. Only in the case that all states are connected to a single dissociation limit the spectral width of the photoelectron spectrum reproduces the spectral width of the KER features, this is called imaging principle. In case of a single limit the shape of the feature both in the electron spectrum and in the KER is defined by the shape of the PE curves in the FC region. We will now compare our findings with the new *ab initio* calculations.
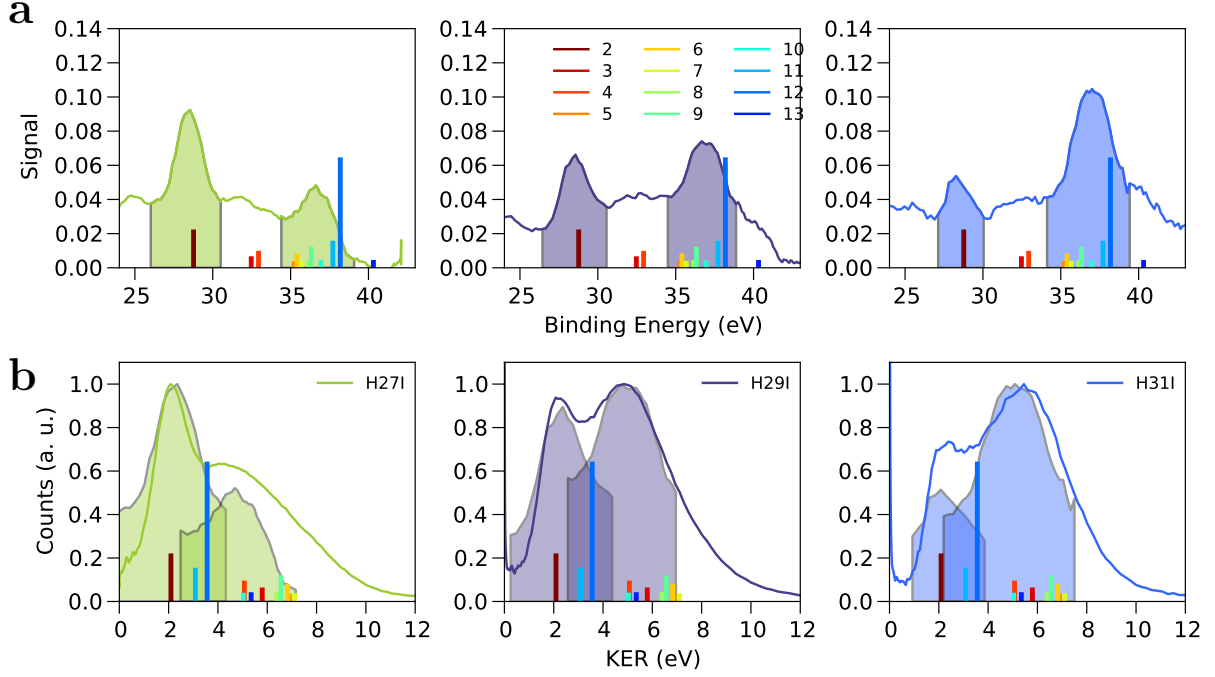
Figure 6.7: a: Photoelectron spectra for H27-H31 showing the F-state and H-band. The shaded areas are transferred to the KER spectra in **b:** by connecting the F-state to L3 and the H-band to L9. The colored lines indicate the different KER contribution resulting from the PE-curves presented in section 2.3. The height of the lines is proportional to the $2\sigma_g^{-1}$-hole character of the states.

6.3.2 Comparison with Theory

The mismatch between the observed experimental KER and the calculation for the Σ_g states presented in the literature in [15] has triggered the calculations presented in 2.3. In the following table a summary of Σ_g states, also from different publications, with a binding energy in the energetic region of the H-band is presented:

	Langhoff 1981 [14]			Aoto 2006 [15]			Kornilov/Ritze 2014					
nΣ_g	3	4	5	5	6	7	8	9	10	11	12	13
B. E. [eV]	37.3	37.4	40.0	37.7	38.0	38.5	36.2	36.3	37.0	37.7	38.2	40.3
Limit	L3	L4	L6	L6	L6	L7	L7	L7	L9	L10	L10	L11
KER	11.0	9.5	11.7	9.1	9 .4	8.7	6.4	6.6	5.0	3.1	3.6	5.3
$2\sigma_g^{-1}$	0.20	0.29	0.03	0.32	0.19	?	0.02	0.07	0.02	0.1	0.42	0.02

Table 6.4: Comparison between different *ab initio* calculations for states with a binding energy (B. E.) in the region of the H-band. Σ_g denotes the number of the state.

With the improvement of *ab initio* calculation over the years, the energy of the PE

curves is moving down in energy, and hence the H-band (37.5 eV) gets assigned to states with higher number n of the Σ_g manifold. Although the PE curves are moving down in energy the dissociation limit remains the same for a given number n. This leads to a lower KER for adiabatic dissociation via the H-band for improved *ab initio* calculations as it can be seen in the row KER in the table 6.4 . We generally can observe that our calculations produce KER in the energy region of about 6 eV, which corresponds well to the experimental observation.

In order to gain further insight which of these states actually reproduces best the data, also the $2\sigma_g^{-1}$-character of the states is listed in the table. The H-band originates from the creation of a $2\sigma_g^{-1}$ hole, and has a dominant one-particle configuration, similar to the X, A and B states. All other states in the relevant binding energy region have a dominant two-hole one particle configuration, see also section 2.2. Naturally we expect that the removal of a single hole is expected to have a large cross-section, and assume that the $2\sigma_g^{-1}$ hole density is proportional to the ionization cross-section.

In figure 6.7 the position of the Σ_g states and the corresponding KER of the new calculations are indicated as vertical lines. The height of lines reflects the $2\sigma_g^{-1}$ hole density. The position of the F-state is nicely reproduced, which is the second state with Σ_g symmetry. A series of states is close to the center of the experimentally measured energy of the H-band in the electron spectrum. State 10 is a little below the peak of the photoelectron spectrum at 37.5 eV and has a small $2\sigma_g^{-1}$ hole density. It is however connected to the L9 threshold and is reproducing the KER maximum at 5.5 eV. The state with the biggest $2\sigma_g^{-1}$ hole density is state 12. It is slightly too high in energy and is connected to the L10 threshold. This state produces a too low KER of 3.6 eV.

The mismatch between theory and experiment may have the following explanations. First the calculation could produce incorrect hole densities, and the 10th state should be dominating the H-band. This is not impossible, since all the states are close in energy and only involve minor rearrangements of other electrons to other shells. Alternatively, the assignment of the large hole density to state 12 could be correct, but the calculations still do not reproduce the binding energy perfectly. There could be a strong non-adiabatic coupling between states 12,11 and 10. State 12 would be dominantly excited and dissociating towards the L9 threshold producing the KER at 5.5 eV. All options are possible explanations and currently neither can be ruled out.

6.3.3 Summary

The recorded photoelectron spectra are in good agreement with the literature, essentially reproducing the XUV energy dependent cross-sections in [14]. However the ion KER spectra we recorded are only partially agreeing with the published literature on the PE-curves describing the dissociation. For dissociation via the H-band we observe a mismatch between [15] and the recorded KER spectra. By comparing electron and ion spectra we can conclude that the H-band is dominantly dissociating towards the L9 threshold. The new *ab initio* calculations presented in section 2.3 generally reproduce this finding, but also raise the question about the exact dissociation dynamics at short internuclear distances.

7 Dissociation Dynamics of N_2

In this chapter the photoion and photoelectron spectroscopy of N_2 introduced in the previous chapter is extended into the time domain. The major scientific goal of the experimental effort is to gain further insight into dissociation induced by ionization into the energy region around the H-band (37.5 eV). In the following we present a summary of the known dissociative ionization channels. Above XUV photon energies of 24.3 eV the nitrogen molecule can undergo dissociative ionization. The lowest electronic state of the molecular N_2^+ ion leading to dissociation is the C-state, with an excitation energy of the vibrational ground state of 23.6 eV. The vibrationally excited molecular ion with $\nu \geq 4$ has a total energy above the dissociation limit and can pre-dissociate by coupling to the D-state, see also chapter 2. This happens on a nano- to picosecond time-scale depending on the vibrational state [56]. The lowest state in energy leading to direct dissociation is the F-state with an excitation energy of 28.4 eV. This dissociation process is ultra-fast and happens on a sub-100 fs timescale. For even higher XUV energies it becomes possible to ionize the inner valence shell with $2\sigma_g$ symmetry and an energy of 37.5 eV. This is associated with a series of ionic states, labeled the H-band, that also result in an ultra-fast dissociation. In this high energy region the electron-electron interactions are leading to complex multi-electronic dynamics during the bond breaking of the molecule.

In this chapter we present the results on varying XUV photon energy in the range of 32 eV to 48.4 eV around the threshold energy of 37.5 eV of the H-band, and probing the induced ultrafast electronic and structural dynamics with a moderately strong IR pulse with peak intensities of a few TW/cm^2. The IR pulse is strong enough to ionize the electronically excited fragments created by the XUV pulse, essentially visualizing the dynamics in the time domain. We are recording both the IR induced time delay dependent changes in the KER and the electron spectra. The major channels that we are able to identify in the time-resolved spectra are:

- Ionization into the dissociative ionic states of the H-band by the XUV pulse. The dissociation dynamics are probed by ionization of the neutral atomic fragment, inducing a Coulomb explosion. This channel is discussed in section 7.3.

- Resonant excitation of neutral dissociative states by the XUV pulse. The induced dynamics are probed by the IR pulse via single ionization of one of the neutral atomic fragments. This channel is discussed in section 7.4

- Resonant excitation of dissociative auto-ionizing states. The dynamics are probed by further ionization and changes in the KER via the IR pulse. This channel is discussed in section 7.5

It appears to be possible to distinguish these different dissociation channels, that are partly spectrally overlapping only by comparing the results for different XUV photon energies and by identifying the relations between electron spectra and KER spectra in case of additional ionization by the IR pulse. The presented results are therefore an excellent demonstration of the experimental advantages of the monochromator beamline that allows to tune the XUV photon energy, while having a short pulse duration (good time-resolution) at the same time.

Before the individual dynamical processes are discussed in detail we present a normalization procedure that is necessary to improve the signal-to-noise ratio in the datasets and which is crucial for interpretation of the data. The procedure involves a general spectroscopic interpretation of the observed features and will therefore also lay the groundwork for the discussion of the individual dynamical processes.

7.1 Preparatory Analysis of Experimental Data

The time-resolved spectra are recorded separately for electrons and N^+ ions by repetitive scanning of the XUV-IR time delay in forward and backward directions. The data are recorded for individual XUV photon energies from harmonic H21(32.8 eV) to H31 (48.8 eV). From now on we will call a series of time-resolved spectra for a single harmonic as a map for this harmonic. Despite repetitive scanning the weak signals induced in the KER and electron spectra by the IR remain noisy. The data quality can be significantly improved by employing a normalization scheme for both the ion spectra and electron spectra. While the normalization scheme for the electron maps is simple and relies on features in the photoelectron spectra, which are expected to be independent of pump-probe delay, the normalization of the KER maps involves a more sophisticated algorithm that exploits the spectroscopic relation between the ion and electron data and already requires a preliminary interpretation of the data. The schemes are described in the following for the electron and ion map of H23.

Normalization of the Photoelectron Spectra

Figure 7.1 presents the normalization procedure for the time-dependent photoelectron map corresponding to H23 (35.9 eV) as an example. In figure 7.1a the unnormalized pump-probe map is shown. The different spectroscopic features are explained in detail in chapter 6.3. In brief, the ionization into the X, A and B states results in kinetic energies of approximately 19 eV, the C-state leads to 11 eV electrons, the F-state leads to 7 eV electrons and the E state to 4 eV kinetic energy. At the overlap of the pump and probe pulses, sideband generation for the X, A and B feature in the photoelectron spectrum is visible. In figure 7.1b the XUV only (static) photoelectron spectrum is subtracted to enhance the visibility of the dynamics. In addition to the dominant sidebands of the X, A, and B peak also the sideband generation on electrons originating from ionization into the F-state around 7 eV is visible in this map. Additional low energy electrons with kinetic energies below 2 eV can be seen.
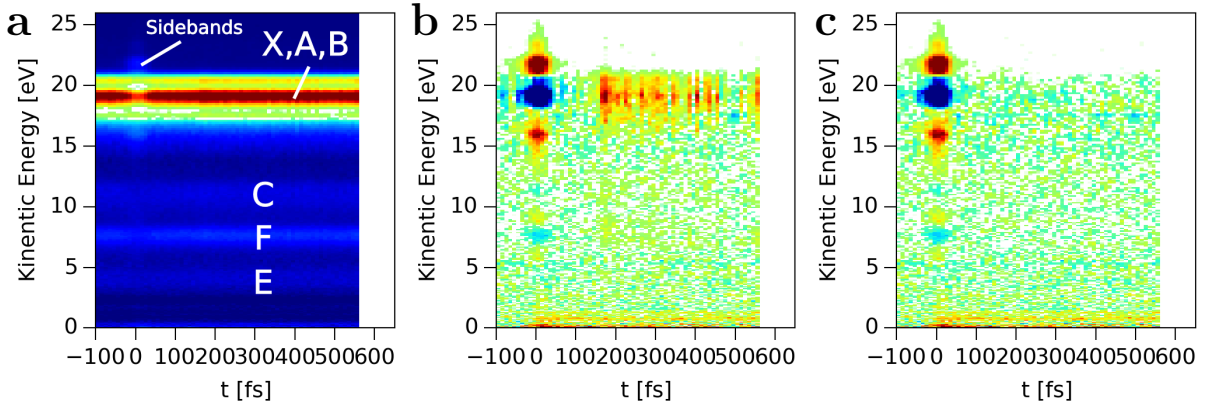
Figure 7.1: Normalization of time-resolved photoelectron maps of H23 **a:** Unnormalized time-resolved map. The features corresponding to different ionization channels are label on the side (see chapter 2 for details). **b:** Unnormalized differential map. The static XUV-only spectrum is subtracted. During pump-probe overlap sideband generation is observable. For longer time delays noise around the energy 19 eV is visible. **c:** Map normalized to the total counts with kinetic energy above 2 eV. Less noise around kinetic energies of 19 eV is visible.

In the map noise between the individual time steps can be observed. This is the most visible in the kinetic energy region around 19 eV, where the signal drifts in intensity and fluctuates between the individual time steps. The noise between individual time steps originates from the pulse-to-pulse XUV energy fluctuations originating from the highly non-linear HHG process. The fluctuations are random but do not average out completely, although the data acquisition time can take up to 22 hours for some of the maps. The slow drift is mostly due to the target gas pressure slowly changing over the time of the measurement, since it was not stabilized actively.

It is possible to reduce the noise by taking into account that sideband generation does not produce any additional electrons. The electrons are only accelerated or decelerated by the electric field of the IR pulse. Therefore the total count rate of the photoelectron spectrum for the energy region including photolines and their sidebands is independent of the pump-probe delay. However for the slow electrons with kinetic energy below 2 eV this is not the case. These are additional electrons originating from ionization induced by the IR pulse. The electron maps are therefore normalized to the total counts of electrons with kinetic energy above 2 eV, since these are independent of the XUV-IR pump-probe time delay. The normalized map is presented in figure 7.1c. The slow drift with delay and the noise between the time steps is greatly reduced. The same procedure is performed for all photoelectron maps recorded in these experiments. The sidebands transient of the combined X,A and B feature can also be conveniently used to determine time zero (the time, at which XUV and IR pulses fully overlap) and the time resolution of the experiment. The FWHM of the Gaussian shaped cross correlations of XUV pulse and IR pulse lies in the range between 44 fs and 47 fs for the different electron maps.
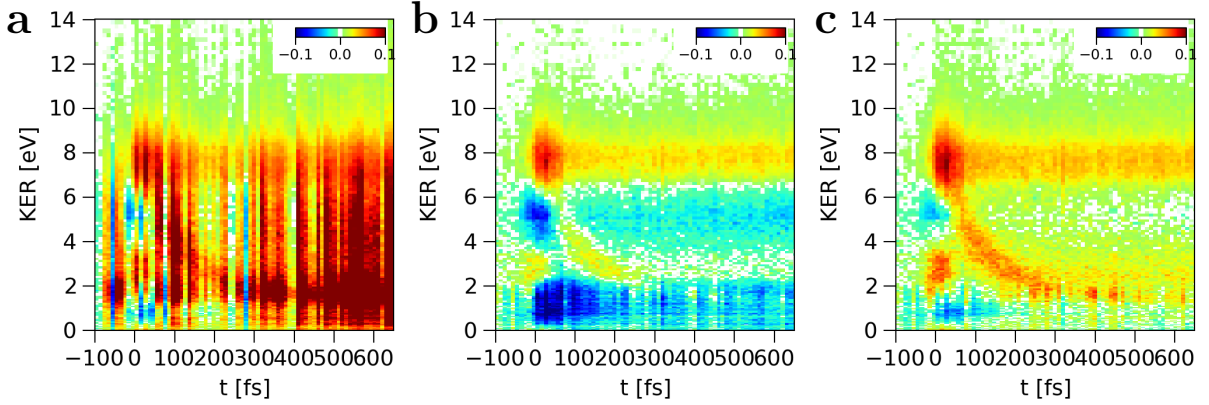
Figure 7.2: Normalization procedure for the ion KER map of H23 **a:** Unnormalized differential KER map. **b:** Map normalized to total counts. **c:** Normalized map corrected by transient shape of slow electrons from the electron map of harmonic H23 (see text for details).

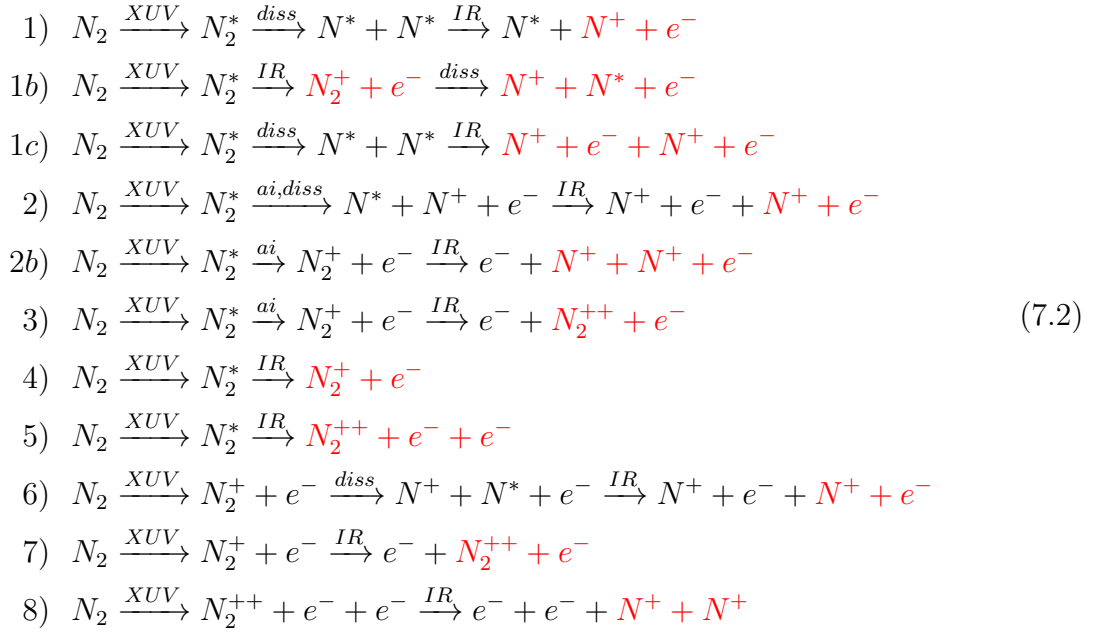### Normalization of the Ion KER Spectra

As an example for the normalization scheme for ion maps the KER map for H23 is presented in figure 7.2. In figure 7.2a the differential unnormalized map is shown. In figure 7.2b the differential map is normalized to the total count rate of ions for each individual step of the pump-probe delay is presented. This normalization greatly improves the quality of the map. However it introduces systematic offsets in the differential spectra, because it assumes that the total ion yield is independent of the pump-probe delay. This is certainly not the case as the IR pulse causes additional ionization of the fragments created by the XUV pulse. Figure 7.2c shows a map that is corrected for these systematic deviations. The correction algorithm is presented in the following.

The IR pulse induces changes in the KER spectrum over the complete spectrum, see figure 7.2a, and therefore no time-independent part of the spectrum can be used to normalize the data without further complications. However, as long as the total count rate in the spectrum stays constant with time delay the spectra could be normalized the total count rate for each time step. Unfortunately we can observe in the electron map that the IR pulse also ionizes the molecule or atomic fragment and creates additional electrons that appear as electrons with a kinetic energy below 2 eV. The strategy to normalize the KER map is therefore the following: We normalize the ion spectrum to the total counts at each individual time step (map 7.2b) and then correct the induced error by multiplying the complete spectrum at each time delay with a correction factor that is deduced from the IR-induced electrons in the electron map for that time step in the following way:

$$I_{KER,Corrected}(E,t) = \frac{I_{KER,Raw}(E,t)}{\int_0^\infty I_{KER,Raw}(E,t)dE} \left(1 + \alpha \cdot \int_0^{2\ eV} I_{EL,Corrected}(E,t)dE\right) \quad (7.1)$$

where α is an amplitude that is chosen such as to correctly account for the additional N^+ ions created by the IR pulse. In practice, it appears that the N_2^{++} signal present in the KER maps at zero kinetic energy (hard to be visible in the map by eye) is weakly affected by the noise. The constant α is thus chosen such as to match the N_2^{++} transient in the corrected map to that in the original map. This algorithm is based on one important assumption, namely that for each additional electron created by the IR pulse there is also only a single extra N^+ atom or a stable N_2^{++} ion, which is also detected in the experiment, because it has the same mass-over-charge channel as the N^+. The N_2^{++} fragments have zero KER and are hard to see by eye in the maps. In order to discuss if this assumption holds a list of all possible IR-induced channels that lead to additional charged fragments follows:

$$
\begin{aligned}
&1) && N_2 \xrightarrow{XUV} N_2^* \xrightarrow{diss} N^* + N^* \xrightarrow{IR} N^* + \textcolor{red}{N^+ + e^-} \\
&1b) && N_2 \xrightarrow{XUV} N_2^* \xrightarrow{IR} \textcolor{red}{N_2^+ + e^-} \xrightarrow{diss} N^+ + N^* + e^- \\
&1c) && N_2 \xrightarrow{XUV} N_2^* \xrightarrow{diss} N^* + N^* \xrightarrow{IR} \textcolor{red}{N^+ + e^-} + N^+ + e^- \\
&2) && N_2 \xrightarrow{XUV} N_2^* \xrightarrow{ai,diss} N^* + N^+ + e^- \xrightarrow{IR} N^+ + e^- + \textcolor{red}{N^+ + e^-} \\
&2b) && N_2 \xrightarrow{XUV} N_2^* \xrightarrow{ai} N_2^+ + e^- \xrightarrow{IR} e^- + N^+ + \textcolor{red}{N^+ + e^-} \\
&3) && N_2 \xrightarrow{XUV} N_2^* \xrightarrow{ai} N_2^+ + e^- \xrightarrow{IR} e^- + \textcolor{red}{N_2^{++} + e^-} \\
&4) && N_2 \xrightarrow{XUV} N_2^* \xrightarrow{IR} \textcolor{red}{N_2^+ + e^-} \\
&5) && N_2 \xrightarrow{XUV} N_2^* \xrightarrow{IR} \textcolor{red}{N_2^{++} + e^- + e^-} \\
&6) && N_2 \xrightarrow{XUV} N_2^+ + e^- \xrightarrow{diss} N^+ + N^* + e^- \xrightarrow{IR} N^+ + e^- + \textcolor{red}{N^+ + e^-} \\
&7) && N_2 \xrightarrow{XUV} N_2^+ + e^- \xrightarrow{IR} e^- + \textcolor{red}{N_2^{++} + e^-} \\
&8) && N_2 \xrightarrow{XUV} N_2^{++} + e^- + e^- \xrightarrow{IR} e^- + e^- + \textcolor{red}{N^+ + N^+}
\end{aligned}
\tag{7.2}
$$

where *diss* stands for dissociation, *ai* stands for autoionization and the * denotes an excited state. The fragments that are created by the IR are labeled in red. Except for the channels 4, 5 and 8 there is always a single extra count in the ion **and** electron spectra originating from the IR pulse. We argue that the channels 4, 5 and 8 are minor and can be neglected in the normalization scheme. Channel 4 and 5 only have a very small cross-section compared to channel 2 and 3, since resonantly excited neutral states with a binding energy high above the ionization threshold and are expected to be highly unstable leading to autoionization. Channel 8 can only be excited by H29 and H31, since these two XUV energies are above the double ionization threshold. The resulting KER of the two N^+ fragments is about 13.2 eV [58] if the dissociation of the stable N_2^{++} is induced by the IR pulse at the equilibrium internuclear distance. We cannot observe this high KER in the data and also can rule out this channel. We conclude that we can apply the suggested algorithm.
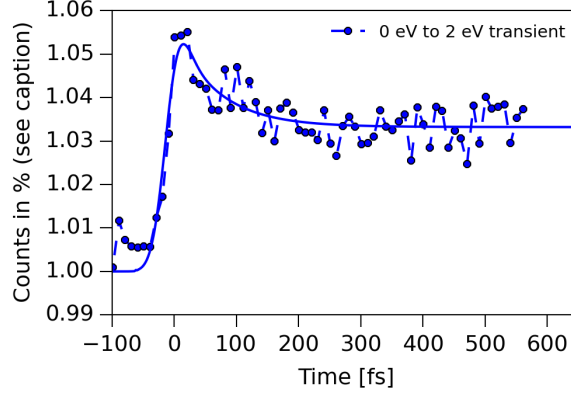
Figure 7.3: Electron transient for electrons with $E_{Kin} < 2\ eV$ in the electron map of H23.

In figure 7.3 the transient of the total counts of electrons with a kinetic energy below 2 eV is presented. To avoid a transfer of the noise in the electron transient into the KER spectra we fit an analytic curve to the transient. We choose a curve with two independent exponential decays convoluted with a Gaussian filter to the transient, since it turns out that this function can reproduce the shape sufficiently well. The fit function is given by the sum of single decays and a constant background, resulting in [59]:

$$S_{tot}(t, B, \sigma_{cc}, t_0, A_1, \tau_1, A_2, \tau_2) = B + A_1 S(t, t_0, \tau_1, \sigma_{cc}) + A_2 S(t, t_0, \tau_2, \sigma_{cc}) \qquad (7.3)$$

where

$$S(t, t_0, \tau, \sigma_{cc}) = exp\left[-\frac{t - t_0}{\tau}\right] exp\left[\frac{1}{2}\left(\frac{\sigma_{cc}}{\tau}\right)^2\right] \frac{1}{2}\left(1 + erf\left[\frac{1}{\sqrt{2}}\left(\frac{t - t_0}{\sigma_{cc}} - \frac{\sigma_{cc}}{\tau}\right)\right]\right) \quad (7.4)$$

and t_0 is time zero, A are the amplitudes of the individual transients, B is the background, σ_{cc} is the time-resolution of the measurement and τ are the decay constants. This fit function can be successfully fitted to the transients of the maps for all XUV energies (not shown). The corrected map after the application of the algorithm is presented in figure 7.2c. In fact we can observe that the algorithm works properly by comparing the amplitude of the depletion in the energy region from 4 eV to 6 eV for a time delays larger than 200 fs in the three maps: In the raw map presented in 7.2a and the corrected map in 7.2c we observe no depletion. In contrast we observe a depletion in the normalized but uncorrected map in 7.2b, since the IR pulse is creating additional N^+ fragments and therefore a uncorrected normalization to the total count rate is enhancing the depletion in the maps. We conclude that the algorithm works correctly.
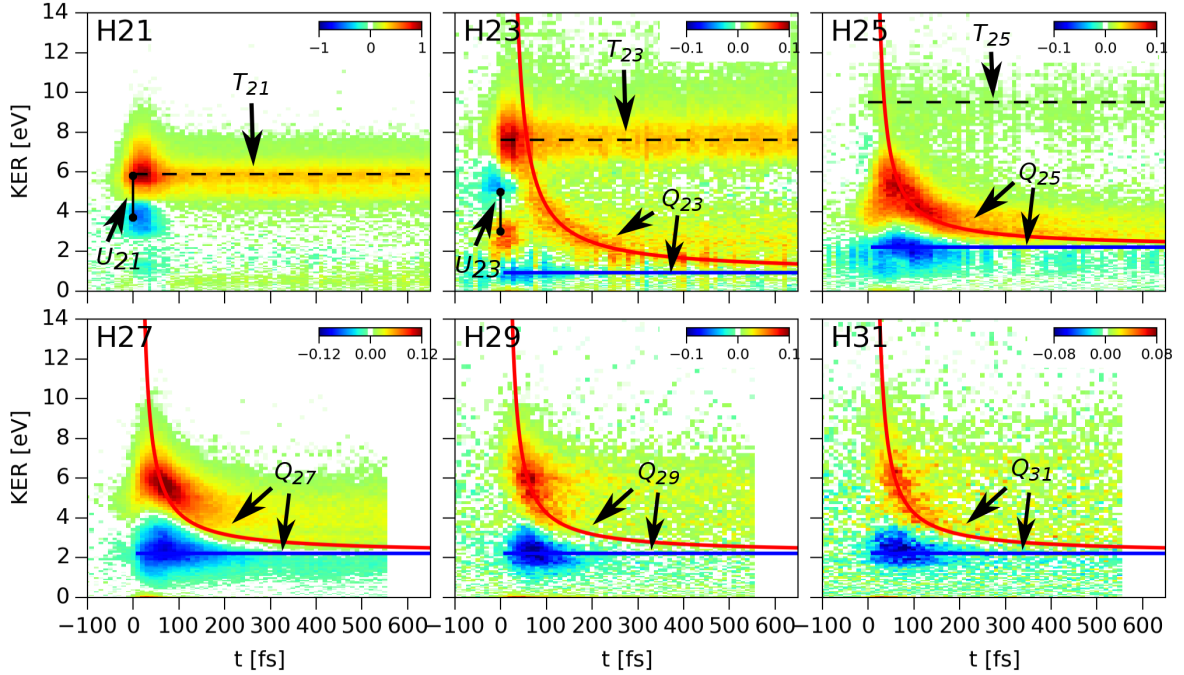
Figure 7.4: Labeling of features in the KER maps. The features T_{21}, T_{23} and T_{25} have a constant energy which does not change with pump-probe delay. The features U_{21} and U_{23} in H21 and H23 only appear during the pump-probe overlap. For H23-H31 we observe features with decreasing energy, labeled Q_{25} to Q_{31}. The feature Q_{23} is converging for long time delays to a different final KER with 0.9 eV in comparison to the features Q_{25} to Q_{31}, which converge to 2.2 eV.

7.2 Overview of Observed Spectroscopic Features

In figure 7.4 and figure 7.5 the normalized differential maps for all six XUV energies are presented for ions and electrons. The different maps are labeled by the XUV harmonic order. Different groups of features are labeled by the letters U, T, Q and W, where the subscript indicates the harmonic order. Features with a common label in figure 7.4 and 7.5 are assigned to the same process. Before we discuss the individual groups of features we will first make some general remarks on the interpretation of the time-resolved maps and especially on how we can exploit the change in XUV energy between the maps.

- If a feature can only be observed for a single harmonic, it likely derives from a neutral state of N_2 molecule that can only be excited resonantly with the XUV photon energy of that harmonic.

- Features that appear for XUV photon energies above a certain threshold can be associated with direct ionization.

For the interaction of the IR pulse with the neutral or ionic molecule the following statements are true:
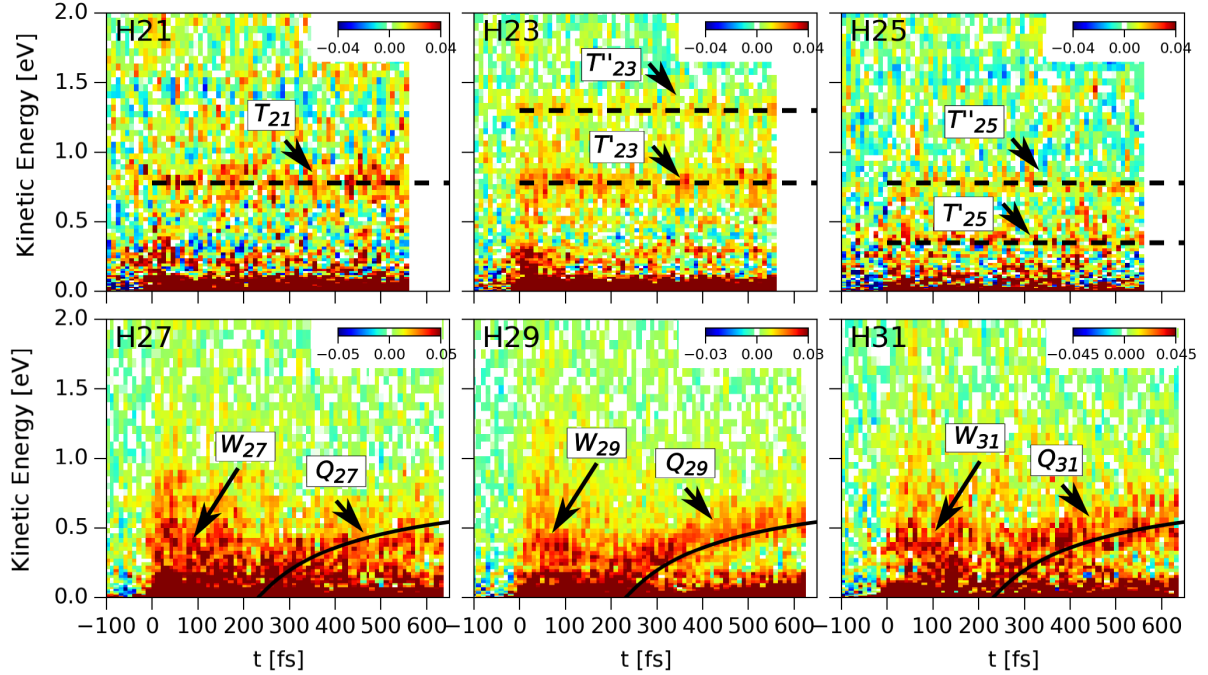
Figure 7.5: Labeling of slow electron features: For H21-H25 we see features with constant kinetic energy, they are labeled T_{21}, T_{23} and T_{25}. For H27-H31 we see slow electrons for short time delays, labeled W_{27-31} and a feature with an increasing energy for longer time delays labeled Q_{27-31}.

- If the IR probes a neutral state by ionization, there should be no corresponding depletion in the differential map.

- If the IR probes a singly charged state by ionization, there is a corresponding depletion signal in the map. The positive signal will be larger than the negative one, since additional fragments are detected. The ratio between positive and negative signals depends on the spectral overlap between the two contributions, however the total counts integrated over both parts are independent of the overlap, but only depend on the pump-probe delay dependent IR absorption cross-section.

- Coupling of dissociation pathways by the IR within the same manifold should lead to equal amounts of positive and negative signal.

Applying these rules we can identify different sets of features in the maps and give a short overview here to prepare the reader for the more detailed discussions in the following sections. The features labeled with Q in the ion maps consist of positive contribution with decreasing kinetic energy and corresponding depletion with a constant KER. The features can be grouped into two groups: Q_{23} and Q_{25-31}. They differ in the limit the positive and negative contributions converge to for long time delays. The fact that a depletion is observed leads to the conclusion that the IR is probing dissociation channels

that already led to an N^+ fragment after XUV ionization. In case of the feature Q_{23} this is a resonantly excited (it appears only for H23) autoionizing state. The group of features Q_{25-31} is associated with dissociative ionization. In the following we will demonstrate that they originate from ionic states of the H-band. For all features the positive contribution is larger than the negative, which leads to the conclusion that additional ion fragments are created by the IR pulse. The corresponding additionally created electrons are visible in the electron maps as the features Q_{27-31}. (The absence of the features Q_{23} and Q_{25} in the photoelectron maps is discussed later). The shape of the features for long time delays (>100 fs) deduces from the shape of the repulsive Coulomb potential that leads to repulsion of the two charged N^+ fragments after the secondary ionization by the IR pulse.

The features labeled T_{21-25} in the ion maps have a constant KER for all time delays, but differ in the value of the KER between the different maps. The features have no corresponding depletions. This leads to the conclusion that these features arise from ionization of neutral resonantly-excited states by the IR pulse. These states can be either dissociative or bound. The electrons originating from the ionization of the IR pulse can be observed in the electron maps also labeled as the features T_{21-25} .

The features U_{21} and U_{23} are only observable in the individual ion maps close to zero time delay. Since these features only appear for individual harmonics and we observe a depletion they have to arise from a resonantly excited autotionizing state. The IR pulse can further ionize the fragments, but can also only change the KER, by coupling the dynamics to a different dissociation limit.

The diffuse features W_{27-31} are electrons that cannot be clearly assigned to a single process. An interpretation will follow in the individual sections discussing the other features.

7.3 Features Q_{23} to Q_{31} - Coulomb Explosion

The features Q_{23-31} show the richest dynamics in the KER spectra and dominate the time-resolved maps for harmonics H23-H31 in figure 7.4. The dynamics observed for these features have a positive contribution with a time dependent decrease in KER energy and a corresponding depletion signal that has a constant KER. Upon a close look the features Q_{25-31} appear to be very similar, while the feature Q_{23} differs from them. Therefore we first describe the features Q_{25-31} and will return to the feature Q_{23} later. We evaluate the dynamics by integrating over separate energy regions in the KER map, which are dominated by the positive and negative signals, respectively. The transients for the positive and negative contributions of features Q_{25-31} are presented in figure 7.6 with the chosen energy ranges labeled in the caption. The sum of the positive and negative contributions (tot), also shown in the figure, is positive and rather constant over time. The positive contribution is therefore larger than the negative one. The positive (pos) and negative (neg) contributions in the maps appear to be stronger for shorter time delays because they are separated further apart in energy, while for longer delays they partially cancel each other. The IR pulse is therefore creating additional N^+ fragments and additionally is changing the KER of N^+ fragments that are already created by the XUV pulse, which
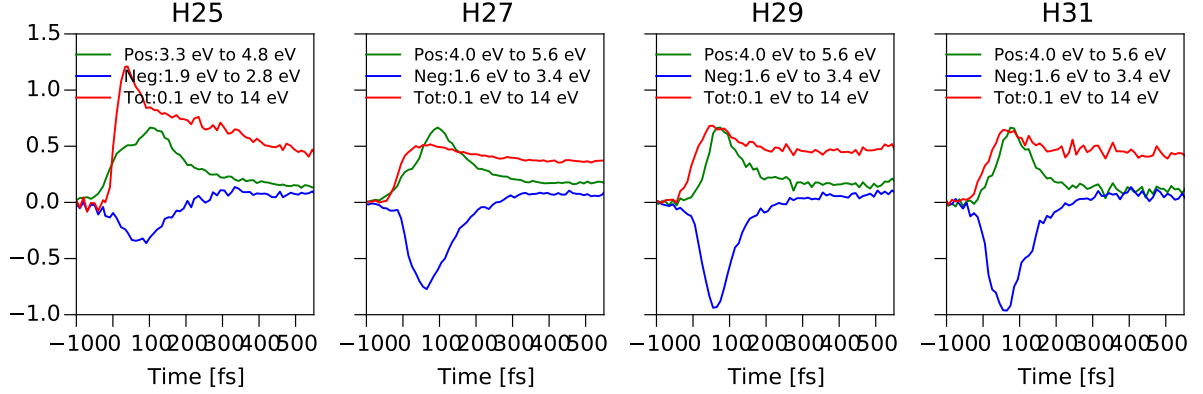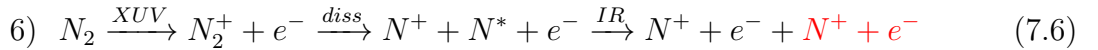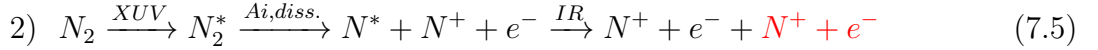
Figure 7.6: Transient signals of the positive (pos) and negative (neg) contributions and the total signal (tot) of the features Q_{25-31}. The transients are obtained by integrating the KER maps in figure 7.4 over the energy ranges of 3.3 eV to 4.8 eV for the positive contribution, 1.9 eV to 2.8eV for the negative contribution and 0.1 eV to 14 eV for the total signal.

leads to the observation of a depletion. We directly can conclude that we are probing dissociative channels, otherwise no depletion region would be observed. Additionally we claim that an IR induced change in the KER for time delays of 500-600 fs can only be induced by a long range interaction potential between the ionic fragments, that is by the Coulomb-potential. The two following channels are possible.

$$2) \quad N_2 \xrightarrow{XUV} N_2^* \xrightarrow{Ai,diss.} N^* + N^+ + e^- \xrightarrow{IR} N^+ + e^- + N^+ + e^- \qquad (7.5)$$

$$6) \quad N_2 \xrightarrow{XUV} N_2^+ + e^- \xrightarrow{diss} N^+ + N^* + e^- \xrightarrow{IR} N^+ + e^- + N^+ + e^- \qquad (7.6)$$

the decay feature Q_{23} has a lower KER of 0.9 eV for long time delays compared to the features Q_{25}-Q_{31} which converges to 2.1 eV, as it is indicated by the solid red and blue lines in figure 7.4. We conclude therefore that feature Q_{23} only appears for H23 and originates from a resonantly excited electronic state, which corresponds to the channel 2. The other features, Q_{25} -Q_{31}, are visible in the maps for several harmonics, and therefore have to originate from a dissociative electronic state of N_2^+, which corresponds to channel 6. The binding energy of the electronic state responsible for the features Q_{25}-Q_{31} has to be between the energy of H23 (35.9 eV) and H25 (39.0 eV). In this energy region the H-band of the N_2^+ is located with a binding energy of about 37 eV. Before we compare our results with the PE curves presented in chapter 2.3 and the new *ab initio* calculations for the H-band we discuss the data using a model of dissociation on a simplified potential energy curve.

7.3.1 Simplified Model of Dissociation

In figure 7.7 a schematic drawing of the model is presented. We approximate the repulsive potential energy curve of N_2^+ by a simple model potential with a "knee"-shape given by
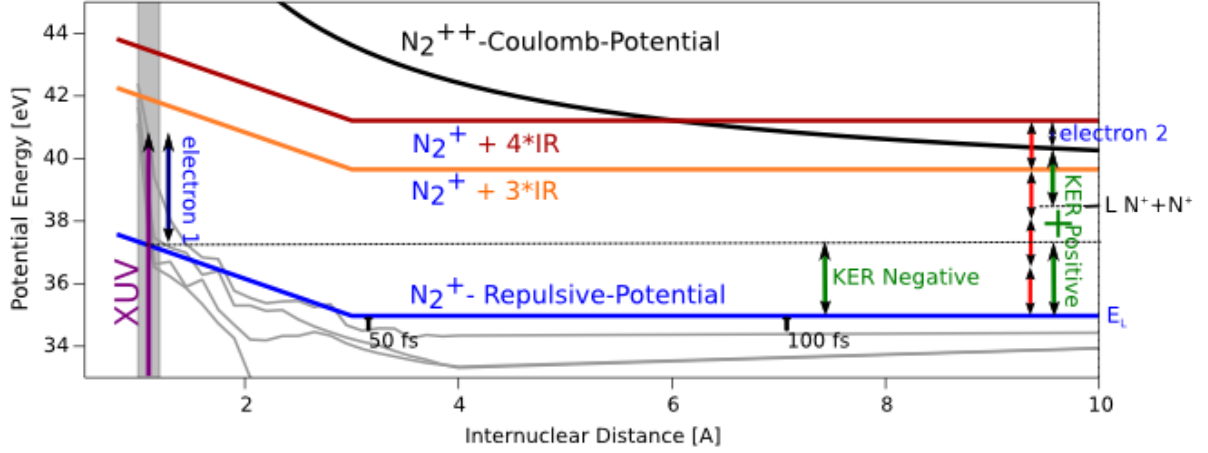
Figure 7.7: The repulsive N_2^+ potential is approximated by the blue curve which consists of two straight sections: one with a negative slope and one with a zero slope. The XUV pulse ionizes the molecule leaving the ion in this excited state, which leads to dissociation. The dissociation is modeled classically. The secondary ionization by the IR pulse is modeled in the multi-photon regime. We include three- or four- IR photon ionization of the dissociating molecule in the model. The possible excitation energy of such a process is indicated as a orange and red line in the figure. When the excitation energy is above the N_2^{++} Coulomb repulsion curve (black line) an ionization via the IR pulse is possible. At this step a second slow electron is created inducing dynamics changes the KER by the repulsion energy. This leads to a negative and positive contribution in the differential KER maps.

$$P(x, E_B, E_L, x_K) = \begin{cases} \frac{E_B - E_L}{x_{FC} - x_K} \cdot (x - x_{FC}) + E_B, & \text{if } x < x_K \\ E_L, & \text{if } x > x_K \end{cases} \qquad (7.7)$$

where E_B is the potential energy in the center of the Franck-Condon region, E_L is the energy of the dissociation limit, x_K is the internuclear distance of the "knee"-edge and x_{FC} is the equilibrium internuclear distance. We separate the dynamics in four successive steps. First the molecule is ionized by an XUV photon. The XUV energy minus the kinetic energy of the removed electron gives the energy of the N_2^+ potential energy curve at equilibrium distance, i.e. in the center of the Franck-Condon region. We then analytically solve the classical equation of motion for the dissociation of the molecule on the repulsive model potential. The solution yields the time dependence of the internuclear distance. In the figure 7.7 the internuclear separation after 50 fs and 100 fs is marked.

The next step in the model is the interaction of the dissociating molecule with the IR pulse. This is challenging, since the IR peak intensity is a few TW/cm^2, where multi-photon transitions are expected but also strong-field effects might play a role. From figure 7.7 we can deduce that the ionization potential at an internuclear distance of about 4 Å to

5 Å is 6 eV. The pondermotive potential of an electron in the IR field is about 0.2 eV, together with the ionization potential this results in a Keldysh parameter [60] of

$$\gamma = \sqrt{\frac{I_P}{2U_p}} = 3.8 \tag{7.8}$$

Since the Keldysh parameter is larger than one, this supports the choice of treating the ionization by the IR pulse in the multi-photon regime for long delays. In the figure two lines indicate the energy that can be reached by three-photon and four-photon ionization. At an internuclear distance of 6 Å the four-photon curve is above the repulsive $N^+ + N^+$ Coulomb-potential, and the dissociating molecule can be doubly ionized. At an internuclear distance of of about 13 Å also three-photon ionization becomes possible (outside the plot range in figure 7.7). Both three- and four-photon ionization lead to a second electron with a kinetic energy depending on the internuclear distance. In the KER spectrum double ionization results in two charged N^+ fragments, that further repel each other. The final KER is the sum of the KER the fragments already have before the interaction with the IR and the additional energy after double ionization accumulated due to Coulomb repulsion. This results in a depletion in the KER spectrum at the kinetic energy acquired by molecules that are not further excited by the IR

$$KER_- = E_B - E_L \tag{7.9}$$

The positive contribution in the KER originating from double ionization is given by

$$KER_+ = E_C(x) - L_{N^+ + N^+} + KER_- \tag{7.10}$$

and should have twice the total counts compared to the depletion. In the following sections we describe how we chose the parameters of the model to fit to the features Q_{23-31} in the ion map in figure 7.4 and the features Q_{27-31} in the electrons map in the figure 7.5.

Initial Binding Energy and Dissociation Limit

The parameters of the model potential are manually chosen to reproduce the shape of the features Q_{23} to Q_{31} in the KER maps and the feature Q_{27} to Q_{31} in the electron maps. We can demonstrate that the shape of the features Q_{23} to Q_{31} is sensitive to the values of E_B and E_L. In figure 7.8 and 7.9 the model potential, the KER map for H31 and the electron map for H31 are presented. In figure 7.8 the parameter E_B is varied and in figure 7.9 the parameter E_L, while the gap is $E_B - E_L$ is kept constant. Figure 7.8a shows the model potentials with varying parameters in orange. The grey curves are the output of the new *ab initio* calculations, presented in section 2.3. The inset shows the energy E_B with the static photoelectron spectrum in the energy region of the H-band, which was discussed in
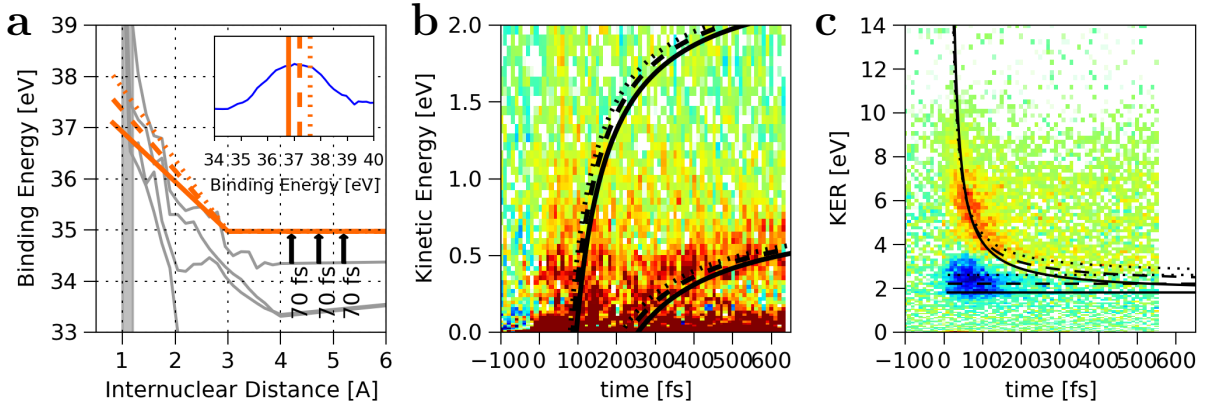
Figure 7.8: a: Different model potentials with different E_B set to 36.78 eV, 37.2 eV and 37.58 eV. x_K is fixed to 3 Å and E_L to L11 (34.97eV). **b** and **c:** Corresponding simulation output for the three different PE and H31. In the electron map the three and four-photon contributions are indicated while for the KER map double ionization at any time-delay is assumed to be possible. We can see that the KER depletion signal is sensitive to the initial binding energy of the state.

chapter 6. In the electron maps in figure 7.8b and the KER maps in figure 7.8c the output of the simulation for the different model potentials is plotted. In the electron map we distinguish between the contribution from three-photon double ionization and four-photon double ionization. In the KER map the induced changes in the KER are plotted starting from time-zero, i.e we assume that the molecule can be double ionized by IR at any time-delay and the IR ionization mechanism does not influence the KER. We will comment later on the shortcomings of the multi-photon picture that do not explain the ionization mechanism by the IR pulse for small time-delays.

In figure 7.8 the binding energy E_B is varied in steps of 0.4 eV around 37.2 eV. The center energy of 37.2 eV corresponds to the peak of the H-band in the photoelectron spectrum and also nicely reproduces the convergence of KER feature for long time delays to about 2.21 eV if E_L is fixed to L11 (34.97 eV) and x_K to 3 Å. We see that the position of the depletion in the KER map is very sensitive to the binding energy of the state we are probing and we claim that we hereby have an uncertainty in the initial binding energy of the electron of no more than 0.5 eV.

In figure 7.9 E_L is set to the limits L10 (34.629 eV) and L11 (34.973 eV) and E_B is set such that the gap between E_B and E_L is 2.21 eV, corresponding to limit of the features Q_{25-31} for long time-delays. x_K is fixed to 3Å. We can see that only the potential connected to L11 reproduces the three-photon contribution in the electron signal. Other dissociation limits (e.g. L9 or L12) do not reproduce the data at all.

The simulation output for four photon IR double ionization does not have a clear corresponding feature in the electron maps. There are electrons created by the IR for short time delays. However this feature is diffuse in shape and it is not clear which ionization mechanism leads to these electrons. For the determination of the model potential param-
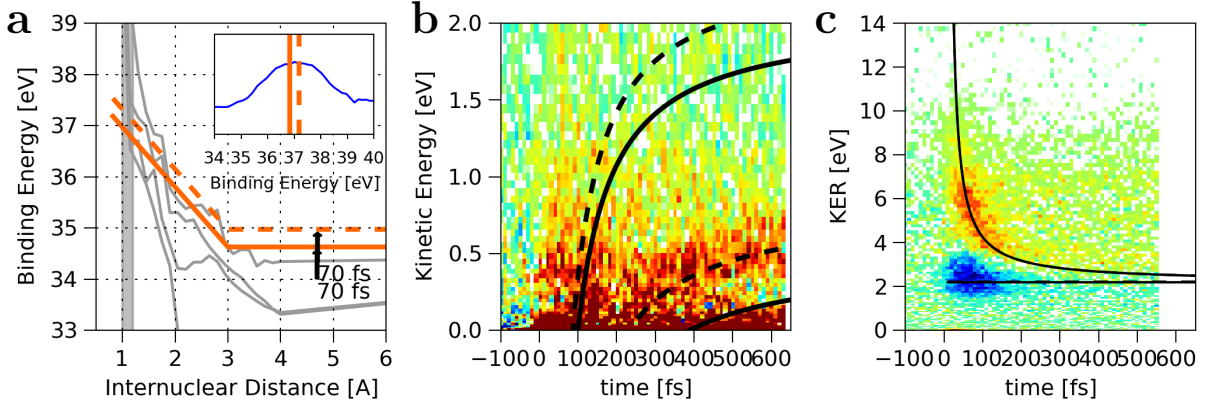
Figure 7.9: a: Model potentials with different E_L set to L10 (34.63 eV) and L11 (34.97 eV). The gap between E_B and E_L is kept fixed at 2.21 eV and x_K is fixed to 3 Å. **b** and **c**: Corresponding simulation output for harmonic H31. In the electron map the three and four photon contribution are indicated while for the KER map double ionization at any time-delay is assumed to be possible. We can see that the electron kinetic energy and the onset of the three photon contribution in the electron map is sensitive to E_L and is in agreement with L11 (dashed line). The KER simulation is the same for the two model potentials, because it is only sensitive to the difference between the E_B and E_L, which we keep constant here.

eters we thus assume the three-photon ionization dominating the long-time dynamics and rely solely on this feature. In the KER maps the different limits (reminder: E_B and E_L are fixed) also result in a slightly different simulation output, however the lines are so close together that they can not be distinguished in the plot.

We conclude that via the analysis of the electron and ion data we can determine the parameters E_B (37.2 eV) and E_L (L11, 34.97 eV) with high accuracy. The binding energy hereby is determined with an energy resolution below 0.5 eV. The resolution is sufficient to clearly identify the limit L11 as the only limit that can explain the data. We will now continue with the question, if we can actually resolve the shape of the N_2^+ repulsive model potential.

Potential Energy Curve Shape

The last free parameter of the model potential is the internuclear distance of the "knee" position x_K. In figure 7.10 the simulation for different knee positions is presented. x_K is set to 1.5 Å, 3 Å and 5 Å. E_B is fixed to 37.2 eV and E_L to L11 (34.97 eV). The position of x_K determines the acceleration of the ionic fragments, but does not influence the final KER. This is indicated in figure 7.10a by the different internuclear separations after 60 fs for the three model potentials presented in the figure. In the electron map (b) and the KER map (c) the variation of the simulation output are only minor in comparison to the temporal and spectral width of the features. However x_K=3 Å definitely gives the best fit
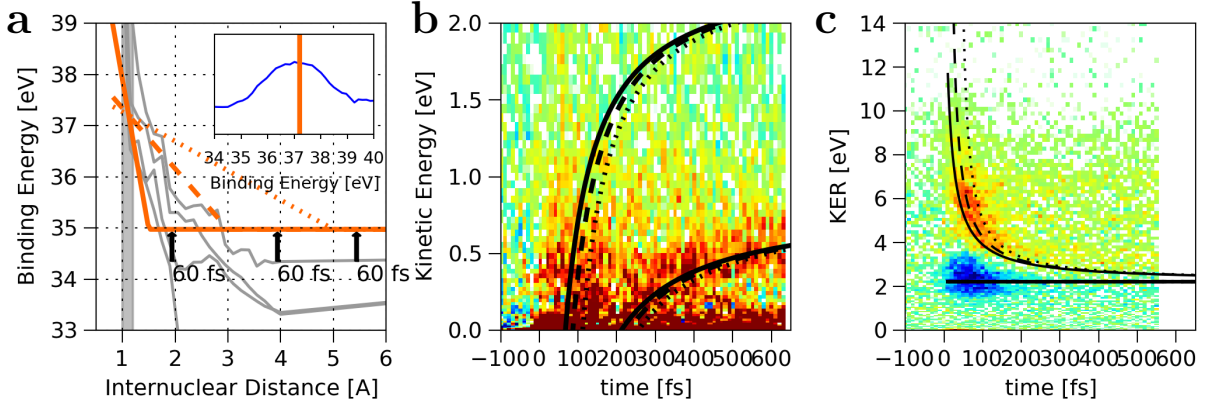
Figure 7.10: a: Model potential energy curved with x_K set to 1.5 Å, 3.0 Å and 5.0 Å. E_B is fixed to 37.2 eV and E_L is fixed to L11 (34.94 eV). **b** and **c:** Corresponding simulation output for harmonic H31. In the electron map the three and four photon contribution are indicated while for the KER map double ionization at any time-delay is assumed to be possible. We can see an influence of the initial slope of the model potential onto the agreement between the simulation and the KER spectrum and fix x_K to 3 Å.

to feature in the KER map.

In the case of feature Q_{23} we cannot observe a signal in electron maps comparable to the features Q_{27} to Q_{31} for the higher XUV energies. However we directly can set E_B equal to the XUV energy (35.9 eV), since we conclude that it is a resonance we are exciting. With the knowledge of the binding energy it is possible to deduce the model potential parameters solely from the KER maps, in complete analogy to the group of features Q_{25} to Q_{31}. In the table 7.1 the results for the model potentials are summarized.

Feature	Type	E_B	E_L	x_K
Q_{23}	Resonant	35.9	L11	3.0
Q_{25}-Q_{31}	Direct ionization	37.2	L11	3.0

Table 7.1: Parameters of model potential for features Q_{23} to Q_{31}

7.3.2 Comparison with Theory

For the features Q_{25-31} we can compare the obtained model potential with the results of the new *ab initio* calculations for the Σ_g states of the N_2^+ manifold. In figure 7.11 both the model potential energy curve and the curves already introduced in section 2.3 are plotted. Table 7.2 lists the potential energies of the states 9-12 for equilibrium internuclear distance, the adiabatic dissociation limits for these states and the $2\sigma_g^{-1}$ hole densities.

First of all it has to be emphasized that the *ab initio* calculations do not reproduce the dissociation limits. The DRMG method is not automatically size consistent, i.e. it does not

Kornilov/Ritze				
$n\Sigma_g$	n=10	n=11	n=12	n=13
E_B [eV]	37.0	37.7	38.2	40.3
E_L	L9	L10	L10	L11
$2\sigma_g^{-1}$	0.01	0.09	0.42	0.02

Table 7.2: Parameters of Σ_g states at the equilibrium internuclear distance.
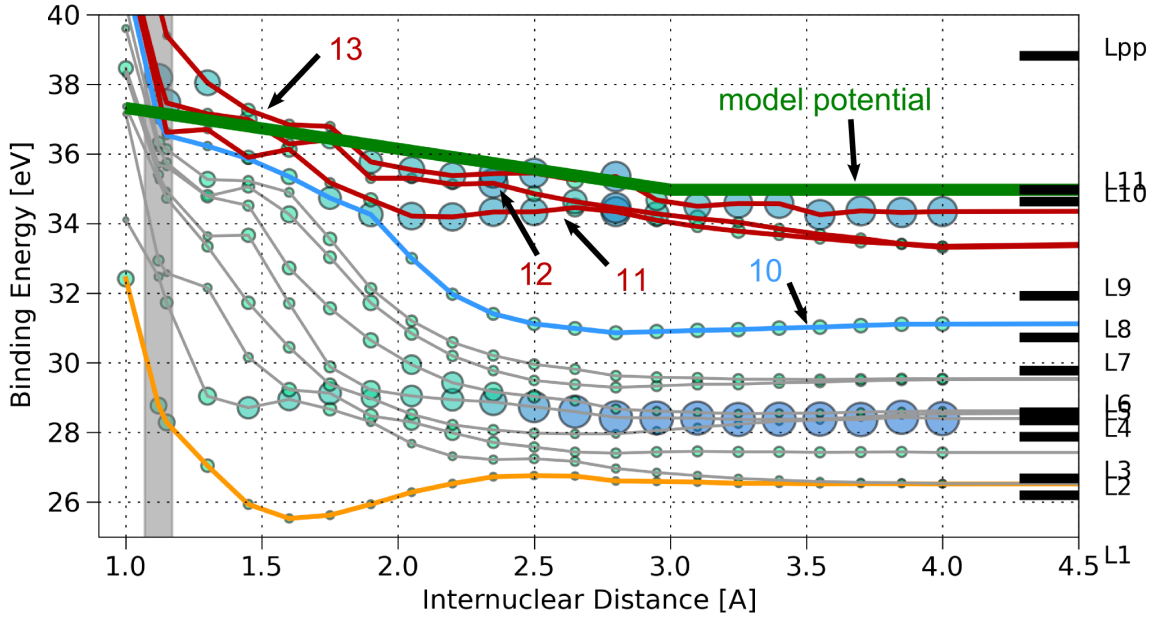

Figure 7.11: Comparison between the model potential explaining the features Q_{25}-Q_{31} and the new *ab-intio* results for the Σ_g states presented in section 2.3.

reproduce correctly the atomic states when the N atoms are far apart. The limits of the curves however are correctly assigned. From the simulation we conclude that we observe a state with binding energy around 37.2 eV with a precision of about 0.5 eV. This would either correspond to the state 10, 11 or maybe even 12, since the *ab initio* calculations still might be improved resulting in lower binding energies in the Franck-Condon region.

In the previous chapter 6, dealing with the spectroscopic interpretation of the static spectra, we concluded that the major dissociation channel contributing to the H-band is connected to the L9 limit and can be either described by ionization into state 10 followed by adiabatic dissociation, or more likely by ionization into one of the states 11 or 12 with a larger $2\sigma_g^{-1}$ hole density. The states 11 and 12 are connected to L10 limit. However it is also possible that an excitation of these states leads to non-adiabatic dissociation towards the L9 limit and hence could also explain the findings presented in the chapter 6.

In case of the features Q_{25-31} in the KER maps we concluded from the parametric model

that we only probe molecules dissociating towards the L11 threshold. The major channel going to L9 would require 2 additional IR photons, in total 5, to be doubly ionized and would result in a depletion around 5.5 eV to 6 eV, at the position of the peak of the H-band in the static KER spectrum. This is not observed in the time-resolved KER maps. We therefore are probing a minor dissociation channel of the H-band, that dissociates towards the L11 threshold. Interestingly we can see that the large $2\sigma_g^{-1}$ hole density o 12 in the FC region is transferred to states 11 and 13 at internuclear distances between 2 Å and 2.5 Å and finally ends up in state 13 for large internuclear distances, see figure 7.11. This might suggest a strong non-adiabatic coupling between the curves. Additionally we also observe that the manual fit of x_K to the KER spectra reproduces the slope of the states 11-13 and backs up our statement that we can resolve the shape of the N_2^+ potential in the time-resolved maps. However only the general trend of the potential energy curves is reproduced by the simple model. The details of the shape and especially the dynamics of the $2\sigma_g^{-1}$ hole in the region from 2 Å to 4 Å cannot be explored with the current time resolution.

In case of feature Q_{23}, theoretical *ab initio* modelling of a neutral resonance in this energy region is more challenging than for the direct ionization channels, because neutral autoionizing states with excitation energies of 35 eV have to be considered. We are not aware of any theoretical calculations for such highly excite states.

7.3.3 Monte Carlo Simulation of the Dissociation Dynamics

So far we only discussed the general trend of the features Q_{25} to Q_{31} in the KER and the corresponding features in the electron maps. In order to compare also the shape of the features with our model we simulate the different contributions of the three and four photon double ionization with a simple Monte-Carlo simulation. In figure 7.12 the three photon and four photon contributions in the KER and electron map are presented. The electron map and ion map for H29 are also presented for comparison with the simulation. For the simulation we make the following assumptions. The result is independent of the XUV energy, only the energy of the excited ionic state is relevant. The ground state internuclear separation has a Gaussian distribution around the center of the FC region with a width of 0.94 Å(FWHM-width of the Gaussian shaped vibrational ground state, assuming a harmonic potential). The time resolution is set to 48 fs (FWHM), and the spectral width of the IR pulse is 0.15 eV, which corresponds to a pulse duration of the IR of 30 fs (FWHM), in case of a bandwidth limited pulse. We assume that the probability for a three- or four-photon process is equal.

The features Q_{27} to Q_{31} in the electron maps are rather nicely reproduced by the model for three-photon ionization. The spectral width in the simulation and in the data for longer time delays in both cases is about 0.2 eV. The four-photon contribution in the simulation has no corresponding part in the electron data. We rather observe the diffuse electron feature labeled W_{27} to W_{31} in the electron maps. We conclude, that the observed ionization mechanism for short time delays is not correctly described in the multi-photon picture we employ. A detailed discussion of the possible underlying mechanisms is beyond
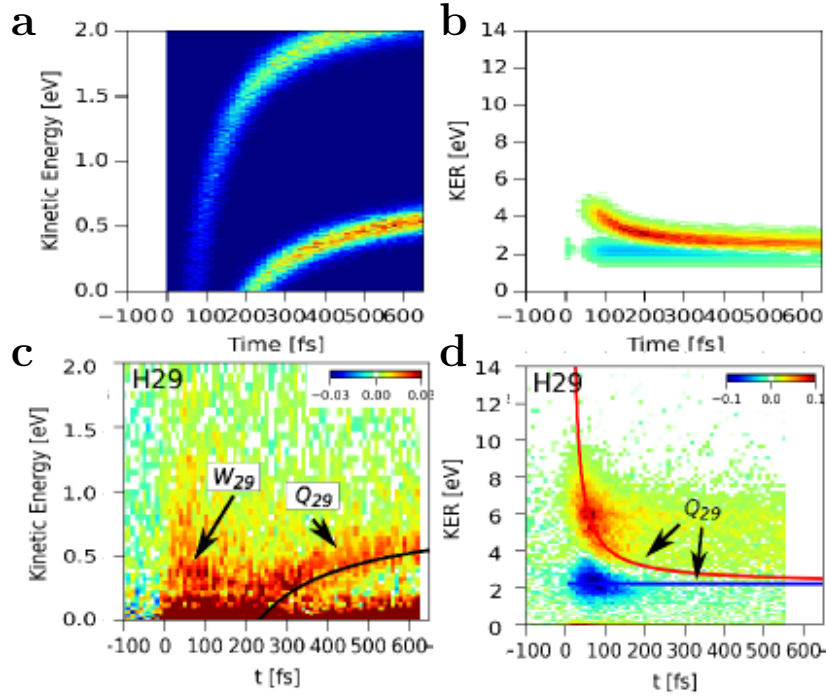
Figure 7.12: Monte-Carlo Simulation for the model described in figure 7.7 and the PE parameters in table 7.1. **a:** Electron data with three and four photon ionization. **b:** KER simulation four- and three-photon double ionization. **c:** Electron map for H29 (45.2 eV). **d:** KER ion map for H29 (45.2 eV).

the scope of this thesis.

In case of the KER maps the positions of the features Q_{25-31} are nicely reproduced, but the observed spectral shape of the features also strongly differs from the simulation. In figure 7.13a and 7.13b KER spectra integrated for different time delays are presented. With an increasing XUV energy the positive contribution gets broader both for short(40-60 fs) and long (400-500 fs) time delays, while the width of the negative part stays rather constant. Such XUV-dependent changes are not observed in our Monte Carlo simulations in figure 7.12. The ratio between positive and negative signals is rather constant in time and we therefore can conclude that probability of doubly ionizing the dissociating fragments with the IR pulse is constant with time and internuclear distance. This is surprising and not explained by our simple model. The reason for the discrepancy in the spectral shape remains unclear.

7.4 Features T_{21}, T_{23} and T_{25} - Neutral Dissociation

The ion features T_{21}, T_{23} and T_{25} in figure 7.14 (replot of the figures 7.4 and 7.5) appear at time zero and their signal remains constant in energy for all positive delays. Also no
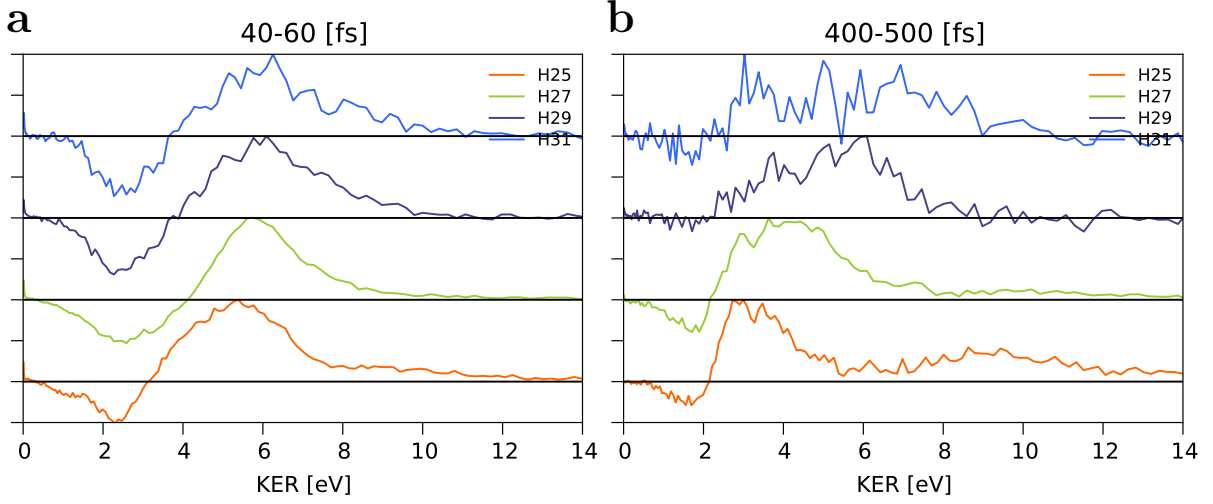
Figure 7.13: KER spectra integrated over different time-delay spans. **a:** Integration for the time span 40 fs to 60 fs. **b:** Integration for the time span 400 fs to 500 fs.
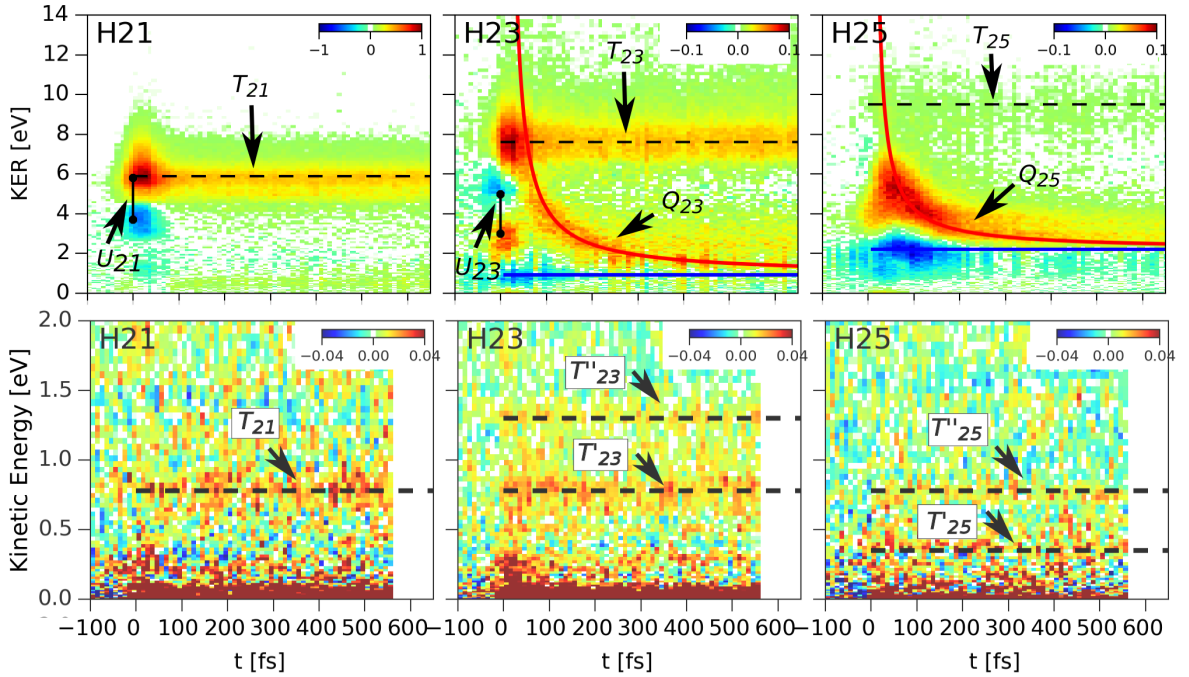

Figure 7.14: These are the same electron and ion maps for H21-H25 that are also presented in figure 7.4 and figure 7.5 that are presented here again for convenience. The features T_{21}, T_{23} and T_{25} have a constant energy which does not change with pump-probe delay. The features U_{21} and U_{23} in H21 and H23 only appear during the pump-probe overlap in the ion maps.

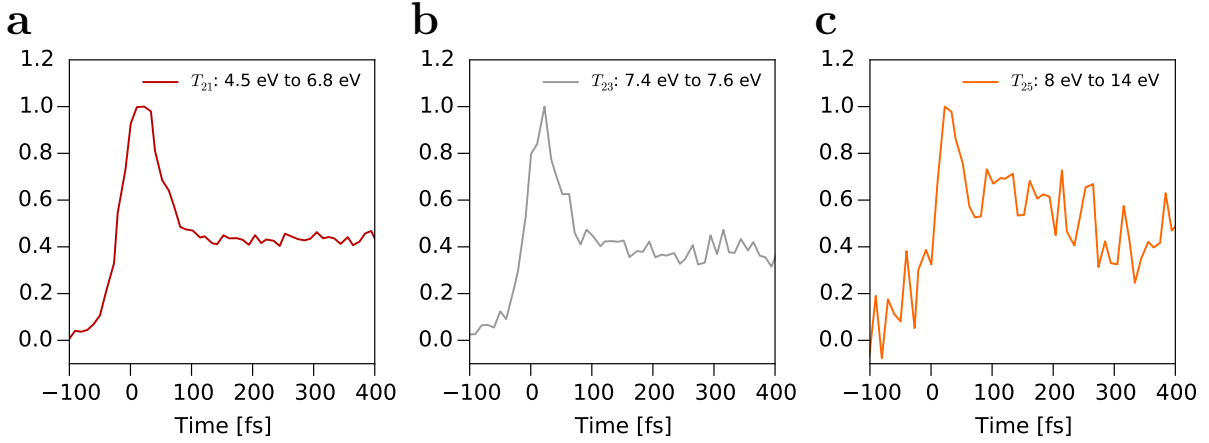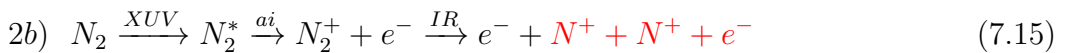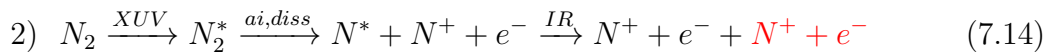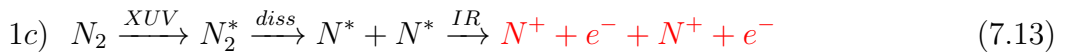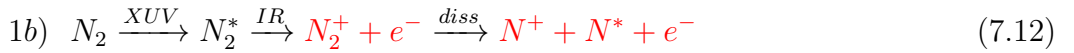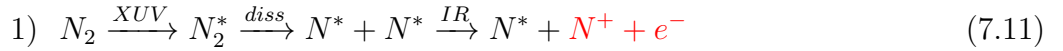**Figure 7.15:** Transient signals of features T_{21}, T_{23} and T_{25} extracted from the ion KER maps of harmonics H21, H23, H25 in figure 7.4 by integrating over the energy ranges of 4.5 eV to 6.8 eV for T_{21}, 7.4 eV to 7.6 eV for T_{23} and 8 eV to 14 eV for T_{25}.

decay of the signal amplitude can be observed for long time delays (>100 fs) after the pump-probe overlap. In figure 7.15 time dependent signals for these three ion features are presented. For the feature T_{25} one can see a small decay, but the signal is noisy and the normalization procedure is not as reliable as for the other harmonics. Therefore we conclude that all three features have no appreciable decay in amplitude for the time delays time recorded in the experiment. There is a slight enhancement of the signal for all three features around pump probe overlap that can be attributed to different reasons: In case of T_{21} it is due to the overlap of this feature with the positive part of feature U_{21}, that will be discussed in detail in section 7.5. In case of feature T_{23} and T_{25} the enhancement for short delays is due to overlap with the feature Q_{23} and Q_{25}. We neglect these variations at short delays and concentrate the discussion on the spectral position and shape of the features at longer delays (>100 fs).

Following the general arguments given in the section 7.2 one can make the following claim: The features appear only for individual harmonics. This limits the possible dissociation channels to resonantly excited neutral states. In the following the possible neutral dissociation pathways that lead to additional N^+ fragments induced by the IR pulse are listed again.

$$1) \quad N_2 \xrightarrow{XUV} N_2^* \xrightarrow{diss} N^* + N^* \xrightarrow{IR} N^* + N^+ + e^- \tag{7.11}$$

$$1b) \quad N_2 \xrightarrow{XUV} N_2^* \xrightarrow{IR} N_2^+ + e^- \xrightarrow{diss} N^+ + N^* + e^- \tag{7.12}$$

$$1c) \quad N_2 \xrightarrow{XUV} N_2^* \xrightarrow{diss} N^* + N^* \xrightarrow{IR} N^+ + e^- + N^+ + e^- \tag{7.13}$$

$$2) \quad N_2 \xrightarrow{XUV} N_2^* \xrightarrow{ai,diss} N^* + N^+ + e^- \xrightarrow{IR} N^+ + e^- + N^+ + e^- \tag{7.14}$$

$$2b) \quad N_2 \xrightarrow{XUV} N_2^* \xrightarrow{ai} N_2^+ + e^- \xrightarrow{IR} e^- + N^+ + N^+ + e^- \tag{7.15}$$

A few of these channels can directly be ruled out. Channel 2b can be ruled out: An IR

induced Coulomb explosion induced at equilibrium internuclear distance would result in a KER of 13.2 eV [58], which is higher than the KER of the observed features. Channel 2 can also be ruled out: The Coulomb explosion induced by the IR would change the KER of the ionic N^+ fragment, since the repulsive Coulomb potential is long-range and the fragments can not be too far apart to not feel the potential within the observed time span. We can not observe a depletion in the map corresponding to the feature T_{21-25} and therefore channel 2 can also be ruled out. For channel 1c the similar argument can be applied. If the IR would create two charged N^+ fragments the KER would be changed within the observed time-span due to the long-range repulsive Coulomb potential.

We therefore limit the possibilities to channels 1 and 1b. Either the IR ionizes a highly excited but bound neutral state that then dissociates or the highly excited state dissociates and the IR ionizes one of the atomic fragments. These two possibilities are difficult to distinguish. Theoretical *ab initio* modeling of neutral states in this energy region is extremely difficult due to the high excitation in the system and the strong electron-electron correlations. Both, bound or repulsive potential energy curves are possible in the energy region of 32.8 eV (H21) to 39.0 eV (H25). To distinguish possible dissociation channels we will present an interpretation that is based on combined interpretation of the features T_{21-25} in the ion and electrons maps.

We first discuss the features T_{21}, T'_{23} and T''_{23} in the electron maps of harmonic H21 and H23, presented in figure 7.14. We observe electrons with a kinetic energy of 0.75 eV labeled as feature T_{21} and T'_{23}. For H23 there are also electrons with kinetic energy close to 1.4 eV observable, labeled as feature T''_{23} . If we assume that these electrons originate from the ionization of a the neutral atoms in the channel 1 by a single IR photon, the kinetic energy of the emitted electron is given by:

$$E_{kin,el} = E_N + E_{Photon} - E_{N^+} \tag{7.16}$$

where E_N is the energy of the neutral state atomic nitrogen, E_{Photon} is the energy of the photon and E_{N^+} is the energy of the ionic state. The photon energy of the IR pulse is 1.57 eV and we assume that the atom is always in the ionic ground state after ionization with an energy of 14.53 eV (given with respect to the neutral ground state). We can find two excited states of the neutral N atom that can explain the observed kinetic energies of the features T_{21}, T'_{23} and T''_{23} in the electron maps for H21 and H23 shown in figure 7.14. The states are the $N \, 2s^2 2p^2(^1D)3p \, ^2D^o$ state with 13.70 eV and the $2s^2 2p^2(^1S)3s \, ^2S$ state with 14.42 eV, see also table 2.1. For convenience we label the $^2D^o$ state S6 and the ^2S state S7. For the S6 state electrons with 0.74 eV kinetic energy (feature T_{21} and T'_{23}) would be expected and, for the S7 (feature T''_{23}) state electrons with 1.46 eV kinetic energy. Close to the ionization limit there are certainly many more states, but all of them have higher main principle quantum numbers than 3 and therefore probably a smaller excitation probability.

The observations for H21 and H23 favour the conclusion that the IR is probing dissociation labeled as channel 1. In this case the initial neutral bound state would directly

dissociate towards one of the neutral dissociative limits. The time scale of the dissociation is expected to be fast (femtoseconds), since the range of the repulsive potential between the two neutral atoms is quite short, i.e. only about 2 Å, which is twice the size of the neutral atom. The IR is then ionizing one of the neutral atoms without any impact on the kinetic energy of the ionic fragments.

The expected KER of the ionized neutral atom is the difference between the initial excitation energy of the neutral molecule, that we, for now, assume to be exactly equal to the XUV energy for the individual harmonic, and the final dissociation limit of the neutral manifold.

$$E_{KER} = E_{XUV} - L_{N_2} \tag{7.17}$$

We can calculate the dissociation limits of the neutral states in the same manner as for the N_2^+ manifold by:

$$L_{N_2} = E_{N_2} + E_{N^*} + E_{N^*} \tag{7.18}$$

with $E_{N_2} = 9.79\ eV$ the dissociation energy of the neutral molecule in the ground state and E_{N^*} the excitation energy of the electronic state of the neutral atom. For the relevant combination of electronic states from table 2.1, the limits are listed in the table 7.3.

Label	S1	S2	S3	S4	S5	S6	S7
Configuration	$^4S^o$	$^2D^o$	$^2P^o$	^4P	^4P	$^2D^o$	^2S
Valence Electron	$2s^22p^3$	$2s^22p^3$	$2s^22p^3$	$2s^22p^33s$	$2s2p^4$	$2s^22p^33p$	$2s^22p^33s$
Energy [eV]	0	2.38	3.58	10.33	10.92	13.70	14.42
Limit with S4 [eV]	20.12	22.5	23.7	30.45	31.04	33.82	34.54
Limit with S5 [eV]	20.71	23.09	24.29	31.04	31.63	34.41	35.03
Limit with S6 [eV]	23.49	25.87	27.07	33.82	34.41	37.19	37.91
Limit with S7 [eV]	24.21	26.59	27.79	34.54	35.13	37.91	38.63

Table 7.3: Dissociation limits of the neutral N_2 manifold. The limits are given only for excited neutral states that are in agreement with the time-resolved electron data.

The KER spectrum corresponding to the features T_{21} and T_{23} is presented in figure 7.16a and 7.16b. The spectra are integrated over a range of time delays from 400 fs to 500 fs. The shapes of the peaks at 5.8 eV for the feature T_{21} and 7.7 eV for the feature T_{23} are well visible. The energy of the calculated KER, deduced from table 7.3, is marked by blue lines. Only the combinations of neutral states that yield the expected KER close to the observed KER are marked, other combinations are too far off. For H21 and feature T_{21} we have four combinations of excited states that might explain the KER. Feature T_{21} in the electron map might correspond to electrons coming from single photon ionization of the neutral S6 state. Since we can not observe electrons with a kinetic energy of 1.46 eV, the channels including an atom in the S7 state can be ruled out, and dissociation to one
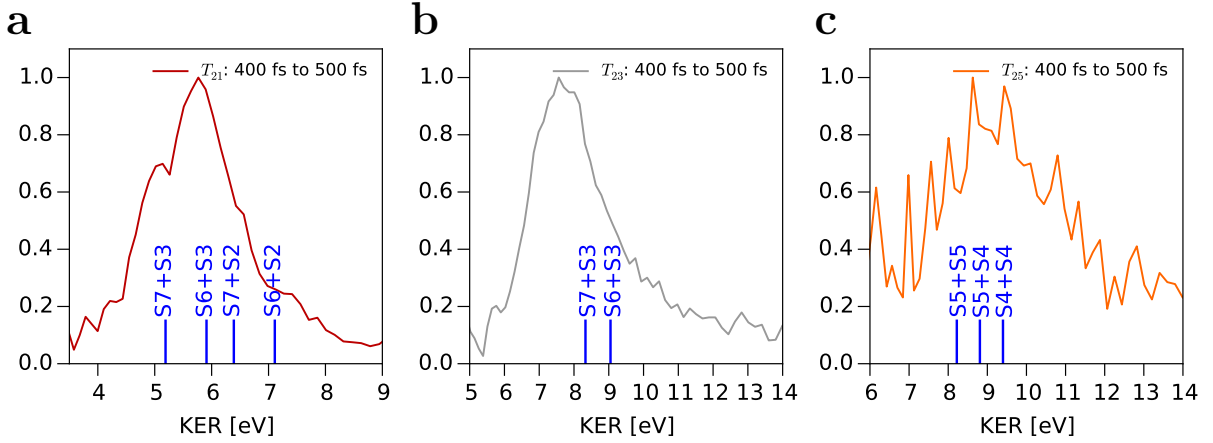
Figure 7.16: KER spectra at long time delays showing the shape of the features T_{21-25} in H21, H23 and H25. Blue lines indicate KER of dissociation towards limits of the $N^* + N^*$ manifold. The energies of the limits are given in table 7.3

of the limits S6+S3 or S6+S2 remain as possibilities. The KER of a dissociation towards the S6+S3 limit coincides well with the maximum of the observed KER.

For feature T_{23} only combinations of the states S6 and S7 with S3 are able to explain the observed KER, although the energetic position of the measured KER maximum is off by more than 0.5 eV from the calculated KER. The binding energy of the resonantly excited state however does not need to be exactly equal to the center energy of the XUV spectrum, but can be within the spectral bandwidth of the XUV pulse, that is about 0.5 eV, which might explain the mismatch. Electrons originating from ionization with a single IR photon of the S6 and S7 state can both be observed in the corresponding electron map, labeled as T'_{23} and T''_{23}. We conclude that dissociation to both limits is observed.

In case of feature T_{25} in the H25 ion map of figure 7.14 the situation is more complicated. We have to include two more electronic states of the neutral atom into the discussion, the $2s^2 2p^2 3s \; ^4P$ (S4) state with an energy of 10.33 eV and the $2s 2p^4 \; ^4P \; ^4P$ (S5) state with and energy of 10.92 eV. Only these two states result in dissociation limits that correspond to a KER in the energy region between 8 eV and 10 eV as can be seen in figure 7.16. However these states can not be ionized via the absorption of a single IR photon. In case of three photon ionization of these states electrons with a kinetic energy of 0.51 eV and 1.1 eV are emitted. However electrons with these kinetic energies can not be observed. This disagreement can not be explained so far.

To summarize, we attribute the features T_{21}, T_{23} and T_{25} to resonantly excited neutral states, since the features only appear for individual XUV energies. We furthermore conclude that the states do not autoionize, since we do not see any depletion in the KER maps and also cannot observe any time-dependent changes in the KER maps that would arise from a Coulomb explosion. We assume that the highly excited neutral states are dissociative and the IR pulse is ionizing highly excited neutral atomic fragments after the atoms are already too far apart to feel their $N^+ + N^*$ interaction potential. The features observed
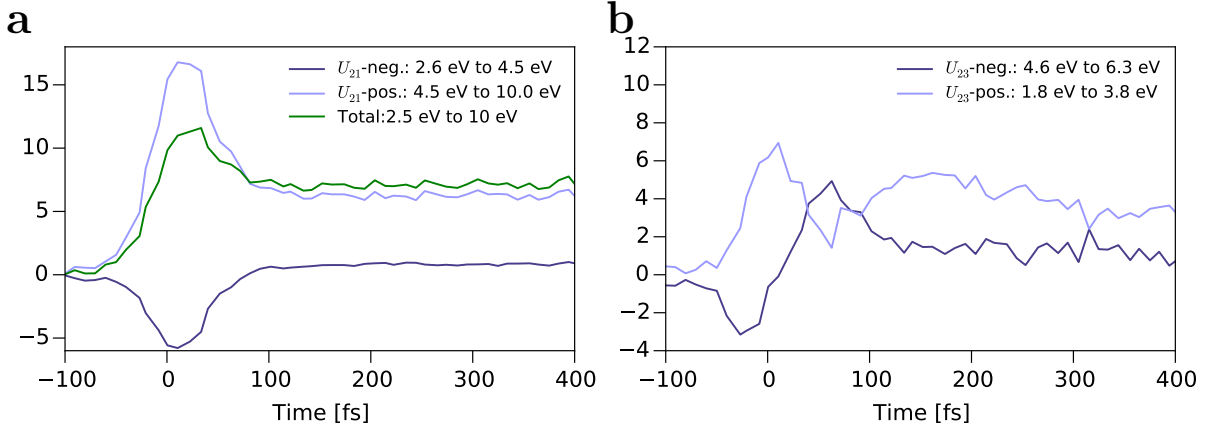
Figure 7.17: Transient signals of features U_{21} and U_{23} extracted from the ion KER maps of harmonics H21 and H23 in figure 7.14.

in the electron maps support the assumption that we are ionizing separated atoms and in fact we can reasonably well predict the final KER by taking into account only atomic states that correspond to the electron maps, for features T_{21} and T_{23}.

7.5 U_{21} and U_{23} - Autoionization

The features U_{21} and U_{23} are observed in the KER maps of H21 and H23, see figure 7.14. For time-delays around time zero the IR pulse is changing the energy of the N^+ fragments. The feature U_{21} indicates a change in the KER of N^+ fragments from about 4 eV to about 6 eV. The positive contribution is overlapping with the feature T_{21}. From the fact that we observe a depletion in the map and we only see the feature in the map of H21 we deduce that the initially excited neutral state creates N^+ fragments via dissociative autoionization and the IR is therefore probing the autoionizing resonance. We can estimate the ratio of the amplitudes of positive to negative contributions by comparing transients for different energy regions in the ion map in figure 7.14. The transients for the positive and negative contribution and the sum of both are presented in figure 7.17a. The signal at t>100 fs corresponds to the feature T_{21} discussed above. We assume that it remains constant also in the region dominated by the feature U_{21}. Therefore for the positive contribution of the feature U_{21} we need to consider the signal, which rises above the level of the feature T_{21}. We can observe that the positive contribution is bigger than the negative one, though it is less than twice the negative one, which would suggest double ionization as the only channel. We therefore have two possible scenarios for this autoionization process, which both can contribute to the signal: Either the IR pulse creates additional N^+ fragments and we observe the channel:

$$2) \quad N_2 \xrightarrow{XUV} N_2^* \xrightarrow{ai,diss} N^* + N^+ + e^- \xrightarrow{IR} N^+ + e^- + \textcolor{red}{N^+ + e^-} \tag{7.19}$$
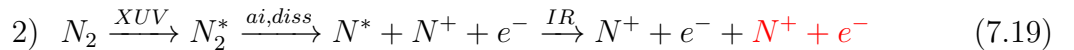
or could also be possible that to the positive contribution arises from the channel:

$$2b) \quad N_2 \xrightarrow{XUV} N_2^* \xrightarrow{ai} N_2^+ + e^- \xrightarrow{IR} e^- + N^+ + N^+ + e^- \tag{7.20}$$
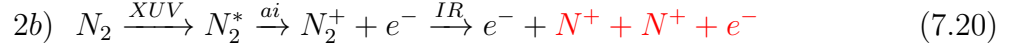
although this channel should result in a rather high KER (up to 13.2 eV) since the Coulomb explosion is started at the equilibrium internuclear distance. We do not observe such a high KER in the map of harmonic 21 and therefore find this channel improbable. In the figure 7.17a we observe that the maximum of both the positive and negative contribution is at about 15 fs after time zero and can conclude that the dissociation dynamics are very fast, on the time-scales of the time-resolution and the channels can only be probed by the IR for small internuclear distances close to the equilibrium internuclear distance.

The feature U_{23} is observed in the ion map for H23. This time the depletion is at higher energies around 5.3 eV and a positive signal at lower energies around 2.3 eV. In the ion KER map we can see that the depletion signal is overlapped by features T_{23} and Q_{23} simultaneously. We estimate the ratio between positive and negative contributions in the KER spectrum at small negative pulse delays within the pump-probe overlap in order to minimize the contributions of T_{23} and Q_{23}. The feature U_{23} therefore consists of an IR induced change of KER to lower energies, where the positive and negative contributions have roughly the same amplitude. This leads to the conclusion, that the IR pulse is probing a dissociative autoionizing resonance, but this time the IR pulse is not ionizing the dissociating fragments, but is rather coupling the dissociation dynamics to a dissociation limit that is higher in energy than the original limit reached by pure XUV ionization. It is thus reducing the KER of the dissociation.

In summary we observe dissociative autoionizing resonances close to time-zero in the KER maps of harmonic H21 and H23. This we can deduce from the facts, that we observe depletions in the maps and only observe the features U_{21} and U_{23} for the individual XUV energies.

7.6 Summary

We recorded time-resolved pump-probe XUV+IR N^+ ion KER spectra and electron spectra with XUV pulses with center energies in the range from 32.8 eV to 48.4 eV and a moderately strong IR pulse with peak intensities of a few TW/cm^2. The comparison of the maps for different XUV energies enables us to identify different dissociation channels of N_2^+ that are either resonant to the XUV photon energy or proceed via direct ionization. We conclude that in the energy range between 32.8 eV and 39 eV we probe both resonantly excited neurally dissociating states and resonantly excited autoionizing states with the IR pulse. In this binding energy range it is hard to make statements about the electronic configuration of the initially excited neutral states, due to the high excitation in the system. For XUV energies from the threshold of 37 eV on we are probing a minor branch of the dissociation via the H-band of the N_2^+ manifold with the IR pulse. We are able to model the general trend of this feature by a classical trajectory calculation and can compare the result with

the new *ab initio* calculations that were performed to describe the potential energy curves of the H-band. We claim that the presented experiments have a higher accuracy than the present theoretical description of the dissociation process. However the model we apply to describe the data can not explain all the observed dynamics. The ionization mechanism for short pump probe time delays remains unclear and additionally the KER spectra exhibit an XUV energy dependence for long time delays that is not reproduced by the present model.

8 Autoionization dynamics in N_2 Close to the Ionization Threshold of the $B^2\Sigma_u^+$ state

In this chapter time-resolved photoelectron spectroscopy of the multi-electron dynamics of an autoionizing resonance excited in N_2 is presented. This experimental effort is carried out in collaboration with the group of Giuseppe Sansone at the Politecnico di Milano, who performed time-resolved (XUV+IR) transient absorption spectroscopy with attosecond time resolution on a series of autoionizing Rydberg states connected to the B $^2\Sigma_u^+$ state (18.78 eV) of N_2^+. This series of Rydberg states is also named the Hopfield ("emission" and absorption) series [61]. We carry out a complementary and more differential experiment using time-, energy- and angular-resolved photoelectron spectroscopy. The monochromator is tuned to excite a resonance at 17.36 eV and the subsequent electron relaxation dynamics that take place on a timescale of a few femtoseconds are probed by a short IR pulse.

The phenomenon of autoionization in molecules refers to a delayed emission of an electron after the excitation of a temporarily bound Rydberg state (resonance) with an excitation energy above the ionization threshold of the molecule. In our case the excitation occurs via the absorption of a XUV photon and the emitted electron originating from the autoionization has the same kinetic energy as an electron corresponding to direct ionization [62]. In the XUV absorption spectrum the interference between the energy dependent phase of the Rydberg state and the continuum state leads to the well known Fano profile in the XUV absorption cross section, which is given by [63]:

$$\sigma_{Fano}(\epsilon) = \sigma_0 \frac{(q+\epsilon)^2}{1+\epsilon^2}, \qquad \epsilon = \frac{E - E_r}{\frac{\Gamma}{2}} \tag{8.1}$$

where σ_0 is the cross section of the direct ionization channel, E is the energy of the XUV light, E_r is the resonance energy of the Rydberg state, Γ is the spectral width of the autoionizing state and q is a parameter, that defines the asymmetry of the line shape. Recently the dynamics of such resonances in atoms have been studied by time-resolved spectroscopy tracking the time-dependent evolution of the absorption line shape [64], and by attosecond interferometry [65].

We extend these studies to molecules, in our case N_2, where the multi-electron dynamics can also be accompanied by structural dynamics of the molecule and the dynamics can not always be indirectly deduced from the absorption line shape. In figure 8.1 a synchrotron absorption spectrum for the XUV energies below the binding energy of the B state is presented [66]. Two series of Rydberg states connected to the B state are indicated. The $n\,d\sigma_g$ series has a strongly asymmetric Fano lineshape (high q parameters) resulting in
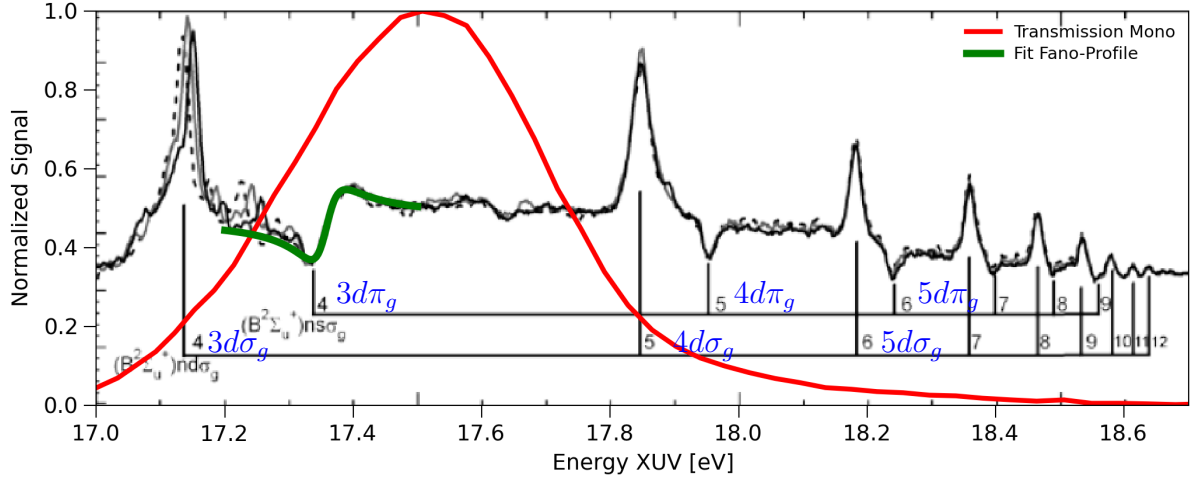
Figure 8.1: Synchrotron absorption measurement, taken from [66], with the measured monochromator energy transmission profile plotted on top. The labeling of the $s\sigma_g$ series from [66] is replaced by a $d\pi_g$ series, to be in agreement with [67]. A Fano profile is fitted to the $3d\pi_g$ resonance, yielding $E_r = 17.36\ eV$, $q = 0.8$ and $\Gamma = 0.05\ eV$.

absorption maxima. This series is traditionally labeled as the Hopfield absorption series. In the case of the $nd\pi_g$ series the situation is more complex. While for the resonances with small n the absorption profile has a relatively balanced Fano profile (q=1) the line shape gets more asymmetric towards an "emission" line shape (q<1) for higher n. These resonances with a reduction of the absorption cross section are also called window resonances. We change (in blue) the labeling of the $s\sigma$ series to a $d\pi_g$ series in agreement with the most comprehensive assignment available so far [67]. This series is traditionally labeled as Hopfield "emission" series. However some regions, for example the region between the $3d\sigma_g$ and the $3d\pi_g$ resonances, also exhibit a more complex absorption spectrum that definitely can not described by a Fano profile. Our aim is to study the decay of excited resonances in this energy region in the time domain.

8.1 XUV Energy Calibration

Careful calibration of the XUV photon energy transmitted through the monochromator is necessary to clearly identify the excited resonances. The calibration is performed in two steps exploiting photoelectron spectroscopy of Argon. First the energy scaling of the VMI is calibrated by recording a photoelectron spectrum generated by the full XUV comb coming from the HHG source. In this case the monochromator gratings are operated in zero order. The combination of the known ionization potential of Argon of 15.76 eV and the assumption that the comb maxima are odd multiples of the driver wavelength makes it possible to calibrate the VMI and the IR wavelength for the HHG process simultaneously,
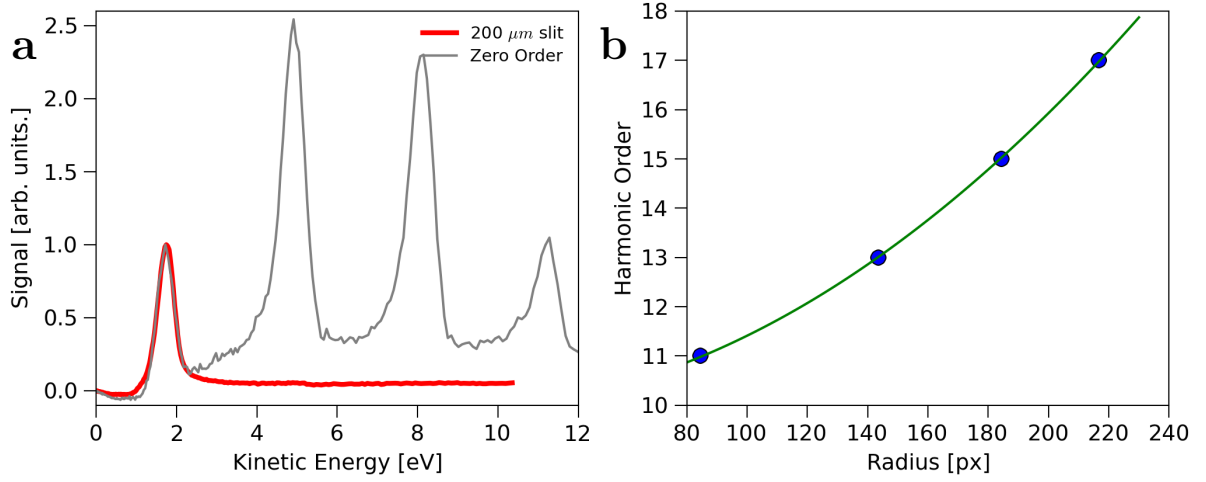
Figure 8.2: a: Photoelectron spectrum of Argon, for full the XUV comb coming from the HHG source and for a monochromatized XUV spectrum **b:** Fit of function 8.2 to the maxima positions of the full XUV comb induced photoelectron spectrum. The IR pulse center energy and the energy calibration of VMI are deduced from the fit.

see figure 8.2. The fit-function is:

$$n = (a \cdot r^2 + E_{IP})/E_{IR} \tag{8.2}$$

where r is the radius, n is the harmonic order, a is the energy calibration factor for the VMI image, E_{IP} is the ionization potential of Argon and E_{IR} is the center photon energy of the IR pulse. The fit yields:

$$E_{IR} = 1.591 \pm 0.005 \ eV \tag{8.3}$$

$$\lambda_{IR} = 779 \pm 2 \ nm \tag{8.4}$$

The IR center wavelength is slightly lower compared to the usual laser parameters when the center wavelength is around 795 nm. This is due to the special laser settings that are used to achieve the shortest possible pulse duration of about 21 fs. The monochromator is tuned to the center of H11 using a slit size of 208 μm. This results in a transmission which is peaks at 17.5 eV, with a FWHM width of about 0.5 eV to 0.6 eV. In figure 8.1, the measured XUV transmission is plotted as a red line on top of the synchrotron absorption measurement taken from [66].

8.2 Photoelectron Spectroscopy

After the XUV energy is calibrated via photoelectron spectroscopy of Argon, the target gas is directly changed to N_2 and a time-resolved XUV-IR pump-probe photoelectron
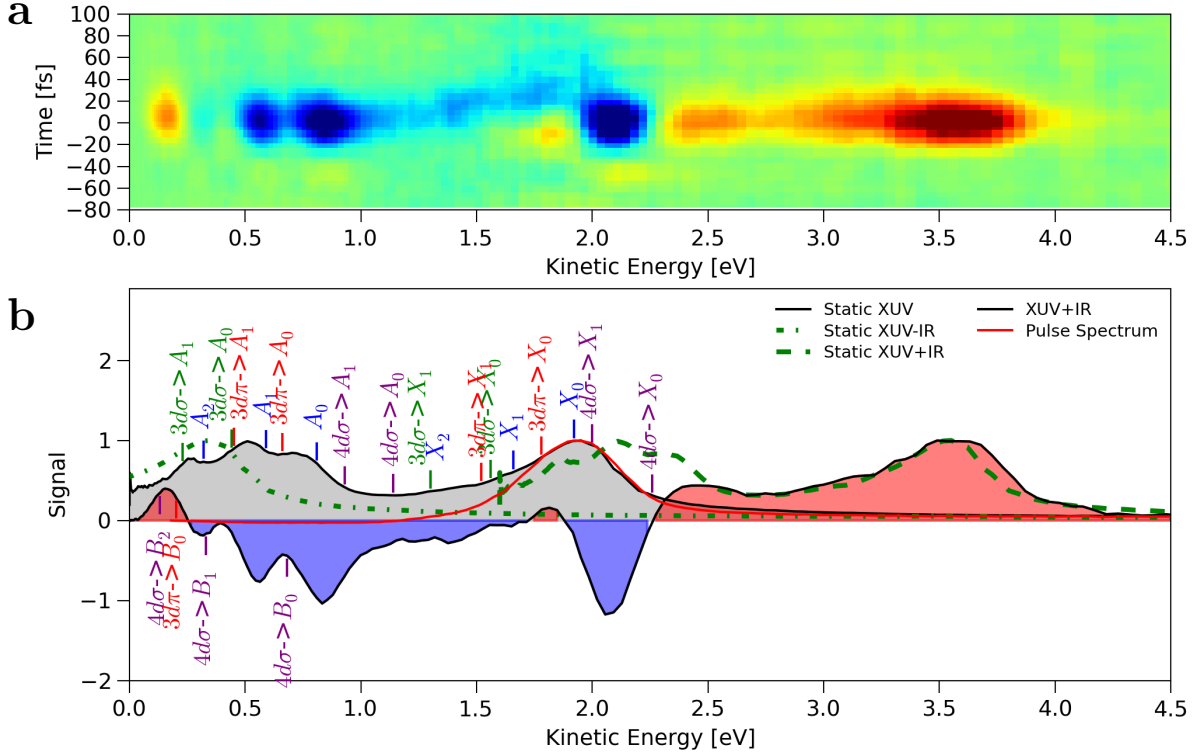
Figure 8.3: a: Time-resolved XUV-IR pump-probe photoelectron map. The static XUV spectrum is subtracted. **b:** The static XUV spectrum (grey). The differential spectrum at zero delay (blue and red). Blue labels refer to states corresponding to direct ionization. Red, green and purple labels to the three relevant resonances of the Hopfield series. The states that can be excited by the XUV pulse are indicated on the top of the static spectrum. States that can be excited by the combination of XUV+IR photons are indicated on the bottom the differential spectrum. Green dashed and dashed dotted lines are the shifted XUV static spectrum plus an minus the energy of an IR photon respectively.

map is recorded. In figure 8.3 the result is presented. Figure 8.3a shows a differential time-resolved map where the static XUV photoelectron spectrum is subtracted. The 8.3b shows the XUV only spectrum in grey, and the XUV+IR differential spectrum at zero pump-probe delay. Positive contributions are shaded in red and negative ones in blue. The differential spectrum is multiplied by a factor of 20, for better comparison with the static XUV spectrum. Before the discussion of the time-resolved data we will first give an interpretation of the static (XUV only) and the pump-probe spectrum (XUV+IR) at zero time delay.

State	X_0	X_1	X_2	A_0	A_1	A_2	B_0	B_1	B_2
B. E. [eV]	15.58	15.84	16.20	16.70	16.91	17.18	18.75	19.10	19.30
Kin. E. [eV]	1.92	1.66	1.30	0.81	0.59	0.32	-	-	-

State	$3d\sigma_g$				$3d\pi_g$				$4d\sigma_g$			
B. E. [eV]	17.14				17.36				17.84			
Continuum	X_0	X_1	A_0	A_1	X_0	X_1	A_0	A_1	X_0	X_1	A_0	A_1
Branch Rat.	0.30	0.11	0.25	0.22	0.23	0.06	0.23	0.23	0.24	0.02	0.13	0.15
Kin. E. [eV]	1.56	1.30	0.44	0.23	1.78	1.52	0.66	0.45	2.26	2.00	1.14	0.93

Table 8.1: Binding energies and the corresponding kinetic energies of the emitted electrons of the ionic states of N_2^+ and the three possible resonantly excited Rydberg states connected to the B state. The vibrational state of the ionic state is indicated by a subscript. The photon energy of the XUV pulse used to calculate the kinetic energies is 17.5 eV. The row "Continuum" denotes the ionic state the resonance is decaying to. The branching ratio of different autoionization channels is given with respect to the sum of all possible channels [68].

8.2.1 XUV Spectrum

In the table 8.1 relevant ionic continuum states, taken from [9], and resonances that have a excitation energy close to the XUV energy of 17.5 eV are listed. The vibrational states are indicated by a subscript. The energy of the resonances are deduced from figure 8.1. For the resonances $3d\sigma_g$ and $4d\sigma_g$ we set the binding energy to the maxima in the absorption cross-section. In case of the $3d\pi_g$ resonance we fit a Fano profile, as described in equation 8.1 to the data, yielding $E_r = 17.36\ eV$, $q = 0.8$ and $\Gamma = 0.05\ eV$. The kinetic energy of the electrons originating from direct ionization to the X and A state depends on the calibrated XUV photon energy of 17.50 eV and are also listed in table 8.1. The kinetic energy of the electrons produced by autoionization are independent of the XUV photon energy. After the "emission" of the electron the molecule can be left in any ionic state with a binding energy below the excitation energy of the resonance. We restrict the discussion to the vibrational states 0,1 and 2. In figure 8.3b the calculated kinetic energies of electrons originating from direct ionization are indicated in blue, electrons coming from the $3d\sigma_g$ resonance in green, from the $3d\pi_g$ resonance in red and from the $4d\sigma_g$ resonance in purple (The states that can be excited by the XUV pulse are indicated on the top of the figure 8.3b. States that can be excited by the combination of XUV+IR are indicated on the bottom of the figure 8.3b).

In the XUV only spectrum (grey) three vibrational states of the A state are clearly visible. They are slightly (about 0.05 eV) shifted with respect to the calculated position. We neglect this small mismatch. For the X state only the vibrational ground state can be identified. However the tail of the peak at 1.9 eV ranging to about 1 eV is likely to originate from the higher vibrational states of the X state.

The resonances are not energy resolved in the XUV only spectrum. First of all the

$3d\sigma_g$ and the $4d\sigma_g$ resonances are only excited with a small probability, since their energy positions are on the wings of the XUV photon energy profile, see figure 8.3. Only the $3d\pi_g$ resonance is excited with a reasonably high probability. Additionally the modulation of the total absorption cross section, in case of the $3d\pi_g$ resonance, is only about 10%. Furthermore the resonances decay via various channels, such that the individual modulation of the XUV only photoelectron spectrum is even more reduced.

8.2.2 XUV+IR spectrum

In figure 8.3b the spectrum at zero time delay between the XUV and IR pulse is presented. The XUV only spectrum is subtracted and the resulting differential spectrum is multiplied by a factor of 20. There are two types of IR-induced features visible. At temporal overlap between the XUV pulse and the IR pulse sideband generation is visible. If we neglect the contribution of the resonances to the static XUV spectrum we essentially see the complete photoelectron spectrum shifted to higher and lower kinetic energies by the IR photon energy. The shifted static spectra are indicated by green dashed and dashed-dotted lines. The differential spectrum is the sum of these two positive sideband contributions and the depletion of the static XUV spectrum. Clearly visible is the positive sideband of the X state around 3.5 eV and the depletion of two vibrational A states between 0.4 eV and 0.9 eV. In the region between 0 eV and 0.5 eV we see the sum of the n=-1 sideband of the X state and the depletion of the higher vibrational A states. In the region between 1.5 eV and 2.5 eV the situation is similar. Here the spectrum is the sum of the n=+1 sideband of the A state and the depletion of the X state. These however are not all the spectroscopic contributions in the spectrum.

For the resonances we can observe the sequential absorption of an XUV photon followed by an IR photon. The XUV photon excites the resonance and the IR photon changes the subsequent multi-electron dynamics by directly ionizing the molecule before it can decay via autoionization. The ionized molecule can thus be left in a different ionic state after the IR induced ionization as compared to the ionic state it would end up in after autoionization. In table 8.2 the kinetic energies of electrons originating from an ionization of the resonances by a single IR photon leaving the molecule in the B-state are listed. The discussion is restricted to vibrational states up to 2.

Resonance	$3d\sigma_g$	$3d\pi_g$			$4d\sigma_g$		
Coupling to	-	B_0	B_1	B_2	B_0	B_1	B_2
Kin. E. [eV]	–	0.201	-	-	0.681	0.331	0.131

Table 8.2: Kinetic energies of electrons resulting from autoioinzing resonances coupled to the B state by an IR photon.

The $3d\sigma_g$ state can not be ionized by a single IR photon, because the energy gap between the resonance and the continuum B state is too big. For the other two states the electrons created by the ionization to the B state make a positive contribution with kinetic energies given in the table 8.2. A clear identification of the observed IR induced couplings of the
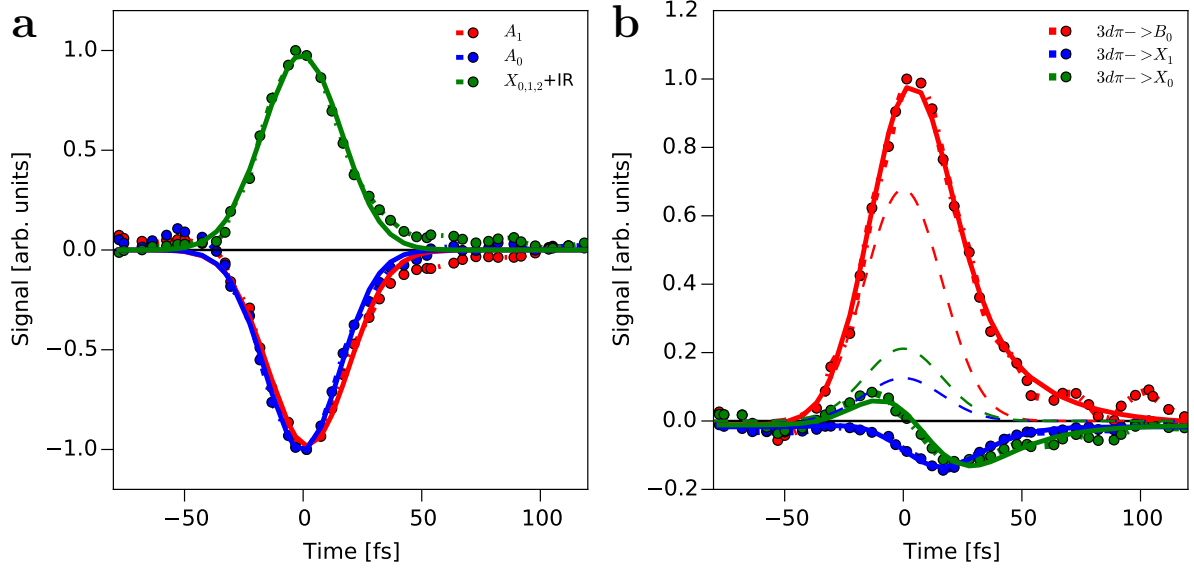
Figure 8.4: Time transients for various energy regions in figure 8.3a. **a:** All transients that are reflecting the cross correlation between XUV and IR. **b:** Time transients corresponding to features that exhibit dynamics exceeding pure sideband generation.

resonances to different ionic states is easier to make in the time-resolved maps, whose interpretation will now follow.

8.2.3 Dynamics

In figure 8.3a the time-resolved differential map is presented. Since most of the spectral features arise from sideband generation they are perfect indicators for the time resolution of the experiment, i.e. the cross-correlation between the XUV pulse and the IR pulse. We take the n=1 sideband of the X state at 3.5 eV and the two depletions corresponding to the $A_{0,1}$ states at 0.8 eV and 0.6 eV and assume that the transients of this energy regions are strongly dominated by sideband generation. Transients of the features are presented in figure 8.4a. A Gaussian profile is fitted to the transients:

$$S_G(t, t_0, a, \sigma_{cc}) = a \cdot e^{-0.5 \cdot (\frac{t-t_0}{\sigma_{cc}})^2} \tag{8.5}$$

where σ_{cc} is the Gaussian width , t_0 is time zero and a is an amplitude. The results are presented in table 8.3. The average of the individual σ_{cc} presented in the table is 16.3 fs (FWHM: 38.3 fs).

We can identify two energy regions in figure 8.3a that show dynamic behaviour that goes beyond sideband generation. In the energy range from about 0.05 eV to 0.25 eV a positive contribution is visible and in the range from about 1.5 eV to about 2 eV a depletion is visible, that is overlapped with a small positive contribution, that is originating from

State	$X_{0,1,2}$+IR	A_0	A_1
σ_{cc}	16.7	16.0	16.1
$\Delta\sigma_{cc-error}$	0.49	0.62	0.69

Table 8.3: Fit results for Gaussian widths for different spectroscopic features induced by sideband generation.

the n=1 sideband of the A-state. In figure 8.3b the expected kinetic energies (given in table 8.2) of electrons from XUV+IR absorption are indicated in the differential spectrum on the bottom. The positive contribution which peaks at about 0.15 eV coincides with the calculated kinetic energy of electron coming from a coupling of the $3d\pi_g$ resonance to the B_0 state. And indeed the depletion between 1.5 eV and 2 eV coincides with the kinetic energy of electron arising from autoionization of the $3d\pi_g$ state into the two lowest vibrational states of the X state (the kinetic energies are given in table 8.1). In the future discussion we divide this energy range into to sections, namely 1.4 eV to 1.6 eV and 1.7 eV to 1.9 eV, associated with the decay into the vibrational states X_0 and X_1. The coupling of the $4d\sigma_g$ resonance to the B_2 state would also result in electrons in the region around 0.15 eV. However this channel is excited with less probability since the excitation energy of this resonance is on the wings of the spectrum of the XUV pulse and we will (for now) associate the region around 0.15 eV with the $3d\pi_g->B_0$ channel. The transients corresponding to the spectral regions are plotted in the figure 8.4b.

Deducing meaningful time constants from these transients is challenging, since the dynamics are happening on time scales close to the time resolution of the measurement. We start with the 0.05 eV to 0.25 eV region. The transient in this energy region is the sum of the n=-1 sideband of the X state, the depletion of the A-state and from the coupling by the IR of the $3d\pi_g$ resonance to the B_0 continuum. We assume that the feature does not change its kinetic energy with time and assume that the probability of ionizing the resonance with the IR photon stays constant with time and can be described by a single decay constant. We are therefore fitting the sum of Gaussian shaped contribution and a function describing a single decay convoluted with Gaussian filter that is accounting for the time resolution of the experiment:

$$S_{tot}(t, bgr, \sigma_{cc}, t_0, a_1, \tau, a_2) = a_1 S(t, t_0, \tau, \sigma_{cc}) + a_2 S_G(t, t_0, a_2, \sigma_{cc}) \quad (8.6)$$

where a_1 and a_2 are amplitudes, S_G is described in equation 8.5 and S is given by [59]:

$$S(t, t_0, \tau, \sigma_{cc}) = exp\left[-\frac{t-t_0}{\tau}\right] exp\left[\frac{1}{2}\left(\frac{\sigma_{cc}}{\tau}\right)^2\right]\frac{1}{2}\left(1 + erf\left[\frac{1}{\sqrt{2}}\left(\frac{t-t_0}{\sigma_{cc}} - \frac{\sigma_{cc}}{\tau}\right)\right]\right) \quad (8.7)$$

where τ is the decay constant and σ_{cc} is the time resolution.

For the fit the time resolution is fixed to $\sigma_{cc-gauss} = 16.3\ fs$, the result from the sideband transients, and t_0 is fixed to zero. The result is given in table 8.4. Unfortunately the

Channel	E. Range [eV]	a_1	a_2	$\tau[fs]$
$(3d\pi_g- > B_0)$	0.05-0.25	0.9 ± 0.2	0.58 ± 0.06	25 ± 3
$3d\pi_g- > X_0$	1.7-1.9	-0.5 ± 0.1	0.21 ± 0.02	20 ± 2
$3d\pi_g- > X_1$	1.4-1.6	-0.9 ± 0.2	0.12 ± 0.02	10 ± 1

Table 8.4: Result of fit of function 8.6 to different transients presented in figure 8.4b. t_0 is fixed to 0 and σ_{cc} is fixed to 16.3 fs.

correlation between τ and the amplitude of the Gaussian background is high, since the decay is close to the time resolution of the measurement. The result for τ therefore has to be taken with caution. The transient of the energetic region between 1.5 eV and 2 eV is the sum of and the n=1 sideband of the $A_{0,1,2}$ states, the depletion of the $X_{0,1,2}$ states and the depletion of the autoionizing $3d\pi_g$ resonance decaying to X_0 or X_1. Again it is unclear what the amplitude of the Gaussian shaped background is, although we can see that the positive contribution of the positive sideband dominates over the depletion of the X state at least for the energy region from 1.7 eV to 1.9 eV. We fit the same fit function 8.6, where σ_{cc} is fixed to 16.3 fs and t_0 is zero. The Gaussian background now has a negative amplitude. The results are also given in table 8.4.

Unfortunately the strong correlation between the amplitude of the Gaussian shaped background and the decay constant of the resonance makes it difficult to reliably estimate the error of the fit. However it seems that it is not possible to fit the transient of the 1.4 eV to 1.6 eV region with a decay constant above 20 fs. We will comment on this in the discussion.

8.3 Photoelectron Angular Distributions

The angular distributions of the emitted photoelectrons of the time-resolved spectroscopy gives additional information about the electronic states. The two VMIS images presented in figure 8.5a and 8.5b show a two-dimensional cut through the momentum distribution of the emitted photoelectrons. Image a shows the XUV-only distribution and image b shows the background-subtracted cut at a pump-probe delay of zero. In both images the laser polarization is vertical. The emitted angular distributions have cylindrical symmetry around this polarization axis. For single photon ionization the angular distribution of the electrons can be described by the following equation:

$$\frac{d\sigma_i}{d\Omega} = \frac{\sigma_i}{4\pi} \left[1 + \beta_2 P_2(cos\phi)\right] \tag{8.8}$$

where σ_i is the partial cross-section of the individual ionization channel, Ω is the solid angle, P_2 is the second order Legendre polynomial, ϕ is angle between the emitted electron and the direction of the electric field of the laser and β_2 is a parameter defining the asymmetry of the angular distribution. The function 8.8 is fitted to the angular distributions of
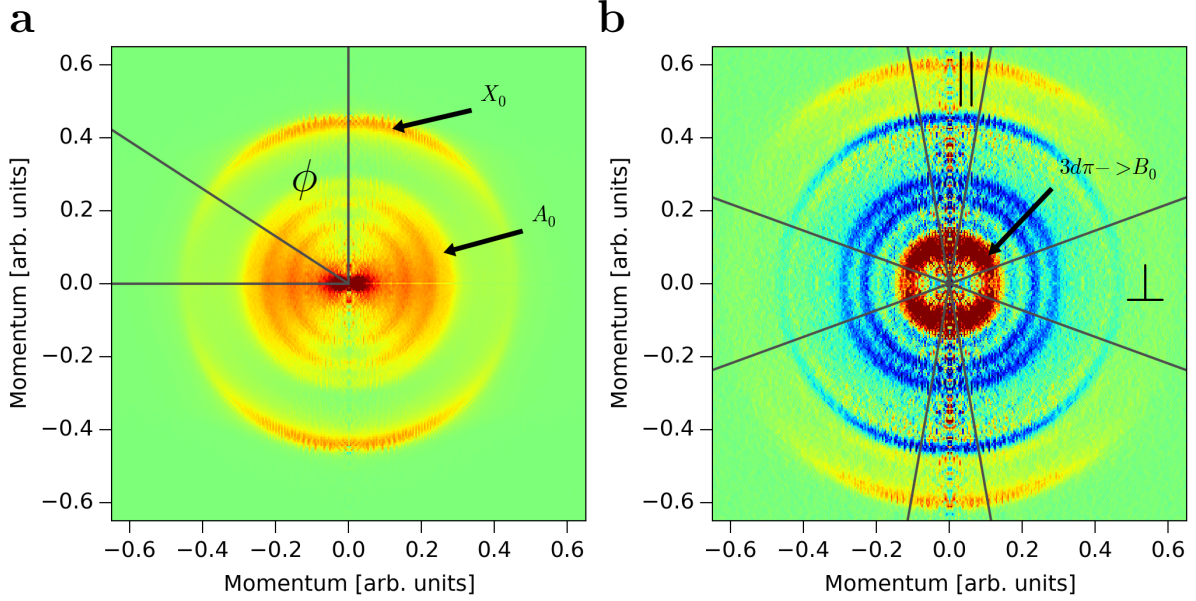
a

b

Figure 8.5: Angular distributions of the photoelectrons. **a:** XUV-only momentum distribution showing contributions of ionization to the X and A states. **b:** XUV+IR differential momentum distribution at time zero.

photoelectrons originating from ionization into the vibrational ground states of the X and A state in the XUV-only image in figure 8.5 yielding:

	Static	
State	X	$A_{\nu=0}$
β_2 (this work)	0.97	-0.36
β_2 literature	1	-0.3

Table 8.5: β_2 parameters extracted from the experimental data presented in figure 8.5a and literature values for β_2 taken from [69, 70]

Both values agree well with values given in the literature [69, 70]. For the spectral features in the time-resolved maps that originate from the multiphoton (XUV+IR) ionization the analysis of the angular distributions is more challenging. A momentum distribution for time zero is presented in figure 8.5b. Generally one can observe that the sideband generation dominantly occurs in the direction of the laser polarization. This is also true for the A state, that in case of the XUV-only ionization emits electrons dominantly perpendicular to the laser polarization. Theoretically equation 8.8 has to be extended by higher order Legendre polynomials to correctly account for the more complex multi photon ionization channels. However we are also facing some technical challenges that complicate the analysis. The asymmetry parameters are extremely sensitive to the background subtraction of the XUV-only spectrum. We therefore chose a more robust method that gives first insights into the
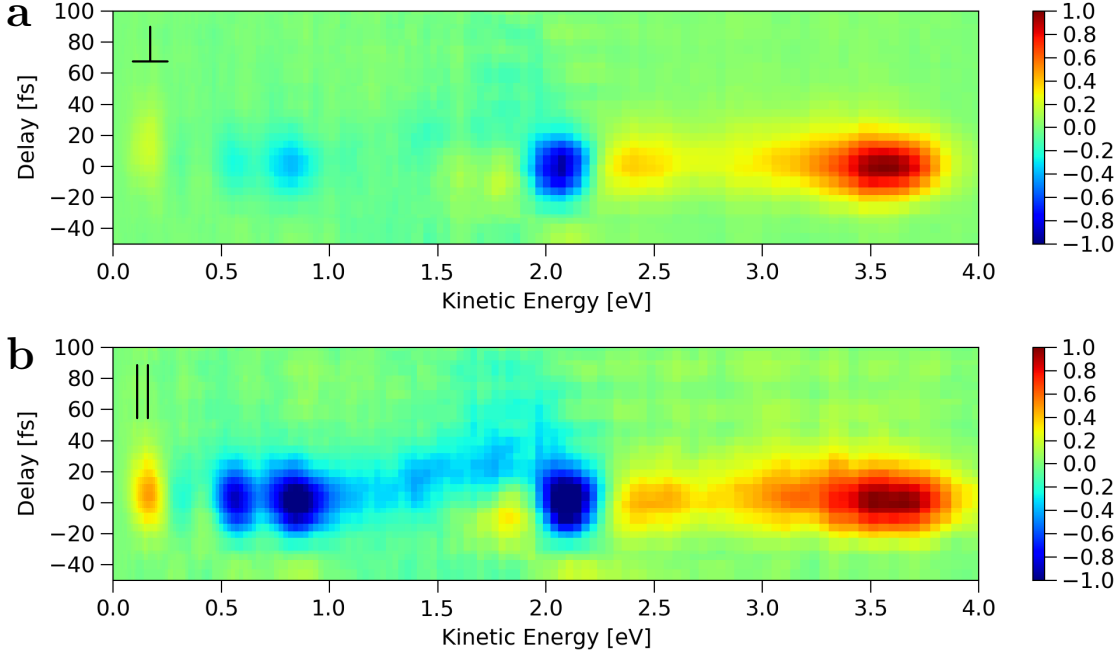
Figure 8.6: a: Differential time-resolved pump-probe map for the emission angle of section $D_\perp$. **b:** Differential time-resolved pump-probe map for the emission angle of section $D_\parallel$. Both maps are normalized to n=1 sideband of the X state.

dynamic behaviour of the angular distribution. The momentum distribution is separated into areas:

$$D_\parallel : \quad [-10°, 10°] \tag{8.9}$$
$$D_\perp : \quad [(90 - 20)°, (90 + 20)°] \tag{8.10}$$

.

The areas are also indicated in figure 8.5b. In figure 8.6 the time-resolved pump-probe XUV+IR maps for the two areas are presented. In both cases the maps are normalized to the maximum of the n=1 sideband (at about 3.5 eV) of electrons originating from ionization into the $X_{0,1,2}$ states. It is directly evident that most of the spectroscopic features have angular distributions different from the sideband, leading to a difference in amplitude of individual features when comparing both maps. In figure 8.7 the transients for the energy region between 0.05 eV and 0.25 eV and the region between 1.7 eV and 1.9 eV are presented. The transients are normalized to their maximum. Again function 8.6 is fitted to the transients with $t_0 = 0$ and $\sigma_{cc} = 16.3$ fs. The results are given in table 8.6

Clearly the transient of the parallel transition in figure 8.7a has a later onset and a smaller Gaussian shaped contribution. This is surprising since we attributed the Gaussian shaped contribution in the fit function to sideband generation present in the spectra. However the sideband generation is dominant along the laser polarization which is in contradiction with

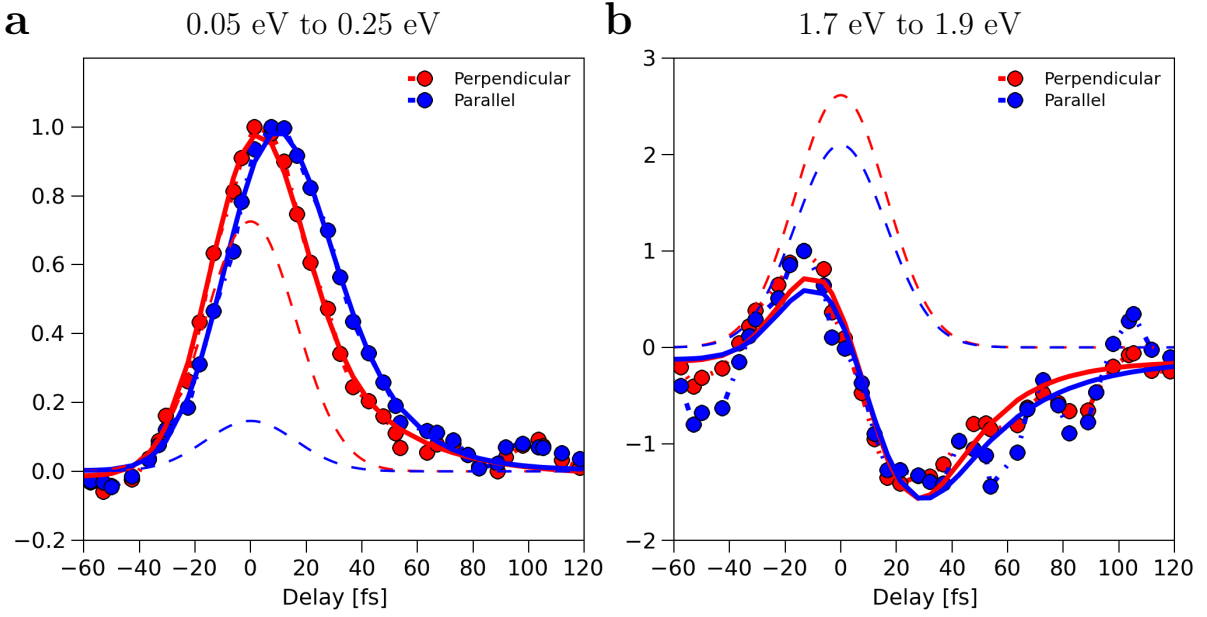**a**   0.05 eV to 0.25 eV   **b**   1.7 eV to 1.9 eV

Figure 8.7: a: Transient integrated of the energy region between 0.05 eV and 0.25 eV in the maps presented in figure 8.6. **b**: Transient integrated of the energy region between 1.7 eV and 1.9 eV in the maps presented in figure 8.6. The dotted lines indicate the Gaussian "background" contribution in the function that is fitted to the transients at that is described in equation 8.6.

Channel	E. Range [eV]	Area	a_1	a_2	$\tau_1[fs]$
$(3d\pi_g->B_0)$	0.05-0.25	$\perp$	0.7 ± 0.1	0.72 ± 0.03	28 ± 4
$(3d\pi_g->B_0)$	0.05-0.25	$\parallel$	2.6 ± 0.2	0.14 ± 0.04	17 ± 1
$3d\pi_g->X_0$	1.7-1.9	$\perp$	-7 ± 1	2.0 ± 0.3	19 ± 2
$3d\pi_g->X_0$	1.7-1.9	$\parallel$	-5 ± 1	2.1 ± 0.3	27 ± 6

Table 8.6: Result of fit of function 8.6 to different transients presented in figure 8.7. t_0 is fixed to 0 and σ_{cc} is fixed to 16.3 fs.

the results for the different emission angles presented here. We therefore propose a different interpretation, namely that the Gaussian shaped contribution also originates from probing a resonance that decays on a time-scale that is not resolved by the present experiment. We are therefore observing two channels with different decay constants. One possible candidate for the second channel (next to the $3d\pi_g->B_0$ channel) is the $4d\sigma_g->B_2$ channel that is also indicated in the figure 8.3b. However this requires vibrational excitation of the ion core by two photons upon ionization by the IR pulse. This scenario seems doubtful for ionization of loosely bound Rydberg electrons. Another option is the $3s\sigma_g$ state, which is the member of the Ogawa-Tanaka series [71] also expected in the same excitation energy region as the $3d\pi_g$ resonance, but not identified so far. We find this assignment more probable and will accept if for the rest of the discussion. However it is not clear which of the channels is associated with the fast and the slower decay. In case of the $3d\pi_g$ resonance

the decay time deduced from the Fano line shape in the absorption spectrum in figure 8.1 is about $\hbar/\Gamma = 13 \, fs$, while the decay time we observe for the parallel transient is slower. This would favour an assignment of the faster contribution to the $3d\pi_g$ state, while the slower contribution dominant in the transient of parallel transition can be assigned to the $3s\sigma_g$ resonance.

8.4 Summary

The results presented here demonstrate the experimental advantages of an XUV source with both excellent time and energy resolution. Meaningful photoelectron spectroscopy on the ultra-fast decay of an autoionizing resonance is drastically simplified with the increased energy resolution of our source in comparison to an unfiltered HHG-XUV source. Simultaneously the time resolution has to be also excellent to track the ultra-fast dynamics in the time domain.

We are able to identify the decay of the $3s\sigma_g$ resonance of the Ogawa-Tanaka absorption series and the decay of $3d\pi_g$ resonance of the Hopfield "emission" series in the data. We are only able to distinguish the two decay channels by exploiting the angular resolution provided by the VMIS and by comparison of the observed decay times with decay time deduced from absorption spectroscopy. The decay of the $3d\pi_g$ resonance is not time resolved by the experiment, but we are able to measure a decay constant of 28 ± 4 fs for the $3s\sigma_g$ resonance.

In case of the $3d\pi_g$ resonance it is of special interest to study the decay dynamics in the time domain, since the absorption spectrum exhibits a more complex structure than can be described by a single Fano line shape. This will become possible in the future when the time-resolution of the monochromator beamline is improved.

9 Summary and Outlook

This thesis presents investigation of XUV photoionization dynamics in nitrogen molecules using a novel XUV time delay compensating monochromator beamline.

The first part of the thesis presents the design and implementation of a laser driven HHG beamline for XUV-IR pump-probe time-resolved spectroscopy. The key element of the beamline is a grating-based time delay compensating XUV monochromator that enables tuning the photon energy of the XUV pulse coming from the HHG source between 10 eV and 50 eV while having a spectral width of less than 0.5 eV and a pulse duration below 15 fs. The optical layout of the monochromator was provided by our collaborators in the group of Luca Poletto at CNR-IFN in Padua and the mechanical implementation is carried out by ourselves with a special focus on stability and usability of the beamline. One of the important tasks is the design and alignment of the grating holders that need to be optimized for a wide range of photon energies (10 eV to 50 eV) and have to provide high reliability in automated switching between photon energies in the course of experiments. Another important design problem is the overall stability of the pump-probe setup inside the vacuum system and the precise initial and daily alignment of the XUV monochromator.

The beamline provides the possibility to exchange the experimental endstation that is used to perform the experiments. A velocity map imaging spectrometer (VMIS) is used in the thesis to perform angular resolved photoelectron and photoion spectroscopy of gaseous targets. Photoelectron spectroscopy of rare gases is used to determine the performance of the beamline. The achieved performance parameters are in good agreement with the output of theoretical modelling, that is also presented.

The first experimental result presented in the thesis is a time- and energy-resolved study of the dissociation dynamics of N_2 upon inner-valence ionization from the $2\sigma_g$ orbital with an ionization potential of about 37 eV. In this energy region theoretical modelling is extremely challenging due to the high excitation in the system and the complex multi-electron dynamics that are involved. Experimental efforts, in close coupling with theoretical modelling, are needed to gain deeper insights into the physics of this highly electronically correlated system. The tunability of the XUV spectral energy in combination with the short pulse duration of the pulse provided by the beamline are excellent tools to study these complex dynamics in the time domain.

The spectral photon energy of the XUV pulse is tuned in a range between 32 eV and 48 eV around the threshold energy of the inner-valence ionization of 37 eV. The induced electronic and structural dynamics are probed with a moderately strong IR pulse and time delay dependent angular-resolved electron and ion spectra are recorded with the VMIS.

The spectroscopic interpretation of the XUV-only spectra are not consistent with the

existing *ab initio* results describing the adiabatic dissociation dynamics of the H-band of N_2 [15]. New calculations, carried out by collaborators within our group, yield improved potential energy curves for the relevant energy region that are in good agreement with the observed experimental data and produce the correct dissociation limits for the H-band.

In the interpretation of the time-resolved spectroscopy the tuning of the XUV energy enables us to identify different dissociation channels with excitation energies close to the threshold energy of 37 eV that are either resonant to the XUV energy and arise from direct ionization. We can clearly identify the creation of a $2\sigma_g^{-1}$ hole dissociating towards a limit with the neutral N atom excited to the n=3 manifold (i.e. L10, L11). We describe the observed dynamics within a simplified model of dissociation. The model can reproduce the general trend of the observed spectroscopic features in the electron and ion spectra. The parameters of the model are used to determine characteristic spectroscopic features of the electronic states with accuracy higher than the output of the new *ab initio* calculations. Besides the general trend the data also exhibits more complex spectroscopic changes that depend both on time delay and the XUV photon energy. These effects are not reproduced by the simplified model. The results presented in this part of the thesis also demonstrate the technical capabilities and experimental advantages of the XUV monochromator beamline.

The second experimental result presented in the thesis is a time-resolved study of the ultrafast decay of an autoionizing resonance (17.3 eV) of the Hopfield emission series of N_2. The XUV photon energy is tuned to dominantly excite a resonance of interest and the resulting multi-electron dynamics are probed by a short IR pulse. Time- and angular-resolved photoelectron spectroscopy is performed yielding direct access to the electron dynamics. We are able to time-resolve the decay dynamics of the autoionizing resonance, that are in the range of 20 fs, and compare our findings with other static and time-resolved studies. The requirements on time and energy resolution of the experiment are extremely high and thus the results are also an excellent demonstration of the utility of the beamline.

In the future the experimental technique can be applied to more complex resonant multi-electron dynamics where the access to angular and time-resolved information about the electron dynamics is crucial to the description of the process. A variety of gas phase molecules will be investigated including more complex autoionization and dissociation processes in highly excited and superexcited molecules. First steps in this direction have already been made with the investigation of neutral dissociation just below the dissociative ionization threshold of N_2. Further application of the beamline involve a liquid microjet endstation, which has been constructed with participation of the author of the thesis. This technique allows to record photoelectron spectra of solvated molecules and will be used to investigate the electronic structure of various biologically-relevant chromophores and their interaction with the environment.

Bibliography

[1] Matthias Uiberacker, Th Uphues, Martin Schultze, Aart Johannes Verhoef, Vladislav Yakovlev, Matthias F Kling, Jens Rauschenberger, Nicolai M Kabachnik, Hartmut Schröder, Matthias Lezius, et al. Attosecond real-time observation of electron tunnelling in atoms. *Nature*, 446(7136):627–632, 2007.

[2] Giuseppe Sansone, F Kelkensberg, JF Pérez-Torres, Felipe Morales, Matthias F Kling, W Siu, Omair Ghafur, Per Johnsson, Marko Swoboda, E Benedetti, et al. Electron localization following attosecond molecular photoionization. *Nature*, 465(7299):763–766, 2010.

[3] Martin Schultze, Krupa Ramasesha, CD Pemmaraju, SA Sato, D Whitmore, A Gandman, James S Prell, LJ Borja, D Prendergast, K Yabana, et al. Attosecond band-gap dynamics in silicon. *Science*, 346(6215):1348–1352, 2014.

[4] Etienne Gagnon, Predrag Ranitovic, Xiao-Min Tong, C. L. Cocke, Margaret M. Murnane, Henry C. Kapteyn, and Arvinder S. Sandhu. Soft x-ray-driven femtosecond molecular dynamics. *Science*, 317(5843):1374–1378, 2007.

[5] Arno Ehresmann, Shuntaro Machida, Masashi Kitajima, Masatoshi Ukai, Kosei Kameta, Noriyuki Kouchi, Yoshihiko Hatano, Eiji Shigemasa, and Tatsuji Hayaishi. Dissociative single and double photoionization with excitation between 37 and 69 ev in n 2. *Journal of Physics B: Atomic, Molecular and Optical Physics*, 33(3):473, 2000.

[6] M. Lucchini, K. Kim, F. Calegari, F. Kelkensberg, W. Siu, G. Sansone, M. J. J. Vrakking, M. Hochlaf, and M. Nisoli. Autoionization and ultrafast relaxation dynamics of highly excited states in n_2. *Phys. Rev. A*, 86:043404, Oct 2012.

[7] Luca Poletto, Paolo Villoresi, Fabio Frassetto, Francesca Calegari, Federico Ferrari, Matteo Lucchini, Giuseppe Sansone, and Mauro Nisoli. Time-delay compensated monochromator for the spectral selection of extreme-ultraviolet high-order laser harmonics. *Review of Scientific Instruments*, 80(12):123109, 2009.

[8] Martin Eckstein, Chung-Hsin Yang, Markus Kubin, Fabio Frassetto, Luca Poletto, Hans-Hermann Ritze, Marc JJ Vrakking, and Oleg Kornilov. Dynamics of n2 dissociation upon inner-valence ionization by wavelength-selected xuv pulses. *The Journal of Physical Chemistry Letters*, 2015.

[9] Forrest R. Gilmore. Potential energy curves for n2, no, {O2} and corresponding ions. *Journal of Quantitative Spectroscopy and Radiative Transfer*, 5(2):369 – IN3, 1965.

[10] M. Magrakvelidze, O. Herrwerth, Y. H. Jiang, A. Rudenko, M. Kurka, L. Foucar, K. U. Kühnel, M. Kübel, Nora G. Johnson, C. D. Schröter, S. Düsterer, R. Treusch, M. Lezius, I. Ben-Itzhak, R. Moshammer, J. Ullrich, M. F. Kling, and U. Thumm. Tracing nuclear-wave-packet dynamics in singly and doubly charged states of n_2 and o_2 with xuv-pump–xuv-probe experiments. *Phys. Rev. A*, 86:013415, Jul 2012.

[11] Hermann Haken and Hans C Wolf. *Molekülphysik und Quantenchemie: Einführung in die experimentellen und theoretischen Grundlagen*. Springer-Verlag, 2013.

[12] Attila Szabo and Neil S Ostlund. *Modern quantum chemistry: introduction to advanced electronic structure theory*. Courier Corporation, 2012.

[13] Ingolf V Hertel and C-P Schulz. *Atome, Molekule Und Optische Physik 2 Molekule Und Photonen-Spektroskopie Und Streuphysik*, volume 2. Springer-Verlag, 2011.

[14] P.W. Langhoff, S.R. Langhoff, T.N. Rescigno, J. Schirmer, L.S. Cederbaum, W. Domcke, and W. Von Niessen. Theoretical studies of inner-valence-shell photoionization cross sections in {N2} and {CO}. *Chemical Physics*, 58(1):71 – 91, 1981.

[15] Tomohiro Aoto, Kenji Ito, Yasumasa Hikosaka, Akihiro Shibasaki, Ryo Hirayama, Norifumi Yamamono, and Eisaku Miyoshi. Inner-valence states of n[sub 2][sup +] and the dissociation dynamics studied by threshold photoelectron spectroscopy and configuration interaction calculation. *The Journal of Chemical Physics*, 124(23):234306, 2006.

[16] Garnet Kin-Lic Chan and Martin Head-Gordon. Highly correlated calculations with a polynomial cost algorithm: A study of the density matrix renormalization group. *The Journal of chemical physics*, 116(11):4462–4476, 2002.

[17] Garnet Kin-Lic Chan. An algorithm for large scale density matrix renormalization group calculations. *The Journal of chemical physics*, 120(7):3172–3178, 2004.

[18] Debashree Ghosh, Johannes Hachmann, Takeshi Yanai, and Garnet Kin-Lic Chan. Orbital optimization in the density matrix renormalization group, with applications to polyenes and β-carotene. *The Journal of chemical physics*, 128(14):144117, 2008.

[19] Thom H Dunning Jr. Gaussian basis sets for use in correlated molecular calculations. i. the atoms boron through neon and hydrogen. *The Journal of Chemical Physics*, 90(2):1007–1023, 1989.

[20] Luca Poletto. Tolerances of time-delay-compensated monochromators for extreme-ultraviolet ultrashort pulses. *Appl. Opt.*, 48(23):4526–4535, 2009.

[21] L. Poletto, P. Villoresi, E. Benedetti, F. Ferrari, S. Stagira, G. Sansone, and M. Nisoli. Temporal characterization of a time-compensated monochromator for high-efficiency selection of extreme-ultraviolet pulses generated by high-order harmonics. *J. Opt. Soc. Am. B*, 25(7):B44–B49, 2008.

[22] Luca Poletto, Paolo Villoresi, Enrico Benedetti, Federico Ferrari, Salvatore Stagira, Giuseppe Sansone, and Mauro Nisoli. Intense femtosecond extreme ultraviolet pulses by using a time-delay-compensated monochromator. *Opt. Lett.*, 32(19):2897–2899, 2007.

[23] T Pfeifer, Ch Spielmann, and G Gerber. Femtosecond x-ray science. *Reports on Progress in Physics*, 69(2):443, 2006.

[24] P. B. Corkum. Plasma perspective on strong field multiphoton ionization. *Phys. Rev. Lett.*, 71:1994–1997, Sep 1993.

[25] Vasileios-Marios Gkortsas, Siddharth Bhardwaj, Edilson L Falcão-Filho, Kyung-Han Hong, Ariel Gordon, and Franz X Kärtner. Scaling of high harmonic generation conversion efficiency. *Journal of Physics B: Atomic, Molecular and Optical Physics*, 44(4):045601, 2011.

[26] Piotr Rudawski, CM Heyl, Fernando Brizuela, Jörg Schwenke, Anders Persson, Erik Mansten, Rafal Rakowski, Linnea Rading, Filippo Campi, Byunghoon Kim, et al. A high-flux high-order harmonic source. *Review of Scientific Instruments*, 84(7):073103, 2013.

[27] Katalin Varjull, Y Mairesse, B Carré, MB Gaarde, Per Johnsson, S Kazamias, R López-Martens, Johan Mauritsson, KJ Schafer, Ph Balcou, et al. Frequency chirp of harmonic and attosecond pulses. *Journal of Modern Optics*, 52(2-3):379–394, 2005.

[28] Luca Poletto and Paolo Villoresi. Time-delay compensated monochromator in the off-plane mount for extreme-ultraviolet ultrashort pulses. *Appl. Opt.*, 45(34):8577–8585, 2006.

[29] M Wieland, Ch Spielmann, U Kleineberg, Th Westerwalbesloh, Ulrich Heinzmann, and T Wilhein. Toward time-resolved soft x-ray microscopy using pulsed fs-high-harmonic radiation. *Ultramicroscopy*, 102(2):93–100, 2005.

[30] Eiji J Takahashi, Masatoshi Hatayama, Satoshi Ichimaru, and Katsumi Midorikawa. Dispersion-free monochromator for selecting a single high-order harmonic beam. In *CLEO: QELS_Fundamental Science*, pages FTu3B–6. Optical Society of America, 2014.

[31] Fabio Frassetto, Cephise Cacho, Chris A. Froud, I. C. Edmund Turcu, Paolo Villoresi, Will A. Bryan, Emma Springate, and Luca Poletto. Single-grating monochromator for extreme-ultraviolet ultrashort pulses. *Opt. Express*, 19(20):19169–19181, 2011.

[32] Motohiko Ito, Yoshimasa Kataoka, Tatsuya Okamoto, Mikio Yamashita, and Taro Sekikawa. Spatiotemporal characterization of single-order high harmonic pulses from time-compensated toroidal-grating monochromator. *Opt. Express*, 18(6):6071–6078, 2010.

[33] L. Poletto. Efficiency of gratings in the conical diffraction mounting for an euv time-compensated monochromator. *Proc. SPIE*, 5534(1):144, 2004. 10.1117/12.573135.

[34] W. Werner. X-ray efficiencies of blazed gratings in extreme off-plane mountings. *Appl. Opt.*, 16(8):2078–2080, 1977.

[35] J. F. Seely, L. I. Goray, Benjawan Kjornrattanawanich, J. M. Laming, G. E. Holland, K. A. Flanagan, R. K. Heilmann, C. H. Chang, M. L. Schattenburg, and A. P. Rasmussen. Efficiency of a grazing-incidence off-plane grating in the soft-x-ray region. *Appl. Opt.*, 45(8):1680–1687, 2006.

[36] Max Born and Emil Wolf. *Principle of Optics*. Pergamon Press, 1970.

[37] P Salieres, T Ditmire, MD Perry, Anne L'Huillier, and M Lewenstein. Angular distributions of high-order harmonics generated by a femtosecond laser. *Journal of Physics B: Atomic, Molecular and Optical Physics*, 29(20):4771, 1996.

[38] Zenghu Chang. *Fundamentals of Attosecond Optics*. CRC Press, 2011.

[39] Christopher C Davis and Michael A Coplan. *Building scientific apparatus*. Cambridge University Press, 2009.

[40] Oleg Kornilov, Russell Wilcox, and Oliver Gessner. Nanograting-based compact vacuum ultraviolet spectrometer and beam profiler for in situ characterization of high-order harmonic generation light sources. *Review of Scientific Instruments*, 81(6):063109, 2010.

[41] Markus Kubin. Wavelength-tunable xuv-pulses for femtosecond xuv-ir nonlinear effects. Master's thesis, Free University Berlin, 2013.

[42] Julius Zielinski. Erweiterung des kurzwelligen energiebereichs einer roentgenlaserquell zur spektroskopie and organischen molekuelen. Master's thesis, Unversity Potsdam, 2012.

[43] André TJB Eppink and David H Parker. Velocity map imaging of ions and electrons using electrostatic lenses: Application in photoelectron and photofragment ion imaging of molecular oxygen. *Review of Scientific Instruments*, 68(9):3477–3484, 1997.

[44] Vladimir Dribinski, Alexei Ossadtchi, Vladimir A Mandelshtam, and Hanna Reisler. Reconstruction of abel-transformable images: The gaussian basis-set expansion abel transform method. *Review of Scientific Instruments*, 73(7):2634–2642, 2002.

[45] A. Kramida, Yu. Ralchenko, J. Reader, and and NIST ASD Team. NIST Atomic Spectra Database (ver. 5.2), [Online]. Available: `http://physics.nist.gov/asd` [2015, March 4]. National Institute of Standards and Technology, Gaithersburg, MD., 2014.

[46] S Düsterer, L Rading, P Johnsson, A Rouzée, A Hundertmark, M J J Vrakking, P Radcliffe, M Meyer, A K Kazansky, and N M Kabachnik. Interference in the angular distribution of photoelectrons in superimposed xuv and optical laser fields. *Journal of Physics B: Atomic, Molecular and Optical Physics*, 46(16):164026, 2013.

[47] AK Kazansky and NM Kabachnik. Sideband structure in angle-resolved electron spectra from laser-assisted auger decay generated by ultra-short pulses. *Journal of Physics B: Atomic, Molecular and Optical Physics*, 42(12):121002, 2009.

[48] Norman M Kroll and Kenneth M Watson. Charged-particle scattering in the presence of a strong electromagnetic wave. *Physical Review A*, 8(2):804, 1973.

[49] Alfred Maquet and Richard TaÏeb. Two-colour ir+xuv spectroscopies: the ?soft-photon approximation? *Journal of Modern Optics*, 54(13-15):1847–1857, 2007.

[50] P Radcliffe, M Arbeiter, WB Li, S Düsterer, H Redlin, P Hayden, P Hough, V Richardson, JT Costello, T Fennel, et al. Atomic photoionization in combined intense xuv free-electron and infrared laser fields. *New Journal of Physics*, 14(4):043008, 2012.

[51] CP Hauri, W Kornelis, FW Helbing, A Heinrich, Arnaud Couairon, André Mysyrowicz, Jens Biegert, and Ursulla Keller. Generation of intense, carrier-envelope phase-locked few-cycle laser pulses through filamentation. *Applied Physics B*, 79(6):673–677, 2004.

[52] Kun Zhao, Qi Zhang, Michael Chini, Yi Wu, Xiaowei Wang, and Zenghu Chang. Tailoring a 67 attosecond pulse through advantageous phase-mismatch. *Optics letters*, 37(18):3891–3893, 2012.

[53] JL Gardner and JAR Samson. 304 å photoelectron spectra of co, n 2, o 2 and co 2. *Journal of Electron Spectroscopy and Related Phenomena*, 2(3):259–266, 1973.

[54] S Krummacher, V Schmidt, and F Wuilleumier. Inner-shell photoionisation in molecules: the nitrogen case. *Journal of Physics B: Atomic and Molecular Physics*, 13(20):3993, 1980.

[55] P. Baltzer, M. Larsson, L. Karlsson, B. Wannberg, and M. Carlsson Göthe. Inner-valence states of n_2^+ studied by uv photoelectron spectroscopy and configuration-interaction calculations. *Phys. Rev. A*, 46:5545–5553, Nov 1992.

[56] C. W. Walter, P. C. Cosby, and H. Helm. Photoexcitation and predissociation intensities of the c??1?u+(v=3 and 4), c?1?u(v=3 and 4), and b??1?u+(v=10, 12, 13, and 15) states of n2. *The Journal of Chemical Physics*, 112(10):4621–4633, 2000.

[57] P. Johnsson, W. Siu, A. Gijsbertsen, J. Verhoeven, A.S. Meijer, W. van der Zande, and M.J.J. Vrakking. Velocity map imaging of atomic and molecular processes at the free electron laser in hamburg (flash). *Journal of Modern Optics*, 55(16):2693–2709, 2008.

[58] O Kornilov, M Eckstein, M Rosenblatt, CP Schulz, K Motomura, A Rouzée, J Klei, Lutz Foucar, M Siano, A Lübcke, et al. Coulomb explosion of diatomic molecules in intense xuv fields mapped by partial covariance. *Journal of Physics B: Atomic, Molecular and Optical Physics*, 46(16):164028, 2013.

[59] Soren Pedersen and Ahmed H Zewail. Femtosecond real time probing of reactions xxii kinetic description of probe absorption fluorescence depletion and mass spectrometry. *Molecular Physics*, 89(5):1455–1502, 1996.

[60] LV Keldysh. Ionization in the field of a strong electromagnetic wave. *Sov. Phys. JETP*, 20(5):1307–1314, 1965.

[61] John J Hopfield. Absorption and emission spectra in the region λ 600-1100. *Physical Review*, 35(9):1133, 1930.

[62] M Wickenhauser and J Burgdorfer. Theoretical aspects of time-resolved autoionization. *LASER PHYSICS-LAWRENCE-*, 14(4):492–496, 2004.

[63] U. Fano. Effects of configuration interaction on intensities and phase shifts. *Phys. Rev.*, 124:1866–1878, Dec 1961.

[64] Christian Ott, Andreas Kaldun, Philipp Raith, Kristina Meyer, Martin Laux, Jörg Evers, Christoph H Keitel, Chris H Greene, and Thomas Pfeifer. Lorentz meets fano in spectral line shapes: A universal phase and its laser control. *Science*, 340(6133):716–720, 2013.

[65] Hiroki Mashiko, Tomohiko Yamaguchi, Katsuya Oguri, Akira Suda, and Hideki Gotoh. Characterizing inner-shell with spectral phase interferometry for direct electric-field reconstruction. *Nature communications*, 5, 2014.

[66] Philip Croteau, John B Randazzo, Oleg Kostko, Musahid Ahmed, Mao-Chang Liang, Yuk L Yung, and Kristie A Boering. Measurements of isotope effects in the photoionization of n2 and implications for titan's atmosphere. *The Astrophysical Journal Letters*, 728(2):L32, 2011.

[67] K. P. Huber, G. Stark, and K. Ito. Rotational structure in the hopfield series of n2. *The Journal of Chemical Physics*, 98(6):4471–4477, 1993.

[68] JB West, K Codling, AC Parr, DL Ederer, BE Cole, R Stockbauer, and JL Dehmer. Branching ratios and photoelectron angular distributions through the hopfield bands in n2 between 650 and 730 aa. *Journal of Physics B: Atomic and Molecular Physics*, 14(11):1791, 1981.

[69] GV Marr, JM Morton, RM Holmes, and DG McCoy. Angular distribution of photo-electrons from free molecules of n2 and co as a function of photon energy. *Journal of Physics B: Atomic and Molecular Physics*, 12(1):43, 1979.

[70] A. C. Parr, D. L. Ederer, B. E. Cole, J. B. West, Roger Stockbauer, Keith Codling, and J. L. Dehmer. Triply-differential photoelectron studies of molecular autoionization profiles: The 710-730 å region of the n$_2$ spectrum. *Phys. Rev. Lett.*, 46:22–25, Jan 1981.

[71] M Ogawa and Y Tanaka. Rydberg absorption series of n2. *Canadian Journal of Physics*, 40(11):1593–1607, 1962.

List of Publications

Publications covered in this thesis:

- Eckstein M., Yang, C.H., Frassetto, F., Poletto, L., Sansone, G., Vrakking, M. J. J. and Kornilov, O., Direct Imaging of Transient Fano States in N_2 (in preparation)

- Eckstein, M., Hummert, J., Kubin, M., Yang, C. H., M., Frassetto, F., Poletto L., Vrakking, M. J. J. and Kornilov, O., Alignment and characterization of the two-stage time delay compensating XUV monochromator, Reviev of Scientific Instruments (submitted)

- Eckstein, M., Yang, C. H., Kubin, M., Frassetto, F., Poletto, L., Ritze, H. H., Vrakking, M. J. J. and Kornilov, O., Dynamics of N2 Dissociation Upon Inner-Valence Ionization by Wavelength-Selected XUV Pulses., J. Phys. Chem. Lett., 2015, 6 (3), pp 419-425

Publications not covered in this thesis:

- Kornilov, O., Eckstein, M., Rosenblatt, M., Schulz, C. P., Motomura, K., Rouzée, A., ... & Frasinski, L. J., Coulomb explosion of diatomic molecules in intense XUV fields mapped by partial covariance., Journal of Physics B: Atomic, Molecular and Optical Physics, 2013, 46(16), 164028.

Short Summary

Time-resolved XUV spectroscopy allows investigation of dynamical processes directly in the time domain with both excellent time and spatial resolution due to the shorter wavelengths of the XUV light as compared to the spectroscopy in the visible range. In this thesis use time- and energy-resolved XUV spectroscopy to investigate ultrafast dynamics in molecular nitrogen (N_2), a diatomic molecule with one of the strongest chemical bonds that exist. Despite its simple molecular structure it exhibits many dynamical effects that are common to all molecules and simultaneously allows for sophisticated theoretical modelling, which enables development of theoretical tools to describe multi-electron dynamics and their influence on the structural dynamics on ultrafast time-scales.

The first part of the thesis presents the design, implementation and experimental characterization of a laser-driven HHG beamline for XUV-IR pump-probe time-resolved photoelectron/photoion spectroscopy. The key element of the beamline is a grating-based time delay compensating XUV monochromator that enables tuning the photon energy of the XUV pulse coming from the HHG source between 10 eV and 50 eV, while keeping the XUV pulse duration below 14 fs, the spectral width below 0.5 eV and the transmission efficiency through the monochromator above 6%.

The second part presents time- and XUV photon energy-resolved pump-probe (XUV-IR) photoelectron/photoion spectroscopy of the dissociation dynamics of N_2 upon ionization from the inner valence $2\sigma_g$ orbital (H-band) with an ionization potential of 37.5 eV. In the interpretation of the time-resolved spectroscopy the tuning of the XUV photon energy enables us to identify dissociative ionization of the molecule, neutral dissociation and autoionization induced dissociation in the data. The dissociative ionization of the $2\sigma_g$ orbital is imaged by a Coulomb explosion induced by the IR pulse and can be explained within a simplified model. The parameters of the model determine characteristic spectroscopic features of the electronic states involved in the dissociation dynamics with the accuracy higher than the output of *ab initio* calculations. The spectroscopic interpretation of XUV-only spectra (obtained simultaneously with the time-resolved spectra) triggered new *ab initio* calculations, carried out by collaborators within our group. The calculations could resolve a mismatch between the experimental data and the models presented in the literature.

Furthermore we present a time-resolved study of the ultrafast decay of an autoionizing resonance (17.3 eV) of the Hopfield series of N_2. The new beamline allows tuning the XUV photon energy to dominantly excite the resonance and to probe the resulting multi-electron dynamics with a short IR pulse. Time- and angular-resolved photoelectron spectroscopy is performed yielding direct access to the autoionization dynamics. We are able to observe decay of autoionizing resonances and are the first to record transient angular distributions of emitted electrons with decay times in the range of 20 fs. We compare our findings with other static and time-resolved studies.

Deutsche Kurzfassung

Zeitaufgelöste XUV-Spektroskopie ermöglicht es aufgrund der kürzeren Wellenlänge im Vergleich zur Spektroskopie im sichtbaren Frequenzspektrum, dynamische Prozesse mit einer hervorragenden Zeit- und Ortsauflösung zu vermessen. Die hier präsentierte Arbeit beschäftigt sich dabei mit ultraschnellen Dynamiken in molekularem Stickstoff (N_2). Trotz der simplen molekularen Struktur des Moleküls können eine Vielzahl dynamischer Prozesse beobachtet werden, die charakteristisch für alle Moleküle sind. Die simple Struktur emöglicht eine detaillierte komplexe Modellierung der dynamischen Prozesse, die anhand von experimentell gewonnenen Erkenntnissen überprüft werden kann.

Im ersten Teil der Arbeit werden Konstruktion, Implementierung und Charakterisierung einer lasergetriebenen HHG-Beamline für zeitaufgelöste Pump-Probe (XUV-IR) Photoelektronen-/Photoionenspektroskopie mit einem VMIS präsentiert. Das Herzstück der Beamline ist ein auf optischen Gittern basierender XUV-zeitverzögerungskompensierender Monochromator, der es ermöglicht, die Photonenergie des XUV-Pulses in einem Energiebereich von 10 eV bis 50 eV zu verstimmen, während die Pulsdauer kürzer als 14 fs ist, die spektrale Bandbreite weniger als 0.5 eV beträgt und die Transmission durch den Monochromator über 6% liegt.

Der zweite Teil der Arbeit präsentiert die Ergebnisse von zeit- und XUV- photonenergieaufgelöster Photoelektronen-/Photoionen-Spektroskopie von Dissoziationsdynamik N2. Es wird der spezielle Fall der durch die Ionisation der inneren Valenzschale ($2\sigma g$, H-Band, 37 eV) induzierten elektronischen und strukturellen Dissoziationsdynamik des Moleküls untersucht. In den zeitaufgelösten Spektren ist es möglich, die direkte ionisationsinduzierte Dissoziation des Moleküls sowie neutrale Dissoziation und autoionisationsinduzierte Dissoziation zu beobachten. Die direkte ionisationsinduzierte Dissoziation nach Entfernen eines Elektrons von der $2\sigma g$-Schale wird hierbei durch eine durch den IR-Puls induzierte Coulomb-Explosion abgebildet, die wir mit einem vereinfachten Modell beschreiben können. Die Parameter des Modells bestimmen die charakteristischen Eigenschaften der beteiligten elektronischen Zustände und können anhand der experimentellen Daten mit einer höheren Genauigkeit bestimmt werden als durch Ab-initio-Rechnungen. Die statischen XUV-Spektren (die zeitgleich mit den zeitaufgelösten XUV-IR-Spektren gewonnen werden) offenbaren einen Widerspruch zwischen unseren experimentellen Ergebnissen und einer Modellierung anhand von in der Literatur präsentierten Potenzialkurven. Durch verbesserte Ab-initio-Rechnungen, die von Kollegen innerhalb unserer Arbeitsgruppe durchgeführt wurden, konnte dieser Widerspruch beseitigt werden.

Des Weiteren werden experimentelle Ergebnisse zum ultraschnellen Zerfall einer autoionisierenden Resonanz (17.3 eV) der Hopfield-Serie von N_2 präsentiert. Die neue Beamline ermöglicht es, durch Verstimmen der XUV-Photonenenergie hauptsächlich eine einzelne Resonanz anzuregen und die induzierte Zerfallsdynamik mit einem kurzen IR-Puls abzutasten. Die zeit- und winkelaufgelösten Photoelektronenspektren ermöglichen es uns, verschiedene Zerfallskanäle der angeregten Resonanzen zu identifizieren und Zerfallszeiten im Bereich von 20 fs zu messen.

Acknowledgements

I am indebted to many people for their help and encouragement which were vital for the successful completion of this work.

First of all I would like to thank my supervisor, M.J.J. Vrakking, for giving me the opportunity to pursue my thesis and supervising it within the great infrastructure that is provided by the Max-Born-Institute.

I would like to express my biggest gratitude to my direct supervisor Oleg Kornilov, who, with his infinite power, positive attitude, open mind and cleverness, created a positive atmosphere and never let me down. Without his great knowledge of physics, mathematics and machine shop technology this work would not have been possible.

Further I want to thank Giuseppe Sansone for co-refereeing this thesis.

I would also like to thank Johan Hummert, Markus Kubin, Timur, Geert Reitsma, Kathrin Lange and Chung-Hsin Yang, who helped at different times with the building of the beamline and various characterization measurements. Without their help it would have been impossible to construct such a big experiment within the time constraints of a PhD thesis. I wish Johan all the best with his PhD and hope the beamline will not cause him any troubles.

I am indebted to Fabio Frassetto and Luca Poletto for their collaboration on the design and alignment of the monochromator.

Special thanks go to Roman Peslin, who can find a solution to any technical problem and who never hesitated to help quickly. Also many thanks to Wolfgang Becker and Arje Katz from the workshop who helped with the design of many parts of the beamline. I would also like to thank Reinhard Grosser for his help with vacuum technology.

Thanks to Christian Neidel, Jesse Klei, Jochen Mikosch and Martin Galbraith for the good spirit in sharing the lab and for keeping the laser running and in perfect shape. Futhermore I would like to thank Sascha Birkner, Christian Schröter, Felix Brauße, Axel Hundertmark, Martin Galbraith and Martin Flögel for fun times in the office and Franziska Buchner, Kathrin Lange and Andrea Lübcke for the great fun we had with the water-jet setup.

Last but not least I want to thank my parents for their unconditional love and support.